Vékonyrétegek és nanoszerkezetek mágneses rendeződésének elméleti vizsgálata

PhD értekezés

Nagyfalusi Balázs

Témavezető: Udvardi László

Budapesti Műszaki és Gazdaságtudományi Egyetem

2024

Theoretical study of the magnetic ordering of thin films and nanostructures

PhD Thesis

Balázs Nagyfalusi

Supervisor: László Udvardi

Budapest University of Technology and Economics

2024

Contents

List of Figures

List of Tables

List of Abbreviations

AFM	**A**ntif**e**rro**m**agnetic
ASA	**A**tomic **S**phere **A**pproximation
BLS	**B**rillouin **L**ight **S**cattering
CV	**C**ollective **V**ariable
DFT	**D**ensity **F**unctional **T**heory
DL	**D**ouble **L**ayer
DM	**D**zyaloshinsky–**M**oriya
DMI	**D**zyaloshinsky–**M**oriya **I**nteraction
DOS	**D**ensity **o**f **S**tates
FES	**F**ree **E**nergy **S**urface
FM	**F**erro**m**agnetic
FMR	**F**erro**m**agnetic **R**esonance
HAMR	**H**eat **A**ssisted **M**agnetic **R**ecording
LDOS	**L**ocal **D**ensity **o**f **S**tates
LSDA	**L**ocal **S**pin **D**ensity **A**pproximation
MAE	**M**agnetic **A**nisotropy **E**nergy
MCA	**M**agneto**c**rystalline **a**nisotropy
MC	**M**onte **C**arlo
MCS	**M**onte **C**arlo **S**tep
ML	**M**ono**l**ayer
MOKE	**M**agneto-**o**ptical **K**err **e**ffect
NN	**N**earest-**N**eighbour
NNN	**N**ext-**N**earest-**N**eighbour
PMA	**P**erpendicular **M**agnetic **A**nisotropy
RS-LMTO	**R**eal-**S**pace **L**inear **M**uffin**T**in **O**rbital (method)
SCE	**S**pin-**C**luster **E**xpansion
SA	**S**hape **A**nisotropy
SKKR	**S**creened **K**orringa–**K**ohn–**R**ostoker (method)
SOC	**S**pin–**O**rbit **C**oupling
SPO	**S**cattering **P**ath **O**perator
SRT	**S**pin **R**eorientation **T**ransition
STM	**S**canning **T**unneling **M**icroscopy
TM	**T**orque **M**ethod
TOM	**T**orsion **O**scillation **M**agnetometry
VASP	**V**ienna **a**b initio **S**imulation **P**ackage

Chapter 1

Introduction

The magnetism of nanostructures such as thin films and clusters has been a well-researched topic over the past 100 years. This began with Werner Heisenberg, who in the 1920s raised his model explaining ferromagnetism, which was generalized throughout the years, and today it is a widely accepted method to describe the magnetic excitations by means of Heisenberg Hamiltonians. Meanwhile thanks to the development of experimental techniques such as the scanning tunneling microscopy (STM), nowadays surfaces can be investigated at an atomic level, and spin chains can be created and controlled on these substrates with an atomic precision [1]. The mixing of superconductivity and magnetism has attracted considerable interest since the discovery of Majorana bound states in magnetic chains on top of a superconducting surface [2–4], and it may open a new prospect in quantum computation.

In the past decades thin films have a great importance in the technological applications, where their magnetic anisotropy plays a key role in several phenomena. This property was first discussed by Néel in 1954 [5], where he predicted the perpendicular interfacial anisotropy (PMA) as a result of the lowered symmetry at a surface or interface. Since then a considerable interest has been focused on the magnetism of thin films and multilayers. The interfacial nature of the PMA was experimentally first demonstrated in the 1960's on ultrathin NiFe films on Cu(111) [6]. This discovery was followed by a plethora of work both from theoretical and experimental points of view [7–10].

The most important practical use of magnetic anisotropy is in the magnetic data storage technology where the information is stored by controlling the magnetic orientation of a small magnetic domain that is retained by magnetic anisotropy. In the early implementation of magnetic recording the magnetization of the bits was parallel with the plane of the film. Application of materials with PMA triggered the reduction of grain size, and thus resulted in an order of magnitude increase of the storage density. The first technological application of perpendicular magnetic recording was in 2005 [11], and recent reviews on PMA can be found in Refs. [12–14]. Today the PMA in the ultrathin magnetic films, heterostructures and nanostructures

has an important role in the development of energy efficient and ultrahigh density memory and logic devices. In order to further increase the storage density, the grain size in the recording medium should be further decreased, which requires a high uniaxial magnetic anisotropy of the thin film. Due to the large magnetic anisotropy of the recording media the magnetic field produced by the write head might no longer be sufficient to overcome the barrier to switch the magnetization. To circumvent this issue a heat assisted magnetic recording (HAMR) was proposed [15–17]. In HAMR the magnetic anisotropy is decreased by temporarily heating the domain storing the information.

The magnetic anisotropy can be traced back to different contributions, namely the magnetocrystalline anisotropy (MCA), and the shape anisotropy (SA). The former is significant in materials with strong spin–orbit coupling (SOC), which can be enhanced by the combination of magnetic materials with heavy nonmagnetic elements. This component ensures the stability of nanoscale magnetic domains, particularly in thin films with PMA. The easy axis MCA in thin films often competes with the SA created by the dipole–dipole interaction, the latter preferring an in-plane orientation of the spins over a perpendicular alignment. The magnetization direction of ferromagnetic PMA materials rotates to in-plane as the film thickness is increased, which effect is called spin reorientation transition (SRT). Increasing the temperature may also induce a SRT due to the different temperature dependence of the MCA and the SA [18]. Since its discovery in the 1960s in NiFe(111)/Cu(111) films [6], thickness- and temperature-driven SRTs have been observed in a wide range of materials [18–21]. Understanding SRT is essential in engineering the thickness of the layers in heterostructures for stable room-temperature spintronic applications.

The Dzyaloshinsky–Moriya interaction (DMI) [22, 23] is also attributed to the SOC in systems with broken inversion symmetry, which naturally appears at magnetic-nonmagnetic interfaces. The DMI is responsible for the formation of chiral noncollinear spin structures including spin–spirals [24], domain walls [25] and skyrmions [26, 27], and leads to a nonreciprocal propagation of spin–waves [28]. Since DMI and MCA are both significant in the same magnetic-nonmagnetic interfaces, it is legitimate to raise the question whether DMI has an effect in the SRTs. A positive answer was found by Rózsa [29], where they showed a mechanism, how finite temperature spin fluctuations can cause the emergence of an effective dynamic anisotropy term in the spin–wave spectrum.

Magnetic skyrmions and other similar localized spin structures, such as antiskyrmions, biskyrmions and merons have been in the center of interest in the last decade. The studies showed, that the stability of these patterns can be traced back to several mechanisms, such as the DMI [30], four-spin interactions [31], or

the frustration of Heisenberg exchange interactions [32, 33]. These objects have been found in several bulk materials and thin films [34]. Modern techniques make possible to create, annihilate and move such objects [27], which can be regarded as quasiparticles [35]. Their size of nanometers, exceptional stability and mobility makes the skyrmions perfect candidates for usage in logical and high-density memory devices [36–38], and they form an emerging platform for future neuromorphic and quantum computing [39].

In numerical simulations the magnetic atomic clusters and ultrathin layers are frequently modeled by classical spin models [40]. The parameters of the spin Hamiltonians can be calculated from first principles using methods, such as the torque method (TM) [41, 42] or the spin–cluster expansion technique (SCE) [43–45]. This is a very effective method, Monte Carlo and spin dynamics simulations can reproduce and explain a myriad of phenomena, but their applicability is always limited by the accuracy of input parameters (e. g. exchange couplings, anisotropies), by the order of expansion of the spin–spin interactions, and the consideration of long-range interactions especially in a large simulation.

In order to avoid using spin models the magnetic ground state of nanoclusters can be determined directly from first principle calculations based on density functional theory. The real-space linear muffin-tin orbital method in the atomic sphere approximation (RS-LMTO-ASA) extended to non-collinear magnetic systems has been successfully used to obtain the magnetic configurations of supported nanoclusters [46–48]. Including the effects of spin–orbit coupling, this parameter-free method was applied to explore the complex magnetic ground state of Mn nanowires on Ag(111) and Au(111) [49], as well as of Cr nano-islands on Pd(111) [50]. Using the constrained local moment method employed with the multiple scattering Green's function technique [51, 52], the existence of a canted magnetic state of a Co chain along a Pt(111) surface step edge [53] was demonstrated from first principles in good agreement with experiment [54]. Deriving explicit expressions for the torque acting on the magnetic moments, the formation of a domain wall through a nano-contact has been studied within an *ab initio* framework [55]. Using the same approach for the torque and by solving the stochastic Landau–Lifshitz–Gilbert equations, it became possible to perform finite temperature spin dynamics simulations for monatomic Co chains on top of Au(001) [56].

In this thesis I use density functional theory (DFT) based electronic structure calculations to describe electronic and magnetic structure of ultrathin films and nanoclusters. Since the electronic degrees of freedom are much faster than the magnetic ones, the two can be decoupled, and the magnetic structure is investigated with a fixed electronic structure. As I described above, the magnetic structure

can be obtained either by introducing effective spin models, or directly from the electronic structure by finding the optimal magnetic ordering by using the *ab initio* equations. In this work I present examples for both ways, which have advantages and disadvantages too. The advantage of spin models is the smaller computational effort, and that the temperature effects can be easily considered in the spin dynamics calculations. On the other hand an *ab initio* method still describes the system better because a less simplified model of the physical system means less chance that our model cannot reproduce the more complicated spin structures found in the experiments.

This work is organized in the following way: first in Chapter 2 I present the basics of the methods I used. The electronic structure of the systems is determined in terms of the fully relativistic screened Korringa–Kohn–Rostoker (SKKR) method [57–59] (Sec. 2.1). Then I present how spin models can be set up to describe a magnetic thin film or a cluster of atoms, and how the appropriate coupling and anisotropy parameters can be obtained by using the method of infinitesimal rotation and spin–cluster expansion technique (Sec. 2.2). This is followed by the description of Monte Carlo simulations, and the well-tempered metadynamics method [60, 61] (Sec. 2.3), which was used to investigate the temperature dependent magnetic anisotropy energy of ultrathin films, and the equilibrium value of magnetic skyrmions in a lattice. The final section of this chapter discusses the *ab initio* energy minimisation scheme (Sec. 2.4), which was used to obtain the ground state of magnetic clusters.

Chapter 3 discusses the studies on magnetic anisotropy energy and spin reorientation transitions in magnetic ultrathin films. First I present the metadynamics method on model systems to formulate the general rules of the SRTs, and how the different distribution of anisotropy can cause a different kind of SRT. This is followed by two real, experimentally motivated thin films: Fe_n/Au(001) and Fe_2/W(110). The first example is a well researched ferromagnet, which shows a typical temperature dependent behaviour [19, 62]. The second, due to its lower symmetry, has a much more interesting behaviour. The observed SRT [46, 63, 64] was investigated in details with respect to the effect of the DMI, which can cause an effective finite temperature magnetic anisotropy term, described in Ref. [29].

In Chapter 4 I present the study on the temperature dependence of equilibrium topological charge of a lattice. This quantity – in some cases – can be interpreted as the number of skyrmionic textures, and thus I show how the chemical potential of skyrmions and antiskyrmions can be evaluated. This analysis was performed on the ultrathin skyrmion–hosting films, namely $(Pt_{0.95}Ir_{0.05})$/Fe/Pd(111) and Pd/Fe/Ir(111).

Chapter 5 contains the results of the *ab initio* optimisation of magnetic clusters

of atoms. Here I present three systems: Fe chains on top of Re(0001), Rh(111), and Nb(110) substrates. This part extends to demonstrate the effect of the angular momentum cutoff $\ell_{\max}$ used for the partial waves in multiple scattering theory on the magnetic structure, and I present a comparison of results gained from direct first principle and spin model calculations. I show how the experimentally measured spin–spiral structure can be reproduced theoretically by *ab initio* optimisation of magnetic moments.

The thesis is end with a summary of the conclusions and my thesis statements.

Chapter 2

Methods

In this chapter I present a brief summary of density functional theory and Korringa–Kohn–Rostoker multiple scattering theory, which I used to obtain the electronic structure of the investigated systems. The magnetic degrees of freedom of the systems are usually described by a classical Heisenberg spin model. I introduce the general formula, and describe the terms I use later. I present the relativistic torque method and the spin–cluster expansion technique, which were used to calculate the magnetic exchange parameters. I used Monte Carlo based well-tempered metadynamics simulations to describe the finite temperature effect of the spin systems. Here I present the basis of Monte Carlo simulations, and introduce why the well-tempered metadynamics is useful tool. The detailed description of the method and phenomenon based peculiarities are presented later in the respective Chapters for the magnetic anisotropy energy (Chap. 3) and skyrmion creation and annihilation (Chap. 4). The chapter finishes with the description of the conjugate gradient optimization method.

2.1 Calculating the electronic structure

The most ideal solution for acquiring the properties of a $\mathcal{H}$ quantum system would be solving the time independent Schrödinger equation:

$$(E_n - \mathcal{H})\Psi_n = 0\,. \tag{2.1}$$

In practice this option is only viable for a very few systems such as the hydrogen atom, the quantum harmonic oscillator or Hooke's atom. In the presence of more and more interacting particles the calculations become more and more difficult, and for solids, where the number of the interacting atoms N is so high ($N \approx 10^{23}$), the computational capacities mean another limit. The common solution is replacing the many-particle system with a single-particle system with some effective interaction. This simplification can be done within the terms of the density functional theory [65,

66]. The single particle problem can be solved for the atomic-scale volume, and then the solution can be expanded to the whole space by considering the scattering between the cells. For this purpose we use the Korringa–Kohn–Rostoker multiple scattering theory [57, 58]. In the following I present the core ideas of this theory, but the curious reader can find more details in a lecture note [67] and book [68] or in PhD dissertations of similar topics [69–71].

2.1.1 Density functional theory

The density functional theory (DFT) relies on the two Hohenberg—Kohn theorems [65]. The first one claims that there is a bijective relationship between the external potential and the ground state density and according to the second one the exact ground state density minimizes the energy of the system. In order to make the electronic structure calculations tractable within DFT Walter Kohn and Lu Jeu Sham [66] introduced the following approximations. They decomposed the energy of the system as:

$$E[\varrho] = T + \int V[\varrho]\mathrm{d}^3\mathbf{r} + E_\mathrm{C}[\varrho] + E_\mathrm{xc}[\varrho]\,, \tag{2.2}$$

where

$$T[\varrho] = \sum_i \int \varphi_i^*(\mathbf{r}) \left(-\frac{\hbar^2}{2m}\nabla^2\right) \varphi_i(\mathbf{r})\mathrm{d}^3\mathbf{r} \tag{2.3}$$

is the kinetic energy of non-interacting particles, V is an external potential, E_C is the energy of the electrons due to the Coulomb repulsion:

$$E_\mathrm{C} = \frac{e^2}{2}\int\int \frac{\varrho(\mathbf{r})\varrho(\mathbf{r}')}{\mathbf{r}-\mathbf{r}'}\mathrm{d}^3\mathbf{r}'\mathrm{d}^3\mathbf{r} \tag{2.4}$$

and E_xc is the exchange-correlation energy, where all correlation effects are contained. They further supposed that the ground state electron density ϱ can be reproduced by a density of non-interacting particles moving in a V_eff effective potential:

$$\varrho = \sum_{i\in\mathrm{occ.}} |\varphi_i(\mathbf{r})|^2\,, \tag{2.5}$$

where the i index runs over the occupied orbitals and the φ_i wave-functions satisfy the following Schrödinger equation:

$$\left(\frac{p^2}{2m} + V_\mathrm{eff}\right)\varphi_i = \varepsilon_i\varphi_i\,. \tag{2.6}$$

The above Kohn–Sham equation can be easily derived by applying the variational principle on the energy given in Eq. (2.2). The effective potential can be obtained as:

$$V_{\text{eff}} = V(\mathbf{r}) + V_{\text{H}}(\mathbf{r}) + V_{\text{xc}}(\mathbf{r}) \,, \tag{2.7}$$

where $V_{\text{H}}(\mathbf{r})$ is the Hartree potential:

$$V_{\text{H}}(\mathbf{r}) = \int \frac{\varrho(\mathbf{r}')}{|\mathbf{r} - \mathbf{r}'|} \mathrm{d}^3\mathbf{r}' \,, \tag{2.8}$$

and $V_{\text{xc}}(\mathbf{r})$ stands for the functional derivative of the exchange-correlation energy with respect of the density:

$$V_{\text{xc}}(\mathbf{r}) = \frac{\delta E_{\text{xc}}}{\delta \varrho} \,. \tag{2.9}$$

Whenever spin–orbit coupling plays an important role in a phenomenon the electronic structure of the system can be described by the relativistic Kohn–Sham–Dirac equation:

$$\left(c\boldsymbol{\alpha}\mathbf{p} + \boldsymbol{\beta}mc^2 + V_{\text{eff}} I_4 + \mu_B \boldsymbol{\beta}\boldsymbol{\Sigma}\mathbf{B}_{\text{eff}}\right) \Psi_n = \varepsilon_n \Psi_n \,, \tag{2.10}$$

where Ψ_n is a bispinor eigenstate with four components, $\mu_{\text{B}} = \frac{e\hbar}{2m_{\text{e}}}$ is the Bohr magneton, c is the speed of light, $m_{\mathbf{e}}$ and e is the mass and charge of an electron. The I_4 is the 4×4 identity matrix, the $\boldsymbol{\Sigma}$, and the α and β the Dirac matrices, are defined as the following:

$$\boldsymbol{\Sigma} = \begin{pmatrix} \boldsymbol{\sigma} & 0 \\ 0 & \boldsymbol{\sigma} \end{pmatrix} \qquad \boldsymbol{\alpha} = \begin{pmatrix} 0 & \boldsymbol{\sigma} \\ \boldsymbol{\sigma} & 0 \end{pmatrix} \qquad \boldsymbol{\beta} = \begin{pmatrix} I_2 & 0 \\ 0 & -I_2 \end{pmatrix} \,, \tag{2.11}$$

where $\boldsymbol{\sigma}$ are the Pauli matrices, and I_2 is the 2×2 identity matrix.

The density and magnetization density in relativistic formalism can be given as:

$$n(\mathbf{r}) = \sum_n \psi_n^\dagger(\mathbf{r})\psi_n(\mathbf{r}) \tag{2.12}$$

$$\mathbf{m}(\mathbf{r}) = -\mu_{\text{B}} \sum_n \psi_n^\dagger(\mathbf{r})\beta\boldsymbol{\Sigma}\psi_n(\mathbf{r}) \,. \tag{2.13}$$

In Eq. (2.10) a new effective field $\mathbf{B}_{\text{eff}}$ has been introduced which is the sum of the external magnetic field and the exchange-correlation field. The exchange-correlation field is the functional derivative of the exchange-correlation energy with respect of the magnetization density:

$$\mathbf{B}_{\text{xc}} = \frac{\delta E_{\text{xc}}}{\delta \mathbf{m}} \tag{2.14}$$

Unfortunately the exact form of the exchange-correlation energy functional is not

known. In the present thesis the local density approximation (LDA) is used for all the electronic structure calculations. In LDA the exchange-correlation energy density is approximated by the energy density of the uniform electron gas:

$$E_{\mathrm{xc}}^{\mathrm{LDA}}[\rho] = \int \rho(\mathbf{r})\varepsilon_{\mathrm{xc}}(\rho(\mathbf{r}))\ \mathrm{d}^3\mathbf{r} \tag{2.15}$$

2.1.2 Multiple scattering theory

Instead of solving the (2.1) Schrödinger equation, in scattering theory we define the resolvent operator:

$$\mathcal{G}(z) = (z - \mathcal{H})^{-1}\ , \tag{2.16}$$

where $\mathcal{H}$ is the Hamiltonian of the system, and z is a complex number outside of the $\{\varepsilon_n\}$ spectrum of $\mathcal{H}$. The coordinate representation of the resolvent operator is called the Green's function:

$$G(z, \mathbf{r}, \mathbf{r}') = \sum_n \frac{\psi_n(\mathbf{r})\psi_n^*(\mathbf{r}')}{z - \varepsilon_n}\ . \tag{2.17}$$

A local density of an operator $\mathcal{A}$ (e. g. n – electron density) can be calculated from the Green's function:

$$A(\mathbf{r}) = -\frac{1}{\pi}\mathrm{Im}\int f(z,\mu)\mathrm{Tr}(\mathcal{A}G^+(z,\mathbf{r},\mathbf{r}))\mathrm{d}z\,, \tag{2.18}$$

where $f(z,\mu) = (1+\mathrm{e}^{(z-\mu)/k_BT})^{-1}$ is the Fermi function, μ is the chemical potential, and G^+ denotes the limit of the Green's function as the complex energy z approaches the real axis from the direction of positive imaginary part.

In the Korringa–Kohn–Rostoker scattering theory we describe the solid state systems as a perturbation with respect to a chosen reference system i. e. the free space, so the $\mathcal{H}$ Hamiltonian is divided into two parts: the reference system $\mathcal{H}_0$ and a $\mathcal{V}$ perturbation (the potential):

$$\mathcal{H} = \mathcal{H}_0 + \mathcal{V}\,. \tag{2.19}$$

The volume of the solid state system is also partitioned. A usual way is the so called muffin-tin method [72], where the space is divided between nonoverlapping spheres and an interstitial region of constant potential. In our implementation we use a slightly different approach. The space is also divided to spheres centered at the atomic positions, but the total volume of the spheres equals to the volume of

the system, so in this way there is some overlap between the spheres. This is the so-called atomic sphere approximation (ASA). The perturbation potential is also divided between the atomic sites:

$$\mathcal{V} = \sum_{\mathbf{R}_i} \mathcal{V}_i \,, \tag{2.20}$$

where $\mathcal{V}_i$ is the single site potential centered at $\mathbf{R}_i$, which is restricted to sphere around $\mathbf{R}_i$. If the cells and the atomic potentials have spherical symmetry, we can use effective potentials which reflect this symmetry. In this case, the Kohn–Sham–Dirac equation is simplified to a radial equation, which has to be solved within a single cell.

The Green's function belonging to the reference system $\mathcal{H}_0$ is defined:

$$\mathcal{G}_0(z) = (z - \mathcal{H}_0)^{-1} \,, \tag{2.21}$$

similarly to $\mathcal{G}(z)$. Assuming the free particle as the reference system, $\mathcal{G}_0$ is known, and the perturbation can be included as the Green's function $\mathcal{G}$ of the interacting system is expanded into a Born series, and this way we get the single site t_i operator:

$$t_i(z) = \mathcal{V}_i + \mathcal{V}_i \mathcal{G}_0(z) t_i(z) = \cdots = (\mathcal{I} - \mathcal{V}_i \mathcal{G}_0(z))^{-1} \mathcal{V}_i \,, \tag{2.22}$$

where $\mathcal{I}$ is the identity operator. The scattering events can be easily described if we use the angular momentum expansion of the operator t_i, and of the Green's function G_0:

$$\mathbf{t} = \{t_i \delta_{ij}\} \qquad \mathbf{G}_0 = \{G_{0i,j}(1 - \delta_{ij})\} \qquad \boldsymbol{\tau} = \{\tau_{ij}\} \,, \tag{2.23}$$

where τ_{ij} is the so-called scattering path operator (SPO) between site i and j, which describes the possible scattering events between the i and the j sites. In Eq. (2.23) t_i, G_{0ij} and τ_{ij} are matrices with their sizes determined by the the angular momentum cutoff $\ell_{\max}$. The connection between the three quantity can be simply written in the matrix form as the following:

$$\boldsymbol{\tau} = \left(\mathbf{t}^{-1} - \mathbf{G}_0^{-1}\right)^{-1} \,. \tag{2.24}$$

With knowledge of the SPO and the solutions of the Kohn–Sham–Dirac equation, the real space representation of the Green's function can be calculated using the

following formula:

$$G(z,\mathbf{R}_i+\mathbf{r}_i,\mathbf{R}_j+\mathbf{r}_j)=\frac{z+mc^2}{2mc^2}\sum_{Q,Q'}Z_i^Q(z,\mathbf{r}_i)\tau_{i,j}^{Q,Q'}Z_i^{Q'}(z^*,\mathbf{r}_j)^\dagger - \delta_{ij}\frac{z+mc^2}{2mc^2}\sum_{Q}\Big(Z_i^Q(z,\mathbf{r}_i)J^Q(z,\mathbf{r}_i')^\dagger\Theta(r_i'-r_i) + Z_i^Q(z^*,\mathbf{r}_i')^\dagger J^Q(z,\mathbf{r}_i)\Theta(r_i-r_i')\Big) \tag{2.25}$$

where $\mathbf{R}_i$ is the position of site i, $Z_i^Q(z,\mathbf{r}_i)$ and $J^Q(z,\mathbf{r}_i')$ are the regular and irregular solutions of (2.10) Kohn–Sham–Dirac equation using the Bristol convention [73] with $Q=(\kappa,\mu)$ a composite angular momentum quantum number, where κ and μ are connected to the $\mathbf{J}$ and J_z total angular momentum. Finally $\Theta(x)$ denotes the Heaviside function.

The electron density can then be calculated using (2.18):

$$n(\mathbf{r},z)=-\frac{1}{\pi}f(\varepsilon)\mathrm{Im}\,\mathrm{Tr}\,G^+(z,\mathbf{r},\mathbf{r})\,. \tag{2.26}$$

After an energy integration we get $n(\mathbf{r})$, which can be substituted back into the exchange correlation energy and magnetic field, and then to the Kohn–Sham–Dirac equation again. This way we can calculate again self consistently until obtaining the desired precision. On the other hand if we perform a real space integration of Eq. (2.26) we get the $n(\varepsilon)$ density of states, which can be used to calculate the band energy, the torque acting on the magnetic moments and finally spin model parameters, that describe the system.

2.1.3 Numerical challenges

Theoretically, the $\mathbf{t}$, $\boldsymbol{\tau}$, and $\mathbf{G}$ matrices are infinite in both the site i and angular momentum Q indices, which should be treated for the numerical application. The angular momentum expansion is usually truncated by choosing a maximum value $\ell_{\max}$ for the orbital angular momentum quantum number. Due to spin and magnetic quantum numbers, overall this reduces the dimension to $2(\ell_{\max}+1)^2$ Q indices. Choosing $\ell_{\max}=2$ or $\ell_{\max}=3$ is usually enough to produce a good description of the systems we investigated.

A bulk system in a crystal lattice has a discrete translational invariance in the direction of all three base vectors and the Green's function can be calculated in Fourier space. If necessary an inverse Fourier transform can be performed to get it

in real-space. The accuracy of the electronic structure calculation depends on the number of $\mathbf{k}$ vectors used for calculating the $\boldsymbol{\tau}$ matrices.

The KKR structure constant G_{0ij} decays as $\frac{1}{r_{ij}^{\ell+1}}$ with the separation between sites i and j. This long range behaviour does not permit the calculations of the Green's function in real-space. In layered systems, such as a surface or an interface only two-dimensional translation invariance is present and the Fourier transform only partially solves our problem. This unfavorable property of the structure constant still remains in a direction normal to the surface. In order to overcome this difficulty a so called screened representation of the Green's function is applied. A detailed description of the screened KKR (SKKR) method can be found in Refs. [59, 74]. The basic idea of the screening transformation is the introduction of a repulsive potential. Treating the new potential construction as a reference system the Green's function falls off exponentially with distance, thus allowing the inversion of sparse, in the case of layered systems block tridiagonal matrices. The screening transformation can be considered as a special case of the embedding technique, and will be detailed in the next section. In practice both the bulk systems and interfaces are investigated with the same layered code to ensure the minimal numerical difference.

Here it is important to mention that the layer–layer distances close to the surface or interface must be also optimized in order to be able to reproduce experimental results. Since the KKR method is not the perfect choice to find the optimal geometric structure due to the muffin-tin potential construction and ASA usually the relaxations are obtained by using the Vienna *ab initio* Package (VASP) [75].

2.1.4 The embedded cluster method

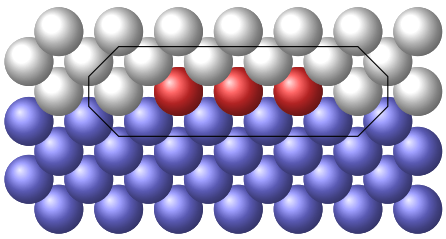

FIGURE 2.1: Concept of the embedded cluster method. The blue spheres denote the substrate atoms, whereas the white ones belong to the empty positions above the interface. The atoms of the cluster – denoted by red spheres – are placed in the vacuum positions. The black polygon surrounds the first neighbourhood of the cluster, which – as expanded cluster – is taken into account in the calculation.

The above described SKKR method is only suitable to describe layered systems with 2D discrete translation symmetry. This condition is obviously not fulfilled for a cluster of finite number of atoms. In this case the so-called embedding technique [74,

76] has to be used. Usally we assume, that the magnetic cluster is positioned on the surface of a hosting substrate. In this case the cluster changes the electronic structure in its close neighbourhood. So for a proper desciption not only the magnetic atoms, but also their environment is taken into account in the embedding scheme, as shown in Fig. 2.1. The number of included surrounding shells is system specific, but usually 1–2 shell is enough to describe the whole perturbation caused by the magnetic atoms. As this method assumes that the electronic properties of a hosting substrate are already known, it can act as a reference system (r) for further calculations. Based on Eq. (2.24), we can give the SPO of the reference system:

$$\boldsymbol{\tau}_r = \left(\mathbf{t}_r^{-1} - \mathbf{G}_0^{-1}\right)^{-1} . \tag{2.27}$$

Similarly, the SPO for the interested system (s) can be written as the following:

$$\boldsymbol{\tau}_s = \left(\mathbf{t}_s^{-1} - \mathbf{G}_0^{-1}\right)^{-1} . \tag{2.28}$$

From the difference of Eq. (2.27) and (2.28) we can get the following formula:

$$\boldsymbol{\tau}_s = \boldsymbol{\tau}_r \left(\mathbf{I} - (\boldsymbol{\Delta}\mathbf{t})^{-1} \boldsymbol{\tau}_r\right)^{-1} , \tag{2.29}$$

where I is the identity and

$$(\boldsymbol{\Delta} t)^{-1} = \mathbf{t}_r^{-1} - \mathbf{t}_s^{-1} . \tag{2.30}$$

Since this only differs from zero for the cluster atoms, (2.29) can be rewritten into:

$$\boldsymbol{\tau}_s^C = \boldsymbol{\tau}_r^C \left(\mathbf{I} - \left(\boldsymbol{\Delta}\mathbf{t}^C\right)^{-1} \boldsymbol{\tau}_r^C\right)^{-1} , \tag{2.31}$$

where C denotes the site indices inside the extended cluster (see Fig. 2.1). Note that this cluster contains not only the magnetic atoms, but the atomic sites from the host system surrounding it. This way we have to deal with matrices of dimension of only $N \times (\ell_{\max} + 1)^2$, where N denotes the number of sites in the extended cluster.

In the practice all these mentioned procedures for bulk, thin layers or atomic clusters are repeated successively in a self consistent way until the error for the potentials reaches a predefined desired precision.

2.2 Heisenberg spin model

The adiabatic approximation [40] makes possible to decouple the electronic and spin degrees of freedom of a magnetic system. In the spirit of the rigid spin approximation, the magnitude of the spins in the system is assumed constant, making possible to describe the magnetization at site i by a direction given by a unit vector $\mathbf{s}_i$, and the magnetic state of an N atomic system can be described by a set of $\{\mathbf{s}_i\}$ spin vectors. As introduced in the beginning of my work, the energy of the interacting spin system is often described by a classical Heisenberg Hamiltonian. From this point generally our spin Hamiltonian has the following form:

$$H = \sum_{i \neq j} \mathbf{s}_i^{\mathrm{T}} \mathbf{J}_{i,j} \mathbf{s}_j + \sum_i \mathbf{s}_i^{\mathrm{T}} \mathbf{K}_i \mathbf{s}_i \,, \tag{2.32}$$

where $\mathbf{s}_i$ is unit vector parallel to the atomic magnetization at site i, $\mathbf{J}_{i,j}$ is 3×3 tensor of exchange interactions, which can be decomposed into three parts in the following way [42]:

$$\begin{aligned} \mathbf{J}_{i,j} = & \frac{1}{3} \mathrm{Tr}\left(\mathbf{J}_{i,j}\right) \mathbf{I} + \frac{1}{2} \left(\mathbf{J}_{i,j} - \mathbf{J}_{i,j}^{\mathrm{T}}\right) \\ & + \frac{1}{2} \left(\mathbf{J}_{i,j} + \mathbf{J}_{i,j}^{\mathrm{T}} - \frac{2}{3} \mathrm{Tr}\left(\mathbf{J}_{i,j}\right) \mathbf{I}\right) . \end{aligned} \tag{2.33}$$

The $|i-j|$ spatial cutoff is system specific: e. g. for a short atomic spin chain the number of coupling parameters is low, and all can be included, but theoretically for a plane this number can be infinitely high, so one has to omit the negligible ones. The three parts of the $\mathbf{J}_{i,j}$ tensor can be interpreted as the following: the first $J_{i,j} = \frac{1}{3}\mathrm{Tr}\left(\mathbf{J}_{i,j}\right)$ term is the isotropic Heisenberg exchange coupling. The second

$$\mathbf{J}_{i,j}^{\mathrm{A}} = \frac{1}{2} \left(\mathbf{J}_{i,j} - \mathbf{J}_{i,j}^{\mathrm{T}}\right) \tag{2.34}$$

antisymmetric part is related to the Dzyaloshinsky–Moriya interaction (DMI):

$$\mathbf{s}_i^T \mathbf{J}_{i,j}^{\mathrm{A}} \mathbf{s}_j = \mathbf{D}_{i,j} \left(\mathbf{s}_i \times \mathbf{s}_j\right) \tag{2.35}$$

This type of exchange interaction was discovered by Dzyaloshinsky [22] and by Moriya [23]; it appears as a consequence of the relativistic spin–orbit coupling (SOC). The last, symmetric traceless part of the $\mathbf{J}_{i,j}$ second order tensor:

$$\mathbf{J}_{i,j}^{\mathrm{S}} = \frac{1}{2} \left(\mathbf{J}_{i,j} + \mathbf{J}_{i,j}^{\mathrm{T}} - \frac{2}{3} \mathrm{Tr}\left(\mathbf{J}_{i,j}\right) \mathbf{I}\right) \tag{2.36}$$

describes classical dipolar and SOC-induced pseudo-dipolar anisotropy contributions. It is commonly referred as the two-site anisotropy of the system. Finally, $\mathbf{K}_i$ is an on-site anisotropy tensor at site i. The sum of the on-site and two-site anisotropy matrices, as a 3×3 matrix has 3 eigendirections. The direction with the lowest energy eigenvalue is called easy direction and it is the preferred magnetization direction for a ferromagnetic system.

Note that the odd order terms in $\mathbf{s}_i$ are missing in Eq. (2.32) due to the time-reversal symmetry. In this work only second order terms are considered, but it has to be mentioned, that recently there are works that include higher order terms of spin–spin interaction in order to obtain higher accuracy of the results [77].

In general the largest energy contribution comes from the isotropic exchange. The DMI and the on-site and two-site anisotropy constants are smaller by a scale. Regardless of the scale of these parameters they should reflect the symmetry of the system.

In the the following I present two different methods, which can be used to obtain the spin model parameters: the relativistic torque method or method of infinitesimal rotations, and the spin–cluster expansion, which two were both used for some calculations in this work.

2.2.1 The relativistic torque method

It was demonstrated first by Liechtenstein *et al.* [41], how Heisenberg exchange interactions between pairs of spins may be determined based on the derivatives of the energy i. e. the torque acting on the spins. Later this torque method or the method of infinitesimal rotations was generalized for relativistic systems by Udvardi and his coworkers [42] and it is a commonly used method today.

In the spirit of the magnetic force theorem [78], $V_{\text{eff}}(r)$ potential and $B_{\text{eff}}(r)$ exchange field are kept fixed for small changes of the magnetic orientations. This implies that the number of the electrons in a finite cluster is not preserved, therefore, the variation of the energy of the system at zero temperature is replaced by the variation of the grand potential, $\Omega = E - \varepsilon_{\text{F}} N$, where the energy E of the system is approximated by the single particle (band) energy,

$$\Delta\Omega = \int_{-\infty}^{\varepsilon_{\text{F}}} \Delta n(\varepsilon)(\varepsilon - \varepsilon_{\text{F}}) \mathrm{d}\varepsilon = -\int_{-\infty}^{\varepsilon_{\text{F}}} \Delta N(\varepsilon) \mathrm{d}\varepsilon \,, \tag{2.37}$$

where ε_{F} is the Fermi energy and $N(\varepsilon) = \int_{-\infty}^{\varepsilon} n(\varepsilon')\mathrm{d}\varepsilon'$ is the integrated density of states (DOS). The main advantage of this formula is that in the multiple scattering theory it can easily be calculated using Lloyd's formula [42, 79].

It is straightforward to derive a formula for the first order change of the grand potential when the exchange correlation field in an atomic sphere at site i is rotated around a unit vector $\mathbf{n}_i$ with an angle of $\Delta\varphi_i$:

$$\Delta\Omega_i^{(1)} = \mathbf{T}_i \Delta\boldsymbol{\varphi}_i \,, \tag{2.38}$$

where $\Delta\boldsymbol{\varphi}_i = \mathbf{n}_i\Delta\varphi_i$, and the $\mathbf{T}_i$ is the torque, defined as:

$$\mathbf{T}_i = \frac{1}{\pi}\int_{-\infty}^{E_{\mathrm{F}}} \mathrm{Im}\,\mathrm{Tr}\left(\frac{i}{\hbar}\left[\mathbf{J}, t_i^{-1}\right]\tau_{ii}\right)\mathrm{d}\varepsilon \,, \tag{2.39}$$

where $\mathbf{J} = \mathbf{L}+\mathbf{S}$ is the matrix of the total angular momentum operator, t_i and τ_{ii} are the single-site scattering matrix and the scattering path operator, respectively, defined previously in Sec 2.1. Similarly the second order change of the grand potential due to the rotations at sites i and j by $\Delta\boldsymbol{\varphi}_i$ and $\Delta\boldsymbol{\varphi}_j$, respectively:

$$\Delta\Omega_{ij}^{(2)} = \frac{1}{2}\Delta\varphi_i H_{ij} \Delta\varphi_j \,, \tag{2.40}$$

where H_{ij} is the Hessian matrix, defined as:

$$\begin{aligned} H_{ij} = \frac{1}{\pi}\int_{-\infty}^{E_{\mathrm{F}}} \frac{1}{\hbar^2}\mathrm{Im}\,\mathrm{Tr}\Big(&\left[\mathbf{J}, t_i^{-1}\right]\tau_{ij}\left[\mathbf{J}, t_j^{-1}\right]\tau_{ji} \\ &-\delta_{ij}\left\{\left[\mathbf{J}, \left[\mathbf{J}, t_i^{-1}\right]\right]\right\}\tau_{ii}\Big)\,\mathrm{d}\varepsilon \,. \end{aligned} \tag{2.41}$$

The first and second derivatives need not to be calculated for arbitrary rotation axes, since every infinitesimal rotation of the direction $\mathbf{s}_i$ may be expressed as a linear combination of rotations around two vectors, which are linearly independent from each other and $\mathbf{s}_i$. We will choose these fixed directions in such a way that the vectors $\mathbf{e}_{1i}$, $\mathbf{e}_{2i}$, and $\mathbf{s}_i$ form an orthonormal right-handed system as shown in Fig. 2.2, and the rotations are chosen as:

$$\Delta\varphi_i = \Delta\varphi_{1i}\mathbf{e}_{1i} + \Delta\varphi_{2i}\mathbf{e}_{2i} \,, \tag{2.42}$$

where the rotation angles $\Delta\varphi_{1i}$, and $\Delta\varphi_{2i}$ are defined to be positive for right-handed rotations.

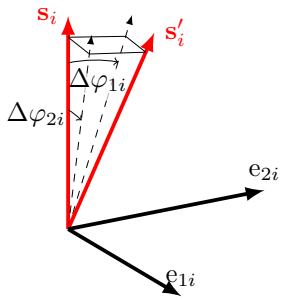

FIGURE 2.2: Rotation of $\mathbf{s}_i$ magnetization vector around the orthogonal directions $\mathbf{e}_{1i}$ and $\mathbf{e}_{2i}$ by angles $\Delta\varphi_{1i}$ and $\Delta\varphi_{2i}$, respectively.

We can calculate the same derivatives for the (2.32) general classical Heisenberg model. The first derivatives with respect to the rotation of $\mathbf{s}_i$ at site i are:

$$\frac{\partial H}{\partial \Delta\varphi_{1i}} = -\sum_j \mathbf{e}_{2i}\mathbf{J}_{i,j}\mathbf{s}_j - \left(\mathbf{e}_{2i}^{\mathrm{T}}\mathbf{K}_i\mathbf{s}_i + \mathbf{s}_i^{\mathrm{T}}\mathbf{K}_i\mathbf{e}_{2i}\right) \tag{2.43}$$

$$\frac{\partial H}{\partial \Delta\varphi_{2i}} = \sum_j \mathbf{e}_{1i}\mathbf{J}_{i,j}\mathbf{s}_j + \left(\mathbf{e}_{1i}^{\mathrm{T}}\mathbf{K}_i\mathbf{s}_i + \mathbf{s}_i^{\mathrm{T}}\mathbf{K}_i\mathbf{e}_{1i}\right) , \tag{2.44}$$

where we used that $\partial\mathbf{s}_i/\partial\varphi_{li} = \mathbf{e}_{li}\times\mathbf{s}_i$ and $\mathbf{e}_{1i}\times\mathbf{e}_{2i} = \mathbf{s}_i$. The similarly the second derivatives:

$$\frac{\partial^2 H}{\partial\Delta\varphi_{1i}\partial\Delta\varphi_{1j}} = \mathbf{e}_{2i}\mathbf{J}_{i,j}\mathbf{e}_{2j} \qquad \text{for } i\neq j\,, \tag{2.45}$$

$$\frac{\partial^2 H}{\partial\Delta\varphi_{2i}\partial\Delta\varphi_{2j}} = \mathbf{e}_{1i}\mathbf{J}_{i,j}\mathbf{e}_{1j} \qquad \text{for } i\neq j\,, \tag{2.46}$$

$$\frac{\partial H}{\partial\Delta\varphi_{1i}\partial\Delta\varphi_{2i}} = -\mathbf{e}_{1i}\mathbf{J}_{i,j}\mathbf{e}_{2j} \qquad \text{for } i\neq j\,, \tag{2.47}$$

$$\frac{\partial H}{\partial\Delta\varphi_{2i}\partial\Delta\varphi_{1i}} = -\mathbf{e}_{2i}\mathbf{J}_{i,j}\mathbf{e}_{1j} \qquad \text{for } i\neq j\,, \tag{2.48}$$

$$\frac{\partial^2 H}{\partial\Delta\varphi_{1i}\partial\Delta\varphi_{1i}} = -\sum_j \mathbf{s}_i\mathbf{J}_{i,j}\mathbf{s}_j + 2\left(\mathbf{e}_{2i}^{\mathrm{T}}\mathbf{K}_i\mathbf{e}_{2i} - \mathbf{s}_i^{\mathrm{T}}\mathbf{K}_i\mathbf{s}_i\right) \qquad \text{for } i=j\,, \tag{2.49}$$

$$\frac{\partial^2 H}{\partial\Delta\varphi_{2i}\partial\Delta\varphi_{2j}} = -\sum_j \mathbf{s}_i\mathbf{J}_{i,j}\mathbf{s}_j + 2\left(\mathbf{e}_{1i}^{\mathrm{T}}\mathbf{K}_i\mathbf{e}_{1i} - \mathbf{s}_i^{\mathrm{T}}\mathbf{K}_i\mathbf{s}_i\right) \qquad \text{for } i=j\,, \tag{2.50}$$

$$\frac{\partial H}{\partial\Delta\varphi_{1i}\partial\Delta\varphi_{2i}} = \frac{\partial H}{\partial\Delta\varphi_{2i}\partial\Delta\varphi_{1i}} = -\left(\mathbf{e}_{1i}^{\mathrm{T}}\mathbf{K}_i\mathbf{e}_{2i} + \mathbf{e}_{2i}^{\mathrm{T}}\mathbf{K}_i\mathbf{e}_{1i}\right) \qquad \text{for } i=j\,. \tag{2.51}$$

From the Eqs. (2.45)-(2.48) only the four transverse components of the $\mathbf{J}_{ij}$ matrix can be obtained supposing a ferromagnetic reference configuration. In order to determine the full $\mathbf{J}_{ij}$ matrix the second derivatives of the band energy must be calculated for three or more ferromagnetic orientations and the matrix can be obtained by fitting Eqs. (2.45)-(2.48). The diagonal elements of the on-site anisotropy

$\mathbf{K}_i$ can be obtained from the difference of Eqs. (2.49) and (2.50). Note that in this way it is only possible to calculate the difference of two diagonal elements of $\mathbf{K}_i$, but such a shift in free energy does not influence the magnetic configuration.

The magnetic dipole-dipole interaction

$$\mathbf{D}_{ij} = m_i m_j \frac{r_{ij}\delta_{ij} - 3\mathbf{r}_{ij} \circ \mathbf{r}_{ij}}{r_{ij}^5} \,, \tag{2.52}$$

also has a two-site anisotropy contribution but it is usually weaker than other contributions, and often it is omitted from the simulations.

2.2.2 The spin–cluster expansion method

Whereas the torque method uses a ferromagnetic ground state to obtain the spin model parameters by calculating the infinitesimal rotations, in the spin–cluster expansion (SCE) [43, 44] the band energy is calculated in the paramagnetic state, where the directions of the exchange field on different sites have a uniform distribution on the unit sphere.

The grand potential can be expanded using real space harmonics $Y_L(\mathrm{s}_i)$, where L is a composite angular momentum index for (l, m), which up to second order looks as the following:

$$\Omega = \Omega_0 + \sum_i \sum_{L\neq(0,0)} J_i^L Y_L(\mathbf{s}_i) + \frac{1}{2}\sum_{i\neq j} \sum_{L\neq(0,0)} \sum_{L'\neq(0,0)} J_{ij}^{L,L'} Y_L(\mathbf{s}_i) Y_{L'}(\mathbf{s}_j) \,, \tag{2.53}$$

where $\Omega_0 = \langle Q \rangle$, and the integrals are

$$J_i^L = \int \langle Q \rangle_{\mathbf{s}_i} Y_L(\mathbf{s}_i) \mathrm{d}^2\mathbf{e}_i \,, \tag{2.54}$$

and

$$J_{i,j}^{L,L'} = \iint \langle Q \rangle_{\mathbf{s}_i,\mathbf{s}_j} Y_L(\mathrm{s}_i) Y_{L'}(\mathrm{s}_i) \mathrm{d}^2\mathbf{e}_i \mathrm{d}^2\mathbf{e}_j \,. \tag{2.55}$$

Here $\langle\cdot\rangle$ means an average for all possible configurations, and in Eqs. (2.54) and (2.55) the noted $\mathbf{s}_i$ spins are fixed during the averaging process. For further details a more comprehensive description of the method can be read in Ref. [69].

Note that the torque method (TM) and the SCE technique use different spin configurations to obtain the exchange parameters. The TM relies on ordered spin configurations, which respects the symmetry of the system. In general this means a collinear ferro-, or antiferromagnetic reference, which are in most cases the ground state of the system. On the other hand, the SCE calculations rely on a disordered,

paramagnetic state as a reference, which often provides more realistic exchange parameters than the TM for noncollinear magnetic systems. This implies that the TM is better suited to describe the collinear ground state and low temperature excitations, whereas the SCE based parameters better describe the non collinear, high temperature magnetism.

Usually the coupling parameters are used in Monte Carlo (MC) and Landau-Lifshitz-Gilbert spin dynamics simulations [56] to obtain the magnetic configuration. In my work I used a MC simulation based method called metadynamics, which I present in detail in the following section.

2.3 Monte Carlo simulations

2.3.1 The Metropolis algorithm

A Monte Carlo simulation is a powerful tool to numerically compute integrals such as thermodynamics average of different quantities by using random positions, called samples. The choice on sampling is essential to gain correct results, and a common choice is using Markov-chain algorithms. In this case the new sample (b) is always based on the previous one (a) with a finite probability of this transition. An algorithm is proved to be good, if the so-called detailed balance is fulfilled for every possible a and b samples:

$$\pi(a)\mathbb{P}(a \to b) = \pi(b)\mathbb{P}(b \to a)\,, \tag{2.56}$$

where probability $\mathbb{P}(a \to b)$ of changing sample from a to b and $\pi(a)$ is the stationary probability of sample a. The Metropolis algorithm [80] is one of the most frequently applied choice to obtain the probability $\mathbb{P}(a \to b)$:

$$\mathbb{P}(a \to b) = \min\left[1, \frac{\pi(b)}{\pi(a)}\right]\,. \tag{2.57}$$

If $\pi(b) > \pi(a)$ i. e. the final sample is more probable than the initial, then $\mathbb{P}(a \to b) = 1$, and id $\pi(b) < \pi(a)$ then the change only appears with a smaller probability.

In my work I investigate spin systems, where each sample can be matched to a configuration and the change is rotation of $\mathbf{s}_i$ to $\mathbf{s}_i'$. The probability of a spin configuration $\{\mathbf{s}_i\}_{i=1}^N$ at a finite temperate depends on its energy given by the spin Hamiltonian of the system. Thus we get the following expression:

$$\mathbb{P}(\mathbf{s}_i \to \mathbf{s}_i') = \begin{cases} e^{-\beta\left[E(\mathbf{s}_i') - E(\mathbf{s}_i)\right]} & \text{if } \Delta E > 0 \\ 1 & \text{otherwise,} \end{cases} \tag{2.58}$$

where β is the inverse temperature and $E(\mathbf{s})$ is the energy of the spin configuration given the spin model Hamiltonian of the system. This algorithm works very well for simpler cases, but as more complex spin structures appear the sampling of the whole configuration space becomes more cumbersome due to the larger energy barriers. The computational time is increased, and in worse cases the results will correlate with the initial configuration, which must be avoided. That is the reason why more sophisticated methods are needed to use.

2.3.2 Metadynamics

Adaptive bias potential methods, such as Wang-Landau algorithm [81], umbrella sampling [82] and metadynamics [60], are widely used to compute the free energy landscapes. If the local minima of the free energy of a system are separated by high energy barriers simulations often get stuck leading to extremely long running time and false conclusions. In adaptive bias potential method the bias potential continuously evolves during the simulation and destabilizes states that have already been visited. In my thesis metadynamics has been chosen to study magnetic anisotropy and spin reorientation transition in thin films, and for investigating the evolution of topological charge in skyrmionic systems.

Metadynamics was first introduced by Alessandro Laio and Michele Parinello in 2002 [60]. In this algorithm the biasing potential is constructed as a sum of Gaussians centered along a trajectory of a random walker in the space of collective variables (CVs). In their initial work of the method Laio *et al.* tested the method on chemical reactions, such as the dissociation of NaCl in water or the isomerization of alanine dipeptide in water [60]. In this work the CVs were the distance $r_{\mathrm{Na-Cl}}$ between Na and Cl ion and the electric fields V_{Na} and V_{Cl} on the Na and on the Cl in the first study and in the second study they were the backbone dihedral angles. Already from these examples it can be seen that the choice and the exact number of collective variables depend on the investigated system and phenomena we are interested in. In our particular case the out-of-plane component of the collective magnetization has been chosen to be the CV for studying magnetic anisotropy and the topological charge for investigating magnetic skyrmions. The algorithm was improved during the years, the adaptively changing height of the Gaussians facilitated the smooth converge of the biasing potential – well-tempered metadynamics [61] –, and this algorithm was proved to converge to the exact free energy [83].

In its first implementation, in chemistry [60] the drive of the walker was based on molecular dynamics [60], but later it was successfully implemented in Monte Carlo simulations as well [84–86]. In solid state physics Tobik *et al.* [86] used metadynamics to sample the free energy surface (FES) of a vortex in a nanodot, and

very recently similarly to us, Charalampidis *et al.* used this method to investigate the effect of thermal spin fluctuations on skyrmion stability [87]. For our purposes metadynamics has been applied in MC simulations. Considering a Monte Carlo step (MCS) as a time step, the bias potential becomes time dependent. After every τ MCS a Gaussian potential centered at the actual value of the CV (η_{act}), is added to the biasing potential:

$$V_{\mathrm{bias}}(\eta, t+\tau) = V_{\mathrm{bias}}(\eta, t) + V_{\mathrm{G}}(\eta - \eta_{\mathrm{act}})\,, \tag{2.59}$$

$$V_{\mathrm{G}}(\eta - \eta_{\mathrm{act}}) = we^{-\frac{(\eta-\eta_{\mathrm{act}})^2}{2\sigma}}\,, \tag{2.60}$$

where σ and w are the width and the height of the Gaussian, respectively. In well-tempered metadynamics [61] the height of the Gaussian depends on the actual value of the bias potential.

In our metadynamics implementation we applied a simple Metropolis algorithm, where during the calculation of the change of the energy in a trial the change of the bias potential has been also included. The probability of acceptance of a random change defined in Eq. (2.57) has the following form:

$$P(\mathbf{s}_i \to \mathbf{s}_i') = \begin{cases} e^{-\beta[E(\mathbf{s}')+V_{\mathrm{bias}}(\eta(\mathbf{s}'))-E(\mathbf{s})-V_{\mathrm{bias}}(\eta(\mathbf{s}))]} & \text{if } \Delta\left(E+V_{\mathrm{bias}}(\eta)\right) > 0 \\ 1 & \text{otherwise,} \end{cases} \tag{2.61}$$

where $\mathbf{s}$ and $\mathbf{s}'$ denote the spin configuration before and after the $\mathbf{s}_i \to \mathbf{s}_i'$ change was made on site i.

Due to the bias all configurations belonging to the same CV value η become less preferable and the walker moves to another configuration, but the history of the walk is stored in the biasing potential. After a predefined number of Monte Carlo steps the biasing potential is updated by adding a Gaussian centered at the actual value of the CV with the height of

$$w = w_0 e^{-\frac{V_{\mathrm{b}}(\eta)}{k_{\mathrm{B}}T_{\mathrm{m}}}}, \tag{2.62}$$

where T_{m} is an appropriately chosen temperature as it is explained in the procedure of well-tempered metadynamics [61]. Performing a fairly large number of steps the free energy is sampled in the whole range of CV. In well-tempered metadynamics the bias potential becomes stationary and the free energy $F(T)$ of the system is identified with the negative of the bias potential. Due to the introduction of the T_{m} temperature in the well-tempered calculations the connection between the free

energy and the biasing potential is the following:

$$F(T) = -V_{\mathrm{b}}(\eta(T)) = -\frac{T + T_{\mathrm{m}}}{T_{\mathrm{m}}} V_{\mathrm{bias}}(\eta(T)), \tag{2.63}$$

where $\eta(T)$ stands for the equilibrium value of the CV [83].

2.4 Ab initio optimization of magnetic configuration for atomic clusters

Building up a classical Heisenberg model-based on first principle calculations turned out to be an effective and successful way of exploring magnetic properties of several systems. However, there are situations where the inclusion of higher order magnetic interactions are necessary for the right description of magnetic properties. *Ab initio* calculation of higher order interactions is also possible [44], but their large number makes the simulations hardly tractable. For small atomic clusters the direct optimization of the magnetic structure without any underlying magnetic model is a passable way. In the present thesis a modified version of the conjugate gradient and Newton–Raphson methods [55] have been used to find the magnetic ground state of deposited clusters from first principles. The method is implemented into the SKKR framework applying the usual approximations (see Sec. 2.1): the magnetic moment of an atom is calculated in a corresponding atomic sphere, the direction of the exchange field is supposed to be constant within an atomic sphere only its magnitude has a radial dependence. As a starting point the electronic structure of the host system – a semi infinite substrate and semi infinite vacuum – is calculated. The electronic structure of a deposited magnetic clusters is described by the embedded cluster technique (see Sec. 2.1.4): the effective potential of the cluster atoms replace those of the vacuum positions on the surface of the substrate and the new effective potentials and fields are self-consistently iterated.

In case of spin model-based techniques at this point the exchange coupling and anisotropy parameters are evaluated and any further optimizations are done within the magnetic model (e. g. classical Heisenberg model). In our case the exchange field on each magnetic atom is rotated to find the optimal directions and the V_{eff} effective potentials and B_{xc} exchange-correlation fields are recalculated. The procedure is continued as long as the errors decrease below a predefined value. In the case of simple systems a simultaneous iteration of the direction of the exchange field, of the effective potential and of the exchange-correlation field works flawlessly [55]. However, in case of complex magnetic structures, e. g. for frustrated antiferromagnetic or for spin-spiral ground states, the convergence of the above scheme might be less

satisfactory. Here comes the idea to estimate the change of the energy of the system with respect to the change of the orientation of the magnetization the same way as for obtaining the spin model parameters for the torque method in Sec. 2.2.1. The formulas for the grand potential, and its first and second derivatives for a cluster can be found in Eqs. (2.37), (2.38), and (2.40).

The detailed description of the method is the following: At first V_{eff} and B_{xc} are fixed and we search for the directions of the exchange correlation field $\mathbf{s}_i$ at each sites corresponding to the lowest free energy. Once the minimum of the grand potential Ω is found the set of $\mathbf{s}_i$ is kept frozen and $V_{\text{eff},i}$ and $B_{\text{xc},i}$ are iterated. The whole procedure is repeated until the error of the effective potential and the exchange correlation field as well as the torque on each site gets smaller than a predefined value.

Note that during the optimization $\mathbf{s}_i$ is moving on the surface of a unit sphere. The minimum of the free energy should be found on the direct product of the unit spheres, thus the standard optimization methods working in Euclidean space do not apply. Instead, an extension of the conjugate gradient algorithm to Riemann manifolds has been used [88–90]: Let $\mathbf{t}_i^{(k)}$ be the torque vector for site i at the kth step of iteration. At the start of the iteration $\mathbf{t}_i^{(0)}$ is set to equal $\mathbf{T}_i$ given by Eq. (2.39). As a first step of the iteration we look for the minimum of the grand potential with respect of α,

$$\Omega(\alpha) = \Omega\left\{O\left(\mathbf{n}_i^{(k)}, \alpha t_i^{(k)}\right)\mathbf{s}_i\right\}\ , \tag{2.64}$$

where $t_i^{(k)} = |\mathbf{t}_i^{(k)}|$, $\mathbf{n}_i^{(k)} = \mathbf{t}_i^{(k)}/t_i^{(k)}$ and $O(\mathbf{n}, \varphi)$ denotes a rotation around a vector $\mathbf{n}$ with an angle of φ. This way every $\mathbf{s}_i$ spin is rotated around the local torque $\mathbf{t}_i^{(k)}$ by an angle which is given by a product of the local magnitude of the torque $t_i^{(k)}$ and a global parameter α. Once the minimum with respect to α is found for the next iteration step $k+1$ we recalculate the torque $\mathbf{T}_i^{(k+1)}$ using Eq. (2.39) now in the new configuration, and the effective torque for the next iteration step is set by mixing $\mathbf{T}_i^{(k+1)}$ with $\mathbf{t}_i^{(k)}$:

$$\mathbf{t}_i^{(k+1)} = \mathbf{T}_i^{(k+1)} + \beta_i \mathbf{t}_i^{(k)}, \tag{2.65}$$

where the multipliers β_i are set by the Polak-Ribière formula [91]:

$$\beta_i = \frac{\left(\mathbf{T}_i^{(k+1)} - \mathbf{T}_i^{(k)}\right)\mathbf{T}_i^{(k+1)}}{\mathbf{T}_i^{(k+1)}\mathbf{T}_i^{(k)}}\ . \tag{2.66}$$

The iteration is repeated until satisfactory convergence is achieved.

The efficiency of this optimization scheme is increased by using the Newton-Raphson method adopted to the Riemann manifold. Using Eqs. (2.38) and (2.40) the change of the grand potential up to second order can be written as:

$$\begin{aligned}\Delta\Omega &= \sum_i \Delta\Omega_i^{(1)} + \frac{1}{2}\sum_{ij}\Delta\Omega_{ij}^{(2)} = \\ &= \sum_i \mathbf{T}_i\Delta\boldsymbol{\varphi}_i + \frac{1}{2}\sum_{ij}\Delta\boldsymbol{\varphi}_i H_{ij}\Delta\boldsymbol{\varphi}_j\,.\end{aligned} \tag{2.67}$$

The component of the total angular momentum operator parallel to $\mathbf{s}_i$ commutes with the single site scattering matrix t_i: $[\mathbf{s}_i\mathbf{J}, t_i] = 0$, consequently:

$$\mathbf{T}_i\mathbf{s}_i = 0, \qquad\qquad H_{ij}\mathbf{s}_j = 0\,. \tag{2.68}$$

In order to find the set of rotation $\{\Delta\boldsymbol{\varphi}_i\}$ minimizing the free energy the search must be constrained to the manifold perpendicular to $\{\mathbf{s}_i\}$. Using the two perpendicular auxiliary vectors $\mathbf{e}_{1i}$ and $\mathbf{e}_{2i}$ as seen on Fig. 2.2, this rotation angles can be written as

$$\Delta\boldsymbol{\varphi}_i = \Delta\varphi_{1i}\mathbf{e}_{1i} + \Delta\varphi_{2i}\mathbf{e}_{2i}\,. \tag{2.69}$$

This can be substituted into Eq. (2.67) to obtain the Newton-Raphson equations for $\gamma = 1, 2$:

$$\mathbf{e}_{\gamma i}\mathbf{T}_i + \sum_{\gamma' j}\mathbf{e}_{\gamma i}H_{ij}\mathbf{e}_{\gamma' j}\Delta\varphi_{\gamma' j} = T_{\gamma i} + \sum_{\gamma' j}\mathcal{H}_{\gamma i,\gamma' j}\Delta\varphi_{\gamma' j} = 0\,. \tag{2.70}$$

Inverting the Hessian $\mathcal{H} = \{\mathcal{H}_{\gamma i,\gamma' j}\}$ a new set of $\Delta\varphi_{\gamma i}$ can be easily calculated:

$$\Delta\varphi_{\gamma i} = -\sum_{\gamma' j}\mathcal{H}^{-1}_{\gamma i,\gamma' j}T_{\gamma',j}\,, \tag{2.71}$$

and a new spin configuration can be generated. The Newton-Raphson method converges to the local minimum if the Hessian $\mathcal{H}$ is positive definite. In our implementation at the end of every line search of the conjugate gradient procedure the Hessian was checked and if all the eigenvalues were positive the optimization method was continued with the Newton-Raphson method.

Chapter 3

Magnetic anisotropy energy in ultrathin films

In this Chapter I am going to present the results for ultrathin layers obtained by metadynamics simulations. First I summarize the background of magnetic anisotropy energy (MAE), spin reorientation transitions (SRTs). Then first I present the results on the temperature dependence of the MAE of model systems [92] which helps to understand the method for the later results. It is followed by the results on the SRTs in the model systems [92], and in the Fe_n/Au(001) [92, 93] and Fe_2/W(110) [92, 94] systems. The effect of the DMI on this system is further investigated [94].

3.1 Background

3.1.1 The magnetic anisotropy energy

General properties and experiments The key property of a ferromagnetic sample is the direction of the magnetization, and the magnetic anisotropy is the quantity which determines the easy direction. With respect to its origin we distinguish different types of anisotropies, such as the magnetocrystalline anisotropy (MCA), due to the spin–orbit-coupling, and shape anisotropy (SA) which is originated from the magnetic dipole-dipole interaction. It is worth mentioning that the pseudo dipolar coupling also due to the spin–orbit coupling may also contribute to the shape anisotropy. It is a common idea to divide the anisotropy into so-called volume and surface anisotropies. This way the effective anisotropy can be described by the following phenomenological expression [6]:

$$K_1^{\text{eff}} = \widetilde{K}_1^V + \frac{K_1^S}{t}\,, \tag{3.1}$$

where $\widetilde{K}_1^V$ is the volume contribution (energy per unit volume), which includes the shape anisotropy, K_1^S is the surface contribution (energy per unit surface), and t is

the thickness of the film. In bulk system the former one dominates. For thin films the shape anisotropy prefers in-plane ferromagnetic orientation. In-plane anisotropy is used for longitudinal recording magnetostrictive and inductive heads, and media for magnetic-field sensors [95]. While in thin layers the surface contribution can lead to the perpendicular magnetic anisotropy (PMA) (e. g. FePt, CoPt compounds [96]). The PMA is used in high density data storage.

This picture is also very useful in the study of thickness driven spin reorientations, since it gives a simple explanation for the phenomenon. The volume part – which is dominated by the shape anisotropy – favours magnetization parallel to the plane of the surface, while the surface contribution prefers magnetization perpendicular to the plane. Since these two change oppositely with the change of the film thickness t, at one specific value the effective anisotropy changes sign. While this work is not about thickness driven SRTs, but the idea of competing anisotropies can also be used in temperature driven phenomena.

Techniques to measure MAE There are many experimental techniques to determine the magnetic anisotropy of ultrathin films and nanostructures, such as the ferromagnetic resonance (FMR) [97] experiments, the Brillouin light scattering (BLS) [98] or the torsion oscillation magnetometry (TOM) [6, 99]. The former two are based on the fact that the magnetic anisotropy has a direct impact on spin dynamics, while the later one is measuring the mechanical torque. Unfortunately all these methods require ultrahigh vacuum for appropriate measurements. The magneto-optical Kerr-effect (MOKE) measurement are also commonly used [100]. This method is based on the magneto-optical response upon reflection of polarized light from a ferromagnetic sample. Since the polarization and the intensity of the reflected light depend on the relative direction of the optical plane and the magnetization of the sample the magnetization can be determined in the different directions. This can also be used to discover spin reorientation transitions [19, 101, 102].

Table 3.1: Magnetic anisotropy energy in some systems.

System	MAE (meV/atom)
bcc Fe	0.0035 [103]
hcp Co	0.035 [103]
fcc Ni	-0.0004 [103]
CoPt (th)	1.052−1.782[95]
CoPt (exp)	1.451−1.665[95]
$L1_0$FePt	0.373 [104]
$L1_0$FePd	0.133 [105]

The typical order of the MCA of cubic 3d-tranisition bulk metals is only a μeV/atom [103]. In the case of ultrathin films it can be orders of magnitude larger and reach the meV/atom value. This increase is originated to the interface anisotropy contributions, which appear due to the different atomic environment near the interface. Some typical values are reported in Tbl. 3.1.

Temperature dependence of the MAE The anisotropy energy K is defined in terms of the dependence of the free energy on the direction of the magnetization, which can be expanded into power series. For cubic system this takes the following form:

$$F = K_0(T) + K_1(T)\left[\cos^2\alpha\cos^2\beta + \cos^2\beta\cos^2\gamma + \cos^2\gamma\cos^2\alpha\right] + \\ + K_2(T)\cos^2\alpha\cos^2\beta\cos^2\gamma + \dots\,, \tag{3.2}$$

where α, β, and γ are the angles between the magnetization vector and the crystallographic axes. The theoretical analysis of the anisotropy was already started in 1936, when Akulov presented the 10th power law, using a simple classical argument [106]:

$$K_1(T)/K_1(0) \approx \left[M(T)/M(0)\right]^{10}\,, \tag{3.3}$$

where $M(T)$ is the magnetization of the system. Comparing this theory with experiments on Fe concluded, that this law is accurate up to $T \approx 0.65\,T_\mathrm{C}$, where T_C denotes the appropriate Curie temperature. Later Zener generalized this law to the $\ell(\ell+1)/2$ power law [107]. This work was followed by Callen and Callen [108]. Their work on the MCA gave two limits:

$$\frac{K_\ell(T)}{K_\ell(0)} \approx \left[\frac{M(T)}{M(0)}\right]^{\ell} \qquad T > T_\mathrm{C}\,, \tag{3.4}$$

$$\frac{K_\ell(T)}{K_\ell(0)} \approx \left[\frac{M(T)}{M(0)}\right]^{\ell(\ell+1)/2} \qquad T \ll T_\mathrm{C}\,, \tag{3.5}$$

with a continuous transition in between. This implies that for on-site uniaxial anisotropy, i. e. $\ell = 2$, the MAE should exhibit a $K(T) \propto M(T)^3$ scaling. For the two-ion terms they gave the same low and high temperature limits.

In case of strongly itinerant magnetic systems both the on-site and the two-site anisotropy should be present in the spin model, and the scaling behaviour of the MAE can be remarkably different than for only the on-site anisotropy [109, 110].

The Dzyaloshinksy–Moriya interaction (DMI) induced anisotropy energy In simulations the different parameters of the spin model play the role of the different

anisotropies. Let's consider the second order classical spin Hamiltonian introduced in Eq. (2.32):

$$H = \sum_{i \neq j} \mathbf{s}_i^{\mathrm{T}} \mathbf{J}_{i,j} \mathbf{s}_j + \sum_i \mathbf{s}_i^{\mathrm{T}} \mathbf{K}_i \mathbf{s}_i \,. \tag{3.6}$$

First principle calculations showed [111], that the uniaxial MCA depends very sensitively on the type of the surface, this way, more generally the onsite anisotropy $\mathbf{K}$ plays the role of the MCA in the spin models. The resolution of the $\mathbf{J}_{ij}$ exchange-coupling tensor [42] gives two anisotropic terms (see Sec. 2.2). The symmetric isotropic term describes the classical dipolar and SOC-induced pseudo-dipolar anisotropy contributions. This two-ion term is connected to the shape anisotropy. Finally the third, antisymmetric part, which is connected to the DMI does not contribute to the anisotropy energy of a collinear magnetic configuration at zero temperature. Although both the MCA and the DMI are attributed to the SOC, they typically compete with each other since the former tends to align all spins along a preferential direction, while the latter opens a finite angle between the magnetic moments. However, in inhomogeneous and disordered systems the DMI may also enhance the anisotropy field, such as in spin glasses containing nonmagnetic heavy metal impurities and displaying a noncollinear magnetic configuration [112, 113], or due to the spin canting at the edges of nanomagnets [114]. In Ref. [29], it has been shown that thermal fluctuations and spin correlations lead to the emergence of a DMI-induced anisotropy term even in homogeneous ferromagnetic systems.

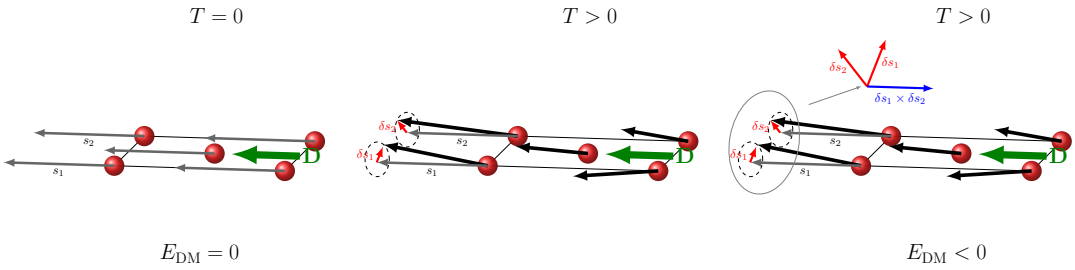

FIGURE 3.1: Left to right: The mechanism explaining the DMI induced anisotropy energy on a bcc (110) lattice. At $T = 0$ with ferromagnetic ordering the DMI energy contribution is zero. At finite $T > 0$ temperature small $\delta\mathbf{s}$ fluctuations emerge, which have minimal energy if the ordering is parallel to the DM vector, causing an effective anisotropy parallel with D.

This mechanism is explained on Fig 3.1. As an example let's consider a bcc(110) lattice with easy x axis and a DM vector $\mathbf{D}$ parallel to the x direction. At zero temperature the configuration is collinear, but at finite temperature, the spins minimize their free energy by fluctuating around this equilibrium direction. So among the higher orders of the DM spin–spin interactions appears a term which is minimal

if the spins are parallel to the DM vector. Thus effectively an in-plane anisotropy term appears, which can be estimated by the following formula on a spin lattice:

$$K_{\mathrm{DMI}} = \frac{m}{2} \sum_{p,q} \sum_{j} \mathbf{D}_{p0,qj} \cdot \langle \mathbf{s}_{p0} \times \mathbf{s}_{qj} \rangle \ , \tag{3.7}$$

where $\mathbf{s}_{qj}$ is a unit vector pointing to the magnetization direction in layer q at site j, m is the overall dimensionless magnetization of the whole lattice, normalized to $m = 1$ at zero temperature, $\mathbf{D}_{p0,qj}$ is a DM vector between the reference 0 site in layer p and site j in layer q, and $\langle \mathbf{s}_{p0} \times \mathbf{s}_{qj} \rangle$ corresponds to the vector chirality. Since the DMI energy contribution reads $\mathbf{D}_{pi,qj}(\mathbf{s}_{pi} \times \mathbf{s}_{qj})$, the scalar product $\mathbf{D}_{p0,qj} \cdot \langle \mathbf{s}_{p0} \times \mathbf{s}_{qj} \rangle$ will be negative when summed up over all neighbours in order to minimize the free energy.

Free energy may be gained if the magnetization is oriented parallel to the DM vector, since the chiral fluctuations have to take place in a plane perpendicular to both the magnetization and the DM vector, as written before.

3.1.2 Spin reorientation phase transitions

The reorientation of the magnetization direction is a common phenomenon. As the easy direction is coupled to the effective anisotropy, with the change of the preferred direction of the anisotropy energy results in the SRT. Since the total magnetic anisotropy comes from multiple components, which all depend differently on external parameters, such as the temperature and the film thickness, the overall anisotropy can easily change its easy direction.

The first discovery is connected to NiFe(111)/Cu(111) films [6], where it was found that if the layer thickness is lower than a threshold value, then the surface anisotropies force the magnetization along the surface normal. As mentioned before this can be interpreted with Eq. (3.1), where volume and surface anisotropy terms are separated, and it is clear to see, that with different signs of K^{V} and K^{S}, with the increase of the film thickness the effective anisotropy changes its sign. Later it was examined in several other thin films, such as fcc Fe/Cu(001) [115–117], bcc Fe/Ag(001) [118], hcp Co/Au(111) [119–121], Fe/Au(001) [18, 19], and Fe/W(110) [63, 64, 122]. From these many possibilities the most interesting ones for us are the Fe/Au(001) and Fe/W(110) systems, because in these the reorientation occurs below 3 and 2 atomic layers, respectively, which can be simulated more easily than about 7 atomic layers for the Fe/Ag(001) case. Here it has to be mentioned that in several cases the critical thickness is at non integer layer numbers, which

in experiments means that steps, and islands are present on the sample, which this way has a varying thickness. This feature cannot be considered in our simulations.

Temperature driven SRTs are as common as thickness driven ones. Usually if the layer thickness is close to the critical value, the effect caused by the increase of the temperature is enough for the emergence of the SRT. This happens in $Fe_{4.3}$/Ag(001) [101], Fe/Cu(001) [123] and Fe_2/W(110) [122]. An explanation behind this, is that the different temperature dependence of on-site and two-site anisotropies can change the competition which set the ground state easy direction. Udvardi *et al.* made a mean field calculation [124] for a bilayer with two-site and uniaxial on-site anisotropies. They found that the mean field approximation provides different transition temperatures for the in-plane (T_x), and normal-to-plane (T_z) magnetizations. The larger of these two is associated with the Curie temperature T_C of the system. An out-of-plane to in-plane SRT can occur when the ground state magnetization is out of plane and $T_z < T_x = T_C$. For a reversed SRT the ground state magnetization must be in-plane and $T_x < T_z = T_C$. In practice this later case is more rare, our studies concentrate on out-of-plane to in-plane reorientations.

3.2 Peculiarities of the simulation of the magnetic anisotropy energy

For examining the MAE of thin films a natural choice for collective variable (CV) is the z (normal-to-plane) component of the normalized magnetization:

$$\eta = M_z/M, \qquad \text{where } M_z = \sum_i s_{zi}, \text{ and } M = \left| \sum_i \mathbf{s}_i \right| . \tag{3.8}$$

The values of the CV chosen for a Heisenberg spin model must be obviously within the interval of $[-1, 1]$ and the free energy has a discontinuity at the boundaries which can not be accurately reproduced by a sum of finite-width Gaussians as it is detailed in Refs. [85, 125]. In order to eliminate this numerical problem, the procedure proposed by Crespo *et al.* [85] has been modified in the following manner: Whenever the bias potential is updated, an extra Gaussian with the same width and height is added out of the physically relevant interval of the CV:

$$\begin{aligned} V_{\text{bias}}(\eta, t+\tau) &= V_{\text{bias}}(\eta, t) + V_{\text{G}}(\eta - \eta_{\text{act}}) \\ &+ \begin{cases} V_{\text{G}}(\eta - 2 + \eta_{\text{act}}) & \text{if } \eta > 0 \\ V_{\text{G}}(\eta + 2 + \eta_{\text{act}}) & \text{if } \eta < 0 \end{cases} , \end{aligned} \tag{3.9}$$

where $V_{\mathrm{G}}(\eta)$ is the Gaussian potential given in Eq. (2.60). This scheme clearly makes the bias potential continuous at $\eta = \pm 1$. It should be noted that $V_{\mathrm{bias}}(\eta)$ does not go smoothly to zero in the nonphysical region, but this part of the CV is never sampled during the simulation. In order to explore the free energy surface along the CV multiple walkers metadynamics [126] was applied. The simulations were done simultaneously on typically four independently started replicas each contributing equally to the growth of a joint bias potential.

The parameters of the bias potential were optimized for each system under consideration. The half width σ determines the grid on the space of the CV, where the bias potential is sampled. In general, we chose $\sigma = 0.03$ making sufficient to sample 150 points in the $[-1:1]$ interval of the CV in order to get a smooth curve for the free energy. The value of the meta temperature T_m depends on the Curie temperature. Obviously, in the high T_{m} limit the normal (non-tempered) metadynamics is regained and the bias potential will not converge. If T_{m} is too small then the convergence will be very slow. In the present study a few times the Curie temperature has been used for T_{m}. The parameter w_0 should be chosen considerably smaller than the anisotropy energy of the whole lattice.

The magnetic anisotropy energy (K) is defined as the difference of the free energy for the normal-to-plane and in-plane spin configurations, which fits the same difference in the bias potential:

$$K(T) = V_{\mathrm{b}}(T, \eta = 1) - V_{\mathrm{b}}(T, \eta = 0)\,, \tag{3.10}$$

where $\eta = 1$ value belongs to the normal to plane configuration and $\eta = 0$ refers to the in-plane magnetic configuration. In Fig. 3.2(a) and Fig. 3.2(b) well converged bias potentials are shown. The bias potential in Fig. 3.2(a) represents a normal-to-plane ground state while Fig. 3.2(b) belongs to a canted magnetic configuration. The flat region in the middle of the bias potential in Fig. 3.2(c) indicates that the simulation could not cover the whole configurational space.

Unfortunately, when more coupling parameters are included in the spin model, despite of all our efforts, the bias potential will become noisy especially around $\eta = 1$ and $\eta = 0$. The former one is treated by the upper mentioned extension of the CV, but in the middle η range another effect is present: if the linear size of the sample is large enough there is a possibility of magnetic domains to form. This is problematic, since the in-plane ferromagnetic configuration will not be reached in the simulation. The sufficient sample size for this problem is reached, when there are enough spins to form 2 domain walls (in the case of periodic boundary conditions, which was used). The typical size of a domain wall can be estimated by $\sqrt{J/K}$. So if the anisotropy

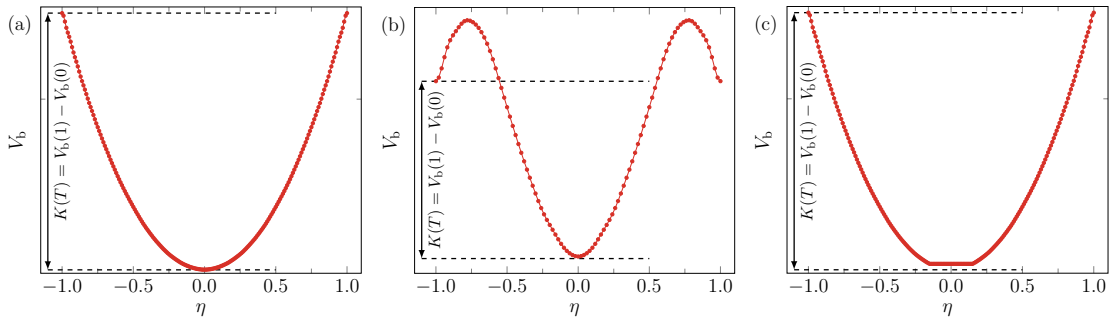

FIGURE 3.2: Typical bias potential at the end of metadynamics simulations. (a) The ground state is a normal-to-plane configuration. (b) The ground state is a canted configuration. (c) The ground state is a normal-to-plane, but the in-plane configurations are not reached.

is around $0.01\,J$ (which is the typical magnitude at zero temperature), the critical size will be around $10 - 20$ spins, which is in the order of the typical linear size of the lattice in the simulations.

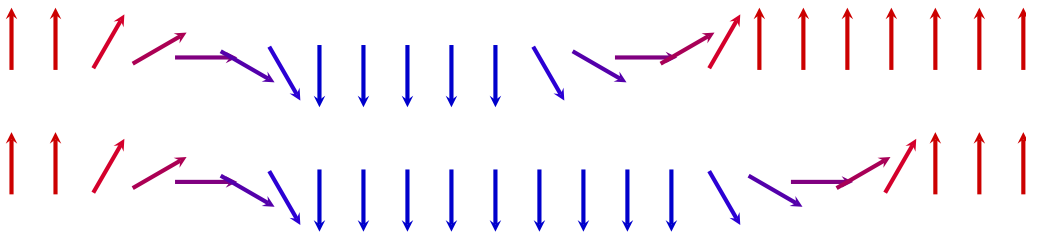

FIGURE 3.3: A schematic example of domain walls with different distance from each other in the magnetic configuration.

To understand why domain walls mean a horizontal region in the $V_\mathrm{b}(\eta)$ curve, imagine now two simple configurations (see Fig 3.3) with the same domain walls, but at different positions. As the domain walls are far enough from each other, the energy of the system does not change as the domain wall is shifted. On the other hand this shift clearly changes value of the CV, since the number of up and down spin changes. These two effects combined mean a horizontal section in the bias potential, which can be seen on Fig. 3.2(c).

In order the avoid this problem and to obtain the good K value, we approximate the $V_\mathrm{b}(\eta)$ function with a polynomial:

$$V_\mathrm{b}^\mathrm{fit}(\eta) = a\eta^4 + b\eta^2 + c\,, \tag{3.11}$$

and restrict the fitting between $\eta_1 = -0.9$ and $\eta_2 = -|\eta_\mathrm{DW}|$ value, where η_DW is the value where the domain walls appear at this temperature, which value can be measured easily by looking at the $V_\mathrm{b}(\eta)$ function. This way effectively the magnetic

anisotropy energy K becomes:

$$K = V_{\mathrm{b}}^{\mathrm{fit}}(1) - V_{\mathrm{b}}^{\mathrm{fit}}(0) = a + b\,. \tag{3.12}$$

Based on this, we can say that the MAE is proportional to the curvature of the bias potential curve.

3.3 Temperature dependent MAE from different origins

Spin model

For the initial model calculations we used a very simple case of the general Heisenberg model in Eq. (2.32) on a (100) simple cubic lattice:

$$H = -\frac{1}{2}\sum_{\langle i,j\rangle}\left[J\mathbf{s}_i\mathbf{s}_j - d\left(\mathbf{s}_i\mathbf{e}_z\right)\left(\mathbf{s}_j\mathbf{e}_z\right)\right] - \sum_i \lambda\left(\mathbf{s}_i\mathbf{e}_z\right)^2\,, \tag{3.13}$$

where $\mathbf{s}_i$ is the normalized magnetic moment vector at site i, J is the isotropic exchange coupling, d is the anisotropic part of the exchange coupling, λ is a uniaxial on-site anisotropy, whose magnitude is the same in every site of the layer, and $\mathbf{e}_z$ is a unit vector pointing to the normal-to-plane [001] direction. The system is a monolayer and only the nearest neighbour interactions are considered in the calculations.

First let us investigate the zero temperature behaviour. The magnetic moment can be written as the following unit vector:

$$\mathbf{s}_i = \begin{pmatrix} \sin\vartheta_i\cos\varphi_i \\ \sin\vartheta_i\sin\varphi_i \\ \cos\vartheta_i \end{pmatrix}\,, \tag{3.14}$$

where ϑ_i and φ_i denote the polar angle with respect to the normal-to-plane direction z and azimuthal angle with respect to the in-plane direction x at site i, respectively. If we assume a ferromagnetic ordering, the energy becomes the following:

$$E = -2J + (2d - \lambda)\cos^2\vartheta\,. \tag{3.15}$$

Depending on the $(2d - \lambda)$ difference the ground is normal-to-plane, if $\lambda > 2d$ and in-plane otherwise. Note that the absence of variable φ shows that all directions are

energetically equivalent in the plane, but this does not prevent the clear distinction of states regarding M_z.

The scale of the anisotropy parameters can be based on experimental values (see 3.1.1 Tbl. 3.1): the uniaxial anisotropy constant for a broad scale of ultrathin films is in the range of $10 - 200\,\mu$eV. The Curie temperature of an ultrathin film of transition metals is few hundreds of Kelvins and so the corresponding effective exchange coupling J is a few tens of meV. These two set the value of the relative anisotropy of the exchange coupling (d/J) and of the uniaxial on-site anisotropy constant (λ/J) between 0.001 and 0.01 for the simulations.

Metadynamics simulations

The aim of the first simulations on the model systems was to reproduce the temperature dependence of the MAE predicted by the Callen–Callen theory (see Sec. 3.1.1). As the energy contribution associated to the different types of anisotropy terms i. e. the λ on-site, and the d two-site anisotropy may have different temperature dependences, the first model is more specified and only contains one them, namely first only an on-site anisotropy λ.

In the first simulation the spin model of the monolayer consists only of an isotropic ferromagnetic nearest neighbour exchange coupling $(J > 0)$ and of a uniaxial on-site anisotropy constant with easy axis perpendicular to the plane $(\lambda > 0)$. With such parameters the ground state of the system is ferromagnetic with a normal-to-plane orientation of the magnetic moments.

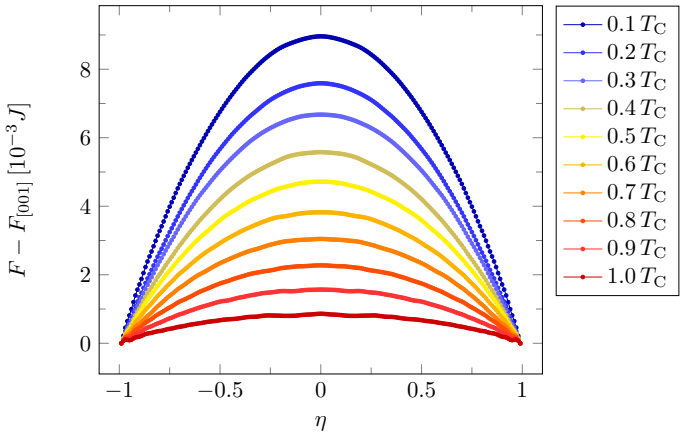

FIGURE 3.4: Free energy difference of normal-to-plane and in-plane magnetic configurations normalized to one spin of a 32×32 monolayer with isotropic nearest neighbour exchange coupling $J > 0$ and a uniaxial on-site anisotropy of $\lambda = 0.01\,J$ at different temperatures. The simulations were performed with the parameters $T_\mathrm{m} = 10\,J$, $w_0 = 0.02\,J$ and $\sigma = 0.03$.

The free energy obtained from the metadynamics simulations is depicted in Fig. 3.4. It shows that the free energy has a quadratic dependence on the collective variable (CV), which is in a good agreement with the $\cos\vartheta$ dependence in Eq. (3.15). The parabolic behaviour of the free energy is retained in the whole temperature range below the paramagnetic phase transition. The free energy has a single maximum at $\eta = 0$ referring to an in-plane configuration and it has two minima at $\eta = \pm 1$ representing the two opposite normal-to-plane magnetic orientations. This agrees with the aforementioned normal-to-plane easy orientation of the moments.

The MAE – calculated using Eq. (3.12) as presented in Sec. 2.3.2 – is plotted on the left side of Fig. 3.5. As the temperature is increasing the curvature of the free energy as a function of CV is gradually decreasing and it tends to zero above the Curie temperature. Here the Curie temperature (T_C) is identified as the temperature corresponding to the maximum of the specific heat identified in another independent Monte Carlo simulation. Although the Curie temperature scales with the system size, it was chosen to be compatible with the size of the system for which the MAE was calculated.

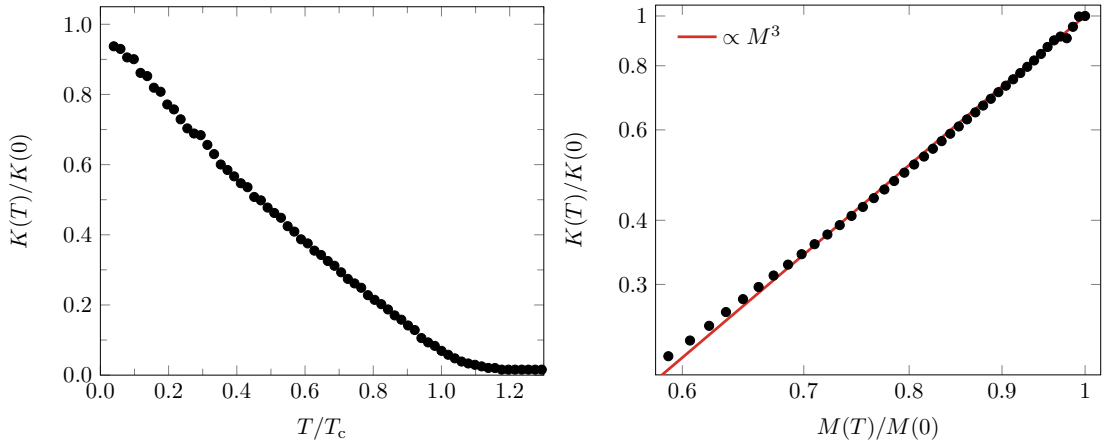

FIGURE 3.5: Left side: Temperature dependence of the magnetic anisotropy energy $K(T)$ of a monolayer with isotropic nearest neighbour exchange coupling $J > 0$ and a uniaxial on-site anisotropy of $\lambda = 0.01\,J$. Right side: Log-log plot of the magnetic anisotropy energy of the same system as a function of the magnetization. Note that both the MAE and the magnetization are normalized to zero temperature value. The simulations were performed on a lattice of 32×32 spins with the parameters $T_\mathrm{m} = 10\,J$, $w_0 = 0.02\,J$ and $\sigma = 0.03$.

The magnetic anisotropy in Fig. 3.5(left) is almost linearly decreasing with the temperature similarly to the results obtained by using constrained Monte Carlo simulations [127] for uniaxial anisotropy. The non-zero value of the magnetic anisotropy above the Curie temperature is the consequence of the finite size of the system. On

the right side of the same Fig. 3.5 the MAE is plotted against the magnetization on a log-log mesh. As can be seen, at low temperatures, i. e. at high magnetization, the results on the anisotropy energy K show an excellent agreement with the M^3 scaling behavior predicted by Callen and Callen [108].

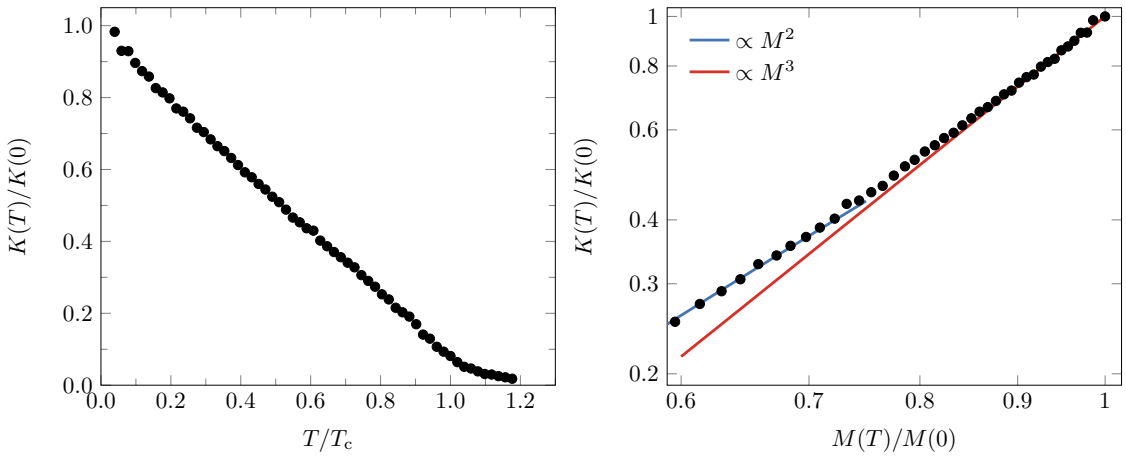

FIGURE 3.6: Left side: Temperature dependence of the magnetic anisotropy energy $K(T)$ of a monolayer of a 32×32 with anisotropic nearest neighbour exchange coupling $J > 0$, $d = -0.01\,J$ and zero on-site anisotropy $\lambda = 0$ Right side: Log-log plot of the magnetic anisotropy energy of the same system as a function of the magnetization. Note that both the MAE and the magnetization are normalized to zero temperature.

Similar simulations were also performed in the case when simply an anisotropic exchange $d < 0$ was included in the model instead of the λ uniaxial on-site anisotropy. The results of these simulations can be seen in Fig. 3.6. The temperature dependence is very similar to the case of a uniaxial on-site anisotropy. A clear difference can be observed when the MAE is plotted against the magnetization. At very low temperatures, i. e. when $M(T)/M(0) \approx 1$, the system behaves as for the other case, but below $M(T)/M(0) \approx 0.8$ the exponent γ in the relationship $K(T) \propto M(T)^\gamma$ changes from three to two. The occurrence of the exponent $\gamma = 2$ in the low-temperature scaling of the MAE was explored in earlier experimental [128] and theoretical studies [109, 110, 129] for FePt alloys.

An important message of the comparison of the two cases is that the MAE attributed to the on-site term decays faster with the temperature than the MAE contribution originated from the anisotropic exchange, which in particular cases can lead to a spin reorientation transition.

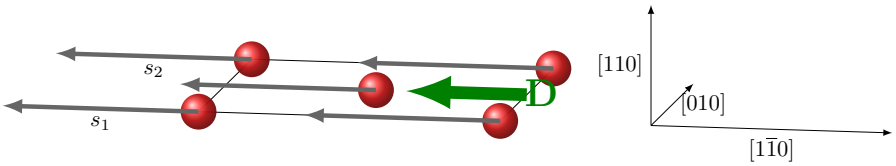

FIGURE 3.7: The ground state spin configuration (grey) of the model system used to investigate the effect of the DMI (green) induced anisotropy term. The [1$\bar{1}$0], [001] and [110] vectors refer to the respective crystallographic directions.

The Dzyaloshinsky-Moriya interaction induced magnetic anisotropy energy

Opposite to the previous two cases, the appearance of DMI induced anisotropy requires a more sophisticated model. As introduced in Sec. 3.1.1 let's consider a magnetic monolayer on a bcc (110) surface. The lower symmetry means that instead of the uniaxial on-site anisotropy, a biaxial one with different λ_x and λ_y constants are needed, and an in-plane DM vector $\mathbf{D}$ is included in the spin Hamiltonian:

$$H = -\frac{1}{2}\sum_{i,j} J\mathbf{s}_i\mathbf{s}_j + \sum_i \lambda_x \left(\mathbf{s}_i\mathbf{e}_x\right)^2 + \sum_i \lambda_y \left(\mathbf{s}_i\mathbf{e}_y\right)^2 + \sum_{i,j} \mathbf{D}\left(\mathbf{s}_i \times \mathbf{s}_j\right) . \tag{3.16}$$

The x, y, z axes correspond to the [1$\bar{1}$0], [001] and [110] crystallographic directions, respectively. The zero temperature energy in a ferromagnetic state is the following energy:

$$E = -2J + \lambda_x \sin^2\vartheta\cos^2\varphi + \lambda_y \sin^2\vartheta\sin^2\varphi\,. \tag{3.17}$$

The direction of the minimal energy configuration depends on the anisotropy terms. If $\lambda_x > 0$ and $\lambda_y > 0$ the easy direction will be normal-to-plane. If one of them is negative then it will set the easy magnetic direction to the corresponding direction. For the simulations $\lambda_x/J = -0.005$, $\lambda_y/J = 0.01$, and $\mathbf{D}/J = (-0.05; 0; 0)$ were chosen. The negative on-site anisotropy in direction x and positive in direction y makes it clear that the easy direction is the in-plane x. The finite temperature induced DMI anisotropy is expected to prefer the same alignment.

The metadynamics simulations were performed on a 64×64 lattice with the usual parameters (see in Sec 2.3). To separate the effect of the DMI from the other contributions two separate series of simulations were performed, first with the whole set of coupling parameters (J, λ_x, λ_y, D), then the DM vectors were omitted. This way we got two curves of the magnetic anisotropy energy, whose difference is the effective DMI induced anisotropy energy. These curves and their difference are

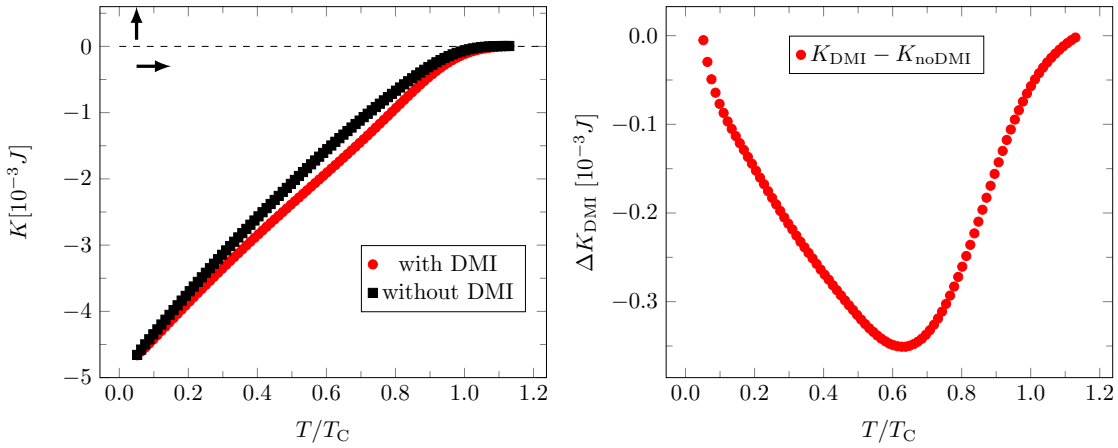

FIGURE 3.8: Temperature dependent magnetic anisotropy energy per atom of a model system desribed by Eq. (3.16), with and without including the DM term. The right side figure shows the difference of the two anisotropies, which equals the DMI induced anisotropy.

shown in Fig. 3.8.

First it is clear to see – that as predicted–, this DMI induced term prefers the in-plane x direction. Secondly we can discuss the temperature dependence of this anisotropy term. Since its origin is the finite temperature fluctuation of the magnetic moments, at low temperatures it has a small value and becomes larger and larger with T. In the middle T range it reaches its maximum, and as the whole system turns paramagnetic, this term also vanishes. This behaviour is fundamentally different from the ones originated from the anisotropy of the exchange coupling or the on-site anisotropies, since opposite to them it is not a monotonically decreasing function of the temperature but has a maximum at a temperature far from 0 and also from the Curie temperature of the system.

3.4 Spin reorientation transitions

Now that all anisotropy types were investigated individually the next step is to put them together to investigate the more interesting behaviour of the spin reorientation transitions. First we study the simplest case of a monolayer with two competing anisotropies of λ and d, then comes the investigation of the more feature-rich bilayer.

3.4.1 Case of a monolayer

Eq. (3.13) gives a model of a monolayer with the two competing anisotropies: the on-site uniaxial anisotropy λ and the anisotropy of the exchange coupling d. Considering a single square lattice, with only the four nearest-neighbour couplings, in case of

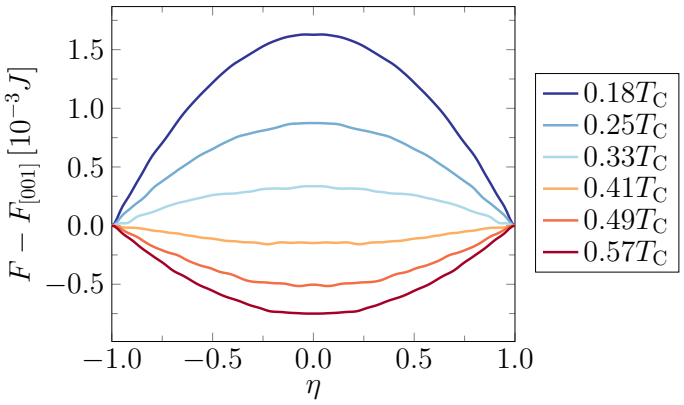

FIGURE 3.9: Free energy of a model monolayer as a function of collective variable $\eta = M_z/M$ measured from the free energy of a normal-to-plane magnetized configuration. The free energy values are normalized to one spin. The metadynamics simulations were performed on a 64×64 rectangular lattice with competing on-site and nearest-neighbour two-site anisotropies, $\lambda = 0.05375\,J$ and $d = 0.025\,J$, respectively, see Eq. (3.13).

$\lambda > 2d$ the ground state will be normal-to-plane ferromagnetic as Eq. (3.15) showed. Since the MAE contribution from the onsite term decays faster than the one from the two-site term, if $\lambda - 2d$ is not too large, the difference can be overcome and a temperature induced normal-to-plane to in-plane SRT can occur.

Metadynamics simulations

For the simulations we used $\lambda = 0.05375\,J$ and $d = 0.025\,J$ as anisotropy constants. In this case the $\lambda - 2d$ difference is 0.00375 J, which is expected to be small enough for a SRT. Fig. 3.9 shows the free energy as a function of the CV, and the energy difference of normal-to-plane and in-plane configurations (similarly to Fig. 3.4). The free energy preserved the parabolic behaviour also for this case of mixed anisotropies. At low temperatures it has two minima, corresponding to $\eta = M_z = \pm 1$, i. e. to a normal-to-plane configuration, as expected. Yet as the temperature is increasing the curvature of the free energy becomes smaller and smaller, and at one point it changes sign and the minimum of the free energy moves to $\eta = M_z = 0$, i. e. to an in-plane magnetic orientation. This change can also be seen on the magnetic anisotropy energy curve in Fig. 3.10. It is positive at low temperatures, and becomes zero at a transition temperature T_r.

Here it is worthwhile to mention that if the magnetization turns into the plane the system will have a gap-less magnetic excitation spectrum and long range magnetic order will no longer exist according to the well-known Mermin-Wagner theorem [130]. Still, the magnetic anisotropy energy can be defined as the free energy difference between the normal-to-plane and in-plane magnetic orientations. Looking back to Fig. 3.10 the free energy demonstrates a first order phase transition. Moschel and

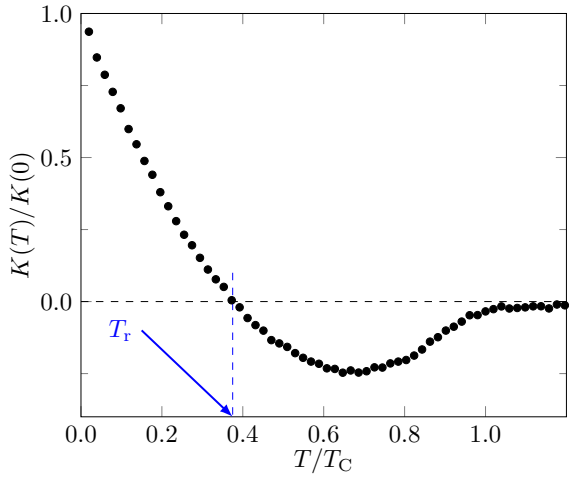

FIGURE 3.10: Magnetic anisotropy energy $K(T)$ normalized to its zero temperature value of a model monolayer system as a function of the temperature. The metadynamics simulations were performed on a 64×64 rectangular lattice with competing on-site and nearest-neighbour two-site anisotropies, $\lambda = 0.05375\,J$ and $d = 0.025\,J$, respectively, see Eq. (3.13).

Usadel [131] using MC simulations and Fridman *et al.* [132] applying a Hubbard-operator technique also confirmed that a monolayer exhibits first order SRT.

3.4.2 Study of reorientation in a bilayer

Spin model

The increase of film thickness to a bilayer increases the number of anisotropy parameters to three (d, λ_1, λ_2). This enriches the phase diagram, now both first order and second order SRT can occur. As a model system we consider a minor expansion of the model in Eq. (3.13), a bilayer on an fcc (001) surface with nearest-neighbour interactions J and d, and on-site anisotropy parameter λ_p, where p is the layer index:

$$H = -\frac{1}{2}\sum_{p,q=1}^{2}\sum_{\langle i,j\rangle}\left(J\mathbf{s}_{pi}\mathbf{s}_{qj} - d\left(\mathbf{s}_{pi}\mathbf{e}_z\right)\left(\mathbf{s}_{qj}\mathbf{e}_z\right)\right) - \sum_{p=1}^{2}\sum_{i}\lambda_p\left(\mathbf{s}_{pi}\mathbf{e}_z\right)^2 . \tag{3.18}$$

A mean-field analysis of a similar model has been performed two decades ago by Udvardi *et al.* [124], where instead of the d anisotropy of the exchange coupling a dipole-dipole interaction was included. Since their part is similar in the models, the same steps can be made to set up the boundaries of the different regions of the phase space.

Zero temperature behaviour

At zero temperature we can suppose a uniform magnetization within each monolayer, whose direction not necessarily agrees, which can be described by the ϑ_i polar and φ_i azimuthal angle in layer i as defined in Eq. (3.14). In this case the energy of the system can be written as:

$$\begin{aligned} E = &- 4J + (2d - \lambda_1)\cos^2\vartheta_1 + (2d - \lambda_2)\cos^2\vartheta_2 \\ &- 4J[\sin\vartheta_1 \sin\vartheta_2 \cos(\varphi_1 - \varphi_2) + \cos\vartheta_1 \cos\vartheta_2] + 4d\cos\vartheta_1 \cos\vartheta_2 \,. \end{aligned} \tag{3.19}$$

This energy term is minimal, if the φ_1 and φ_2 azimuthal angles agree in the two layers. After this assumption we get the following expression:

$$\begin{aligned} E = &-4J + (2d - \lambda_1)\cos^2\vartheta_1 + (2d - \lambda_2)\cos^2\vartheta_2 \\ &- 4J\cos(\vartheta_1 - \vartheta_2) + 4d\cos\vartheta_1 \cos\vartheta_2 \,, \end{aligned} \tag{3.20}$$

In the case of uniform in-plane ($\vartheta_1 = \vartheta_2 = \vartheta = \pi/2$) and a normal-to-plane ($\vartheta_1 = \vartheta_2 = \vartheta = 0$) orientations the energy has extrema:

$$E(\vartheta = 0) = -8J + 8d - \lambda_1 - \lambda_2 \,, \tag{3.21}$$

$$E(\vartheta = \frac{\pi}{2}) = -8J \,. \tag{3.22}$$

Similar to the case of the monolayer, the energies of these two particular configurations coincide if $8d = \lambda_1 + \lambda_2$, which defines a line in the $\{\lambda_1, \lambda_2\}$ parameter space. In the vicinity of this line a canted magnetic configuration exists. The boundaries of the region of the canted states can be obtained from the stability condition:

$$\left| \frac{\partial^2 E}{\partial\vartheta_i \partial\vartheta_j} \right|_{\vartheta_i = 0, \pi/2} = 0 \,, \tag{3.23}$$

yielding the lower boundary line,

$$\left(J + d - \frac{\lambda_1^{\mathrm{l}}}{2}\right)\left(J + d - \frac{\lambda_2^{\mathrm{l}}}{2}\right) = (d - J)^2 \tag{3.24}$$

and the upper boundary line,

$$\left(J - 2d + \frac{\lambda_1^{\mathrm{u}}}{2}\right)\left(J - 2d + \frac{\lambda_2^{\mathrm{u}}}{2}\right) = J^2 \,. \tag{3.25}$$

Below the line given by Eq. (3.24), $\lambda_1 + \lambda_2 < \lambda_1^{\mathrm{l}} + \lambda_2^{\mathrm{l}}$, the ground state is in-plane ferromagnetic and above the line given by Eq. (3.25), $\lambda_1 + \lambda_2 > \lambda_1^{\mathrm{u}} + \lambda_2^{\mathrm{u}}$, it is

normal-to-plane ferromagnetic. These borders are visualised for the $d = 0.02\,J$ case in Fig. 3.11.

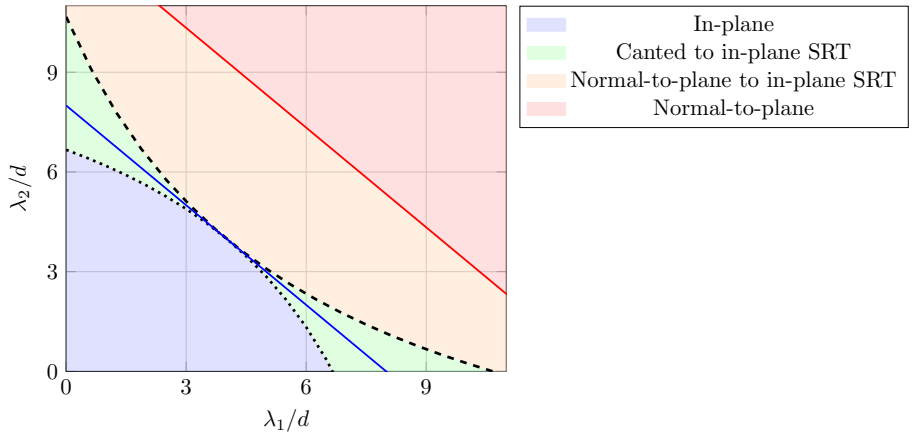

FIGURE 3.11: Ground states and possible SRTs of an fcc(001) ferromagnetic bilayer described by the model Hamiltonian Eq. (3.18) with nearest-neighbour exchange interactions, J and d, and uniaxial anisotropies, λ_1 and λ_2. The plot is restricted to the positive $\{\lambda_1, \lambda_2\}$ region, and the boundaries are calculated for the case of $d = 0.02\,J$. The solid blue line shows the boundary where the normal-to-plane and in-plane configuration have the same energy, while the region of canted ground states given by Eqs. (3.24) and (3.25) is shown with dotted and dashed lines. The upper red line bounds the area where a normal-to-plane to in-plane spin reorientation occurs according to mean-field theory (Eq. (3.35)). The differently colored regions correspond to ground states and SRTs shown in the legend.

Mean field estimation for finite temperature

At finite temperature the mean-field free energy of the bilayer can be expressed as:

$$F = \frac{4J}{2}\mathbf{M}^2 - \frac{4d}{2}(M^z)^2 - k_\mathrm{B}T\ln(Z_1) - k_\mathrm{B}T\ln(Z_2)\,, \tag{3.26}$$

where

$$Z_i = \int I_0(4J\beta M^x \sin\vartheta)\exp\left[4(J-d)\beta M^z\cos\vartheta\right]\exp\left[\lambda_i\beta\cos^2\vartheta\right]\sin\vartheta\,\mathrm{d}\vartheta\,, \tag{3.27}$$

$I_0(x)$ is the modified Bessel function of the first kind, while M_x and M_z are the x and z component of the whole magnetization of the bilayer, respectively.

The magnetization in the normal-to-plane z and in-plane x directions can be given with the following formulas:

$$M_x = \sum_{i=1}^{2} \frac{1}{Z_i} \int \sin\vartheta I_1(4J\beta M_x \sin\vartheta) \exp\left(\lambda_i \beta \cos^2\vartheta\right) \sin\vartheta \, \mathrm{d}\vartheta \,, \tag{3.28}$$

$$M_z = \sum_{i=1}^{2} \frac{1-\frac{d}{J}}{Z_i} \int \cos\vartheta \exp\left(4(J-d)\beta M_z \cos\vartheta\right) \exp\left(\lambda_i \beta \cos^2\vartheta\right) \sin\vartheta \, \mathrm{d}\vartheta \,, \tag{3.29}$$

where $I_1(x)$ denotes the the modified Bessel function of first order. As was shown in Ref. [124] the magnetization can go to zero either via an in-plane or via a normal-to-plane direction at temperatures, T_x and T_z, respectively, the higher of which can obviously be associated with the mean-field estimation of the Curie temperature T_C. Minimizing the free energy with respect to the magnetization of the system with the constraint $M_z = 0$ or $M_x = 0$ can give these temperatures.

A high temperature expansion ($\beta \to 0$), the series expansion of the Bessel functions $I_0(x)$ and $I_1(x)$, and a $z = \cos\vartheta$ variable replacement in Eqs. (3.27), (3.28) and (3.29) yield the following form:

$$Z_i = \int \exp\left(\lambda_i \beta z^2\right) \mathrm{d}z \tag{3.30}$$

$$M_x = \sum_{i=1}^{2} \frac{1}{Z_i} \int (1-z^2) 2J\beta M_x \exp\left(\lambda_i \beta z^2\right) \mathrm{d}z \,, \tag{3.31}$$

$$M_z = \sum_{i=1}^{2} \frac{1-\frac{d}{J}}{Z_i} \int 4(J-d)\beta M_z z^2 \exp\left(\lambda_i \beta z^2\right) \mathrm{d}z \,. \tag{3.32}$$

Finally for T_x and T_z this gives the following expressions to first order in λ_1 and λ_2:

$$k_\mathrm{B} T_z = \frac{8}{3}(J-d) + \frac{2}{15}(\lambda_1 + \lambda_2) \,, \tag{3.33}$$

$$k_\mathrm{B} T_x = \frac{8}{3}J - \frac{1}{15}(\lambda_1 + \lambda_2) \,. \tag{3.34}$$

Depending on the ground state magnetization and the value of T_z and T_x, spin reorientation transition is only going to happen of if the ground state magnetic orientation has lower critical temperature, e. g. out-of-plane to in-plane SRT occurs when the ground state magnetization is out of plane and $T_z < T_x = T_\mathrm{C}$, or reversed SRT occurs if the ground state magnetization is in-plane (or canted) and $T_x < T_z = T_\mathrm{C}$. In other cases the magnetization turns paramagnetic without changing its direction. If the two temperatures agree, then no reorientation can occur. In the parameter space $\{\lambda_1, \lambda_2\}$ this region is bounded by the line defined by Eq. (3.24)

and by the line where $T_x = T_z$:

$$\lambda_1 + \lambda_2 = \frac{40}{3} d \,. \tag{3.35}$$

The visualisation of the different regions for the $d = 0.02\,J$ case can be seen in Fig. 3.11.

Metadynamics simulations

Metadynamics Monte Carlo simulations are a perfect tools to explore the phase diagram of the model bilayer. The reorientation temperature can be determined by calculating the magnetic anisotropy energy curve and searching for the temperature where is crosses the zero value. Although e. g. according to *ab initio* calculations the anisotropy parameters λ_p and d can take both positive and negative values, in order to keep the MC simulations tractable, the investigations were similarly restricted to the positive quarter of the $\{\lambda_1/d, \lambda_2/d\}$ parameter space as previously in Fig. 3.11.

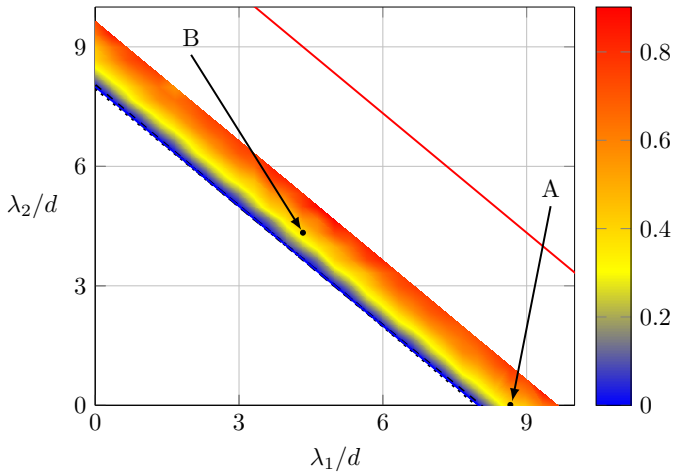

FIGURE 3.12: Phase diagram of an fcc (001) ferromagnetic bilayer described by the model Hamiltonian Eq. (3.18) with nearest-neighbour exchange interactions, J and d, and uniaxial anisotropies, λ_1 and λ_2. Similarly to Fig 3.11, now for the case of $d = 0.005\,J$, the solid blue line shows the boundary where the normal-to-plane and in-plane configuration have the same energy, while the region of canted ground states given by Eqs. (3.24) and (3.25) is comparable with the line width. The solid red line bounds the area where a normal-to-plane to in-plane spin reorientation occurs according to mean-field theory. This area becomes considerably narrower from metadynamics simulations as shown by the colored area. The color-bar to the right refers to $T_\mathrm{r}/T_\mathrm{C}$. For this case, the points A ($\lambda_1/d = 8.66$, $\lambda_2/d = 0$) and B ($\lambda_1/d = \lambda_2/d = 4.33$) are chosen for further investigations.

The phase diagram for $d = 0.005\,J$ is shown in Fig. 3.12. In this case, the region where canted ground states exist determined by Eqs. (3.24) and (3.25) is extremely narrow. The area where a normal-to-plane to in-plane SRT occurs provided by the metadynamics simulations (colored region) is considerably narrower than the

corresponding area predicted by the mean field theory (bounded by the blue and red solid lines). The coloring clearly demonstrates that the reorientation temperature T_r gradually approaches the Curie temperature as the sum of the uniaxial on-site anisotropy constants $\lambda_1 + \lambda_2$ is increasing, while parallel to the lines $\lambda_1 + \lambda_2 = \text{const.}$ it is almost unchanged. If the uniaxial on-site anisotropy is further increased after the reorientation temperature T_r approached the Curie temperature T_C, the system keeps its normal-to-plane ferromagnetic order till the ferromagnetic-paramagnetic phase transition.

The area of the canted ground states depends on the value of two-site anisotropy constant d. If it is increased, this area defined by Eqs. (3.24) and (3.25) becomes wider (compare Fig. 3.11 with $d = 0.02\,J$ and Fig. 3.12 with $d = 0.005\,J$). For further investigations we choose two specific points in the phase diagram: point A ($\lambda_1/d = 8.66$, $\lambda_2/d = 0$) representing a canted ground state, however, lying in the vicinity of the upper boundary line of this region (dashed line in Fig. 3.12) and point B ($\lambda_1/d = \lambda_2/d = 4.33$) corresponding to a normal-to-plane ferromagnetic ground state. For the first choice of (λ_1, λ_2) the magnetization of the system continuously turns into the plane as the temperature is increasing and, considering the normal-to-plane component of the magnetization as order parameter, the system undergoes a second order SRT. This is demonstrated in left subfigure of Fig. 3.13, where the free energy is shown as the function of the CV at different temperatures close to the reorientaion temperature T_r. At low temperatures the minima of the curve confirms the expected canted initial state, and below the reorientation temperature, $T_\mathrm{r}/T_\mathrm{C} \sim 0.45$, the magnitude of the minimum position of the free energy, η_min, decreases continuously with increasing temperature, while at the in-plane magnetization $\eta = 0$ there is a maximum in the free energy. Above the reorientation transition temperature the in-plane configuration belongs to the minimum of the free energy, that means the order parameter is identical to zero.

At point B in Fig. 3.13 the uniaxial anisotropy parameters λ_1 and λ_2 agree and no canted ground state exists for the bilayer, therefore, the mean-field description of temperature dependent magnetism becomes analogous with that of the monolayer. The results of metadynamics simulations show, however, some different features for the bilayer and the monolayer. According to Fig. 3.9 the SRT for the monolayer is discontinuous and the normal-to-plane and in-plane phases can not coexist. The free energies for the bilayer with anisotropy parameters $\lambda_1 = \lambda_2 = 4.33\,d$ are shown in right subfigure of Fig. 3.13. Below the reorientation temperature the free energy has minima at $\eta = \pm 1$ which correspond to a normal-to-plane average magnetization. As the temperature is increasing a local minimum of the free energy evolves to $\eta = 0$ referring to in-plane magnetization. In a small temperature range (3rd blue curve

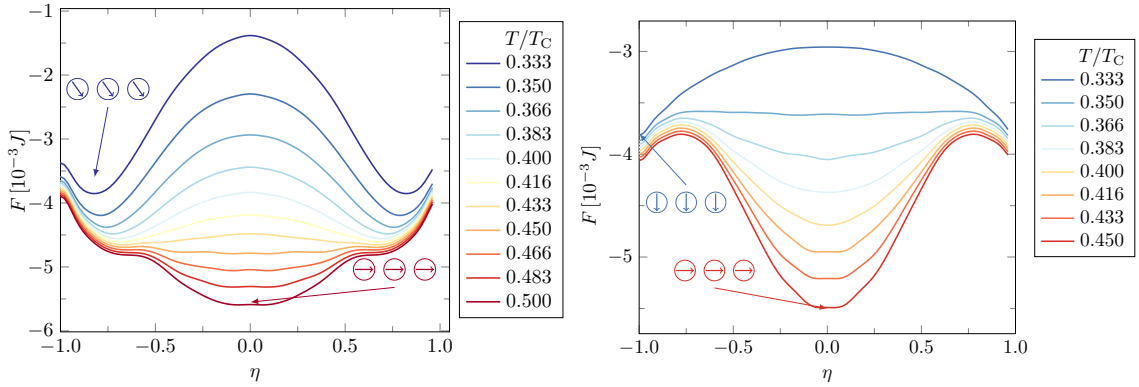

FIGURE 3.13: Free energy profiles from metadynamics simulations of a $2 \times 64 \times 64$ bilayer with nearest-neighbour exchange interactions. For the left figure $d = 0.05\,J$, and anisotropy constants $\lambda_1 = 8.66\,d$, $\lambda_2 = 0$ (point A in Fig. 3.12). The low temperature magnetic configuration is canted ($0 < \eta < 1$), while by increasing the temperature the system continuously turns into the phase with in-plane magnetization showing the nature of a second order phase transition. For the right figure $d = 0.05\,J$, and anisotropy constants $\lambda_1 = \lambda_2 = 4.33\,d$ (point B in Fig. 3.12). At low temperature the magnetization points normal to the plane ($\eta = \pm 1$), while at the reorientation temperature, $T_\mathrm{r} \sim 0.366\,T_\mathrm{C}$, it suddenly jumps to in-plane, as $\eta = 0$ becomes the minimum position of the free energy, displaying thus a first order phase transition.

on Fig. 3.9 left) this is only a metastable stable, which is separated from the global minimum at $\eta = \pm 1$ by a small barrier. Yet as the temperature is further increased the local minimum at $\eta = 0$ becomes the global maximum. The spin reorientation transition is, therefore, of first order as in the case of the monolayer but the phases with in-plane and normal-to-plane magnetization can coexist.

3.5 $\mathrm{Fe}_n/\mathrm{Au}(001)$

Ultrathin Fe layers on Au(001) substrate are the subject of extensive investigations especially in context of low-dimensional magnetism, see Ref. [19] and references therein. An Fe monolayer grown on Au(001) has often been referred as a prototypical two-dimensional ferromagnet. The film $\mathrm{Fe}_n/\mathrm{Au}(001)$ exhibits a normal-to-plane magnetic ground state for $n \leq 2$ and MOKE measurements showed that it undergoes a thickness driven spin reorientation, when the thickness of the Fe film increased to 2.3 monolayers [19]. Whereas the driving force of this spin reorientation is the magnetostatic shape anisotropy, it is worth to study the temperature dependence of the spin-orbit induced MAE by using the metadynamics simulations.

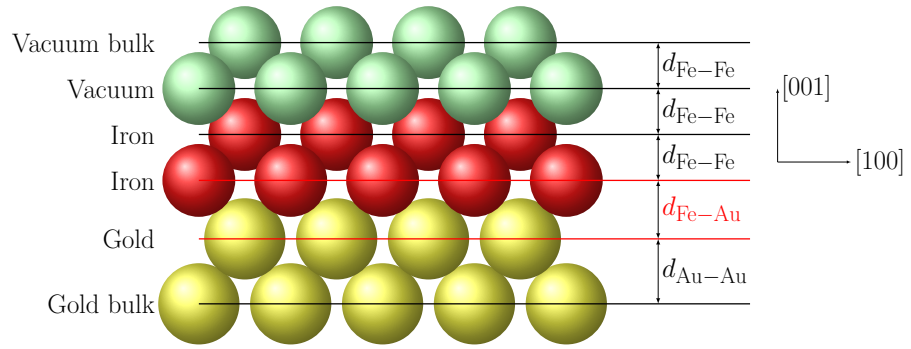

FIGURE 3.14: Interface geometry of $Fe_2/Au(001)$ showing the different interlayer distances. The yellow, red and green spheres denote the gold, the iron and the vacuum sites, respectively. The spheres are proportional to their ASA sizes of the atoms. The bulk label indicates, that from this point the bulk geometry is applied.

3.5.1 $Fe_2/Au(001)$

Geometry and electronic structure

The $Fe_2/Au(001)$ was modeled by four atomic layers of Au, two atomic layers of Fe, and three atomic layers of empty spheres (vacuum) sandwiched between semi-infinite bulk Au and semi-infinite vacuum. Since the (001) surface of fcc Au fits almost perfectly to the (001) surface of the bcc Fe – the lattice mismatch is less than 0.6 % –, a perfect 2D translational symmetry was supposed for the whole system with the lattice constant of Au substrate ($a_{Au} = 2.87$ Å) in all atomic layers, thus the distance of the Au atomic layers was $d_{Au-Au} = 2.03$ Å. The Fe-Fe interlayer distance, the Fe-Vac distance and the Vac-Vac distance above this have been chosen to be the same as the bulk value ($d_{Fe-Fe} = 1.44$ Å). Since the magnetic anisotropy energy is sensitive to the lattice relaxation, the electronic structure was determined for different values of the Fe-Au interlayer distance ranging from d_{Fe-Au} =1.45 Å to 1.7 Å. The geometry of the interface region is presented in Fig. 3.14.

Spin model

The magnetic behaviour of the system was described by the following Heisenberg Hamiltonian:

$$H = -\frac{1}{2}\sum_{p,q=1}^{n}\sum_{i,j}\mathbf{s}_{pi}^{T}\mathbf{J}_{pi,qj}\mathbf{s}_{qj} - \sum_{p=1}^{2}\sum_{i}\lambda_p(\mathbf{s}_{pi}\mathbf{e}_z)^2\,, \tag{3.36}$$

where p and q denote the layers, i and j stand for Fe atoms within each layer, $\mathbf{e}_z$ is a unit vector parallel to the [001] direction, $\mathbf{J}_{ij}$ is a 3×3 matrix of exchange interactions, and λ_p is an on-site uniaxial on-site anisotropy constant at layer p. The detailed description of this model can be read in Sec. 2.2. The $\mathbf{J}_{ij}$ exchange

coupling parameters, and the λ_p on-site anisotropies were determined for all investigated $d_{\mathrm{Fe-Au}}$ distances *ab initio* using the relativistic torque method [42]. The $\mathbf{J}_{ij}$ exchange interaction was limited to the radial distance of $8a_{\mathrm{Au}} = 22.96\,\text{Å}$. The energy difference between the ferromagnetic z and ferromagnetic x configurations, and the layer dependent on-site anisotropies are presented in Tbl. 3.2. The largest anisotropy energy is at the $d_{\mathrm{Fe-Au}} = 1.1\,d_{\mathrm{Fe-Fe}} = 1.584\,\text{Å}$ relaxation, which we used for the further calculations. The spin magnetic moments of the Fe layers – which are also susceptible to interlayer relaxations –, were found to be $\mu_{\mathrm{S}} = 3.0\,\mu_{\mathrm{B}}$ in the surface layer (in direct contact with vacuum), and $\mu_{\mathrm{I}} = 2.7\,\mu_{\mathrm{B}}$ in the interface layer.

TABLE 3.2: Zero temperature total MAE and layer dependent on-site anisotropy constants (in units of meV) in Fe_2/Au(001) for different $d_{\mathrm{Fe-Au}}$ values. The Fe layer at the interface with Au is denoted by I, the one at the surface by S. Negative/positive values of the anisotropies prefer in-plane/normal-to-plane orientation of the magnetization.

$d_{\mathrm{Fe-Au}}/d_{\mathrm{Fe-Fe}}$	λ_{I}	λ_{S}	$E_z - E_x$
1.02	-0.0509	0.4630	-0.2778
1.04	-0.0600	0.4732	-0.4083
1.06	-0.0800	0.4525	-0.5109
1.08	-0.0936	0.4061	-0.6032
1.10	-0.0966	0.3600	-0.6692
1.12	-0.0892	0.3120	-0.6491
1.14	-0.0802	0.2647	-0.6056
1.16	-0.0702	0.2202	-0.5653
1.18	-0.0591	0.1809	-0.5541
1.20	-0.0438	0.1518	-0.5443

In order to characterize the anisotropy of the exchange tensors the lattice sum of the exchange couplings has been introduced:

$$\mathbf{J}_p = \frac{1}{2} \sum_{q=1,2} \sum_j \mathbf{J}_{p0,qj} \ , \tag{3.37}$$

where $\mathbf{J}_{p0,qj}$ is the coupling tensor between an arbitrary site 0 in layer p and site j in the layer q. Due to the C_{4v} symmetry of the lattice $\mathbf{J}_p$ is a diagonal matrix with identical J_p^{xx} and J_p^{yy} elements.

The layer dependent uniaxial on-site anisotropy constants λ_p, and the anisotropy of exchange couplings $J_p^{zz} - J_p^{xx}$ are summarized in Tbl. 3.3. Interestingly, the on-site anisotropies and the exchange anisotropies have different signs in both the interface (I) and the surface (S) layer, and they also change sign between the two layers. Nevertheless, in both layers the positive contributions dominate, resulting in an overall normal-to-plane magnetic ground state for the bilayer.

TABLE 3.3: Calculated layer dependent magnetic anisotropy parameters for the chosen relaxation (in units of meV) for the $Fe_2/Au(001)$ layers. The Fe layer at the interface with Au is denoted by I, the one at the surface by S. Negative/positive values of the anisotropies prefer in-plane/normal-to-plane orientation of the magnetization.

layer	λ	$J_p^{zz} - J_p^{xx}$
I	−0.097	0.181
S	0.360	−0.314

Finite temperature simulations

The thermodynamic quantities of the system such as the magnetization ($M(T)$) and the specific heat ($C(T)$), have been calculated by means of Monte Carlo simulations. The peak of the $C(T)$ curve set the Curie temperature to $T_C = 440\,K$, which is very close to the experimentally reported value of $T_C^{exp} = 430\,K$ [62].

The MAE was calculated by well-tempered metadynamics simulations. The results for $K(T)$ are plotted against the magnetization curve in Fig. 3.15 for the low temperature limit. It is remarkable that the MAE exhibits a $K \propto M^3$ dependence similar to the Callen and Callen theory for $\ell = 2$ [108], though the anisotropy has both on-site and two-site contributions, see Tbl. 3.3. In such cases the temperature dependence of the MAE has no predictable power-law form, for systems with uniaxial anisotropy one can expect an exponent between two and three.

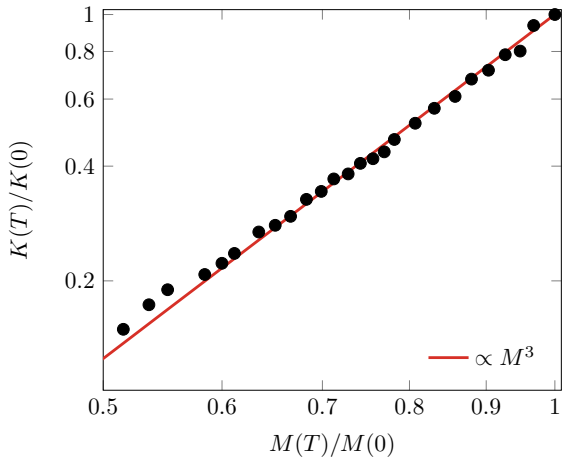

FIGURE 3.15: Temperature dependence of the magnetic anisotropy energy of $Fe_2/Au(001)$ om a log-log mesh. The simulations were performed on a $2 \times 64 \times 64$ lattice with the parameters $T_m = 10\,T_C$, $w_0 = 0.16\,T_C$ and $\sigma = 0.04$.

3.5.2 $Fe_3/Au(001)$

Geometry, electronic structure and spin model

For the trilayer the same geometry was used as for the bilayer (see Fig. 3.14.), the third Fe layer was put in the place of the first vacuum layer in the same vertical position. Similarly the effect of the Fe-Au interlayer distance on the exchange coupling parameters was calculated. We used the same Heisenberg Hamiltonian, the only difference is the extension to the third Fe layer:

$$H = -\frac{1}{2}\sum_{p,q=1}^{n}\sum_{i,j}\mathbf{s}_{pi}^{T}\mathbf{J}_{pi,qj}\mathbf{s}_{qj} - \sum_{p=1}^{3}\sum_{i}\lambda_p(\mathbf{s}_{pi}\mathbf{e}_z)^2\,, \tag{3.38}$$

where the exchange parameters were calculated with the relativistic torque method. The result of the study on interlayer relaxation can be seen in Tbl. 3.4. The on-site anisotropy prefers normal to plane configuration, but it is compensated by the two-site contribution and the MAE prefers an in-plane magnetization, as it is expected from the experiments. The spin magnetic moments of the Fe layers are $3.0\,\mu_B$, $2.3\,\mu_B$ and $3.0\,\mu_B$ in the surface, middle and interface layers, respectively.

TABLE 3.4: Calculated total MAE and sum of the layer-dependent on-site anisotropy constants for $Fe_3/Au(001)$. All energies are given in meV.

d_{Fe-Au}/d_{Fe-Fe}	$E_z - E_x$	$\lambda_S + \lambda_M + \lambda_S$
1.10	0.073	−0.072
1.12	0.088	−0.076
1.14	0.118	−0.086
1.16	0.142	−0.095

Finite temperature simulations

The thermodynamic quantities of the system, such as the magnetization ($M(T)$) and the specific heat ($C(T)$), have been calculated by means of Monte Carlo simulations. The peak of the $C(T)$ curve set the Curie temperature to $T_C = 500\,K$, which is still close to the experimentally reported value of $T_C^{exp} = 550\,K$ [62].

The MAE was calculated by well-tempered metadynamics simulations, using the same relaxed geometry as for $Fe_2/Au(001)$. Here we have to note, that as in the model systems the x and y directions are equivalent in a (001) surface, and cannot be differentiated with a collective variable defined by the out-of-plane component of the magnetization. So in the following we can only state that the magnetization

is in-plane, without further specifying its direction. The metadynamics simulations were performed on a $3 \times 32 \times 32$ lattice. The temperature dependence of the relative free energy magnetic anisotropy with respect to the normal to plane configuration can be seen in Fig. 3.16. As the figure shows, the MAE is in the μRy range. This

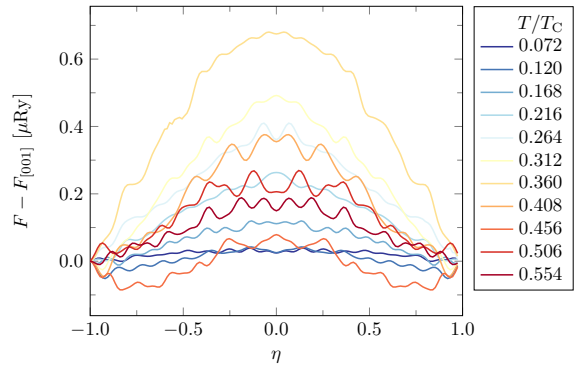

FIGURE 3.16: Temperature dependence of the relative free energy magnetic anisotropy normalized to one spin with respect to the normal to plane configuration in Fe_3/Au(001). The simulations were performed on a $3 \times 32 \times 32$ lattice with the parameters $T_m = 10\,T_C$, $w_0 = 0.16\,T_C$ and $\sigma = 0.04$. The different colors represent different temperatures.

values are so small, that we are in the range of the Gaussian in the metadynamics simulations, which explains the error of the curve. The comparison of the different temperatures shows, that this temperature dependence is not monotonic, both at low temperatures (blueish curves) and high temperatures (reddish curves) it is small, and it has a maximum at $0.36\,T_C$, i. e. 180 K. This can probably be explained similarly to the SRTs of the model system. At low temperatures the term from the on-site anisotopy, which was proven to prefer the normal-to-plane configuration is strong, it nearly compensates the contribution from the two-site anisotropy, thus the MAE is small. Then the former contribution diminishes faster, thus the anisotropy energy grows, until a maximum, where is begins to decrease with the temperature, as expected.

3.6 Fe bilayer on W(110): reorientation and DMI

Ultrathin Fe films epitaxially grown on W(110) have been studied intensively [133, 134] due to their peculiar magnetic properties, such as in- and out-of-plane anisotropy [135], spin reorientation [63, 64], and domain wall formation [136]. The magnetic ground state of the Fe_2/W(110) depends on the size and shape of the double-layer areas in the experiments [64, 137]. Fe double layer (DL) stripes exhibit a periodic magnetic structure with alternating out-of-plane domains separated by 180° walls [138]. For larger DL islands there is a normal-to-plane ferromagnetic order at low temperature [63], which turns into the in-plane direction $[1\bar{1}0]$ at

higher temperature [139]. The quality of the Fe coverage also influences the thermodynamic properties, i. e. according to susceptibility measurements [139] the Curie temperature strongly depends on the Fe coverage.

Geometry and electronic structure

The Fe_2/W(110) interface was modeled by seven atomic layers of W, two atomic layers of Fe, and three atomic layers of empty spheres (vacuum) sandwiched between semi-infinite bulk W and semi-infinite vacuum. The bulk lattice constant of bcc Fe is $a_{\mathrm{Fe}} = 2.867\,\text{Å}$, and of bcc W is $a_{\mathrm{W}} = 3.165\,\text{Å}$. Due to this large lattice mismatch of 9.4 %, there is a considerable inward relaxation of the Fe layers, which has been confirmed by many experimental [134, 140, 141], as well as theoretical [142–144] investigations. In our calculations the distance between the upmost W layer and the interfacial Fe layer was chosen to be $d_{\mathrm{Fe-W}} = 2.01\,\text{Å}$, whereas the distance between the interfacial and surface Fe layers was set to $d_{\mathrm{Fe-Fe}} = 1.71\,\text{Å}$, according to the results of earlier studies based on density functional theory calculations [143, 144]. The layered geometry is presented in Fig. 3.17. The spin magnetic moments of the Fe layers were found to be $\mu_{\mathrm{S}} = 2.78\,\mu_{\mathrm{B}}$ in the surface layer, and $\mu_{\mathrm{I}} = 2.34\,\mu_{\mathrm{B}}$ in the interface layer, and the ferromagnetic alignment of the layers was found to be preferred. The largest induced magnetic moment of $\mu_{\mathrm{W}} = 0.16\,\mu_{\mathrm{B}}$ was found in the upmost W layer, and it was aligned antiparallel to the magnetic Fe layers.

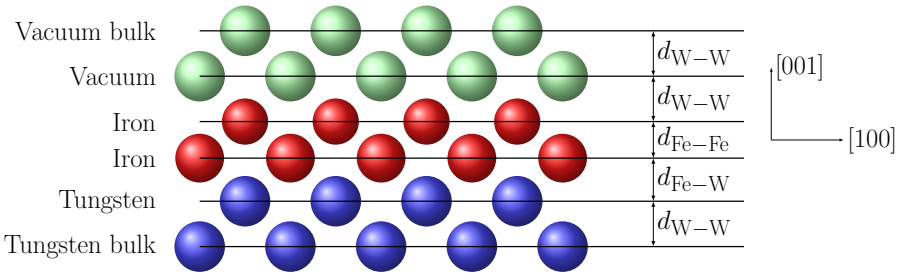

FIGURE 3.17: Interface geometry of Fe_2/W(110) showing the different interlayer distances. The blue, red and green spheres denote the tungsten, the iron and the vacuum sites, respectively. The spheres are proportional to their ASA sizes of the atoms. The bulk label indicates, that from this point the bulk geometry is applied.

Spin model

As opposed to the previous case, the W(110) substrate has a lower – $C_{2\mathrm{v}}$ – symmetry, which implies that the x and y components of the parameters will not be equal, and a bi-axial on-site anisotropy is required. The magnetic Fe DL was modeled by the

following classical Heisenberg spin Hamiltonian:

$$H = -\frac{1}{2}\sum_{p,q=1}^{2}\sum_{i\neq j}\mathbf{s}_{pi}^{T}\mathbf{J}_{pi,qj}\mathbf{s}_{qj} + \sum_{p=1}^{2}\sum_{i}\lambda_{px}(\mathbf{s}_{pi}\hat{\mathbf{x}})^2 + \sum_{p=1}^{2}\sum_{i}\lambda_{py}(\mathbf{s}_{pi}\hat{\mathbf{y}})^2 \,, \quad (3.39)$$

where λ_{px}, and λ_{py} are the on-site biaxial anisotropy constants in layer p, and the $\hat{\mathbf{x}}$ and $\hat{\mathbf{y}}$ vectors are unit vectors parallel to the $[1\bar{1}0]$ and [001] in-plane directions, respectively.

The relativistic torque method was applied by Levente Rózsa to calculate the exchange interaction tensors and the on-site anisotropy coefficients. Due to the (110) surface the calculations were performed in parallel alignments of the spins along two in-plane nearest-neighbour directions, one in-plane next-nearest-neighbour and third-nearest-neighbour direction, and along the out-of-plane directions. The ferromagnetic or antiferromagnetic alignment of the moments in the Fe as well as the substrate layers was based on the self-consistent calculations. Since orienting the moments along a specific direction only gives information about the exchange tensor elements with Cartesian indices perpendicular to the magnetization direction, a least-squares-fitting procedure was applied to the results of the five different calculations mentioned above. The interaction between atoms was included in the model within a real-space cutoff of $8\sqrt{2}a_{\mathrm{W}} = 35.808\,\text{Å}$. The magnetostatic dipolar interaction was added manually to the traceless symmetric part of the exchange tensors, since it is not taken into account in the *ab initio* calculations. The dipolar term favors spin alignment along the [001] direction by 0.143 meV/atom and along the [110] direction by 0.137 meV/atom over the out-of-plane [110] orientation.

TABLE 3.5: Calculated layer dependent magnetic anisotropy parameters (in units of meV) for the Fe_2/W(110) layers. $J_p^{\alpha\alpha}$ is defined in Eq. (3.37). The Fe layer at the interface with W is denoted by I, the one at the surface by S. The notations x, y, and z stand for the $[1\bar{1}0]$, [001], and [110] directions, respectively.

layer	λ_x	λ_y	$J_p^{zz} - J_p^{xx}$	$J_p^{zz} - J_p^{yy}$
I	0.611	0.261	– 0.603	0.138
S	– 0.055	– 0.137	0.377	0.106

The layer-wise on-site and exchange anisotropy parameters defined in Eq. (3.37), are summarized in Tbl. 3.5. The anisotropy of the exchange couplings in the interface layer prefers the in-plane $[1\bar{1}0]$ direction, which is partially compensated by the contribution from the surface layer. On the contrary, the on-site anisotropy of the interface layer clearly prefers the normal-to-plane [110] direction for the magnetization. The MAE calculated as the difference between the energy of the system magnetized in the $[1\bar{1}0]$ in-plane direction and parallel to the normal-to-plane [110]

direction, $E_{1\bar{1}0} - E_{110} = 0.330\,\text{meV}$, as well as the MAE related to the [001] and [110] directions, $E_{001} - E_{110} = 0.368\,\text{meV}$, imply indeed a normal-to-plane magnetic orientation in the ground state as also found in Refs. [136, 142].

Finite temperature simulations

Standard Metropolis Monte Carlo simulations on the perfect DL of Fe resulted in a Curie temperature of $T_\text{C} = 520\,\text{K}$, which is in relatively good agreement with the experimentally reported $T_\text{C}^\text{exp} = 455\,\text{K}$ [139]. In the metadynamics MC simulations the normal-to-plane component of the normalized magnetization was chosen again as the collective variable. The height of the Gaussian bias potentials was set to $w_0 = 0.04\,\text{mRy}$, their width was $\sigma = 0.06$, and the metadynamics temperature was set to $T_\text{m} = 10400\,\text{K}$. The simulations were performed on a $64 \times 64 \times 2$ lattice.

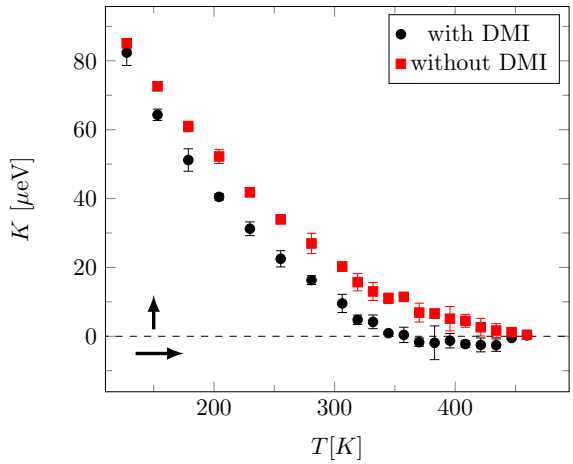

FIGURE 3.18: Temperature-dependent MAE of the DL Fe on W(110) obtained from metadynamics simulations, defined as the difference in the free energy between the normal-to-plane and the in-plane magnetic configurations. The presented values are normalized to one Fe atom. The black solid circles show results based on the full Hamiltonian in Eq. (3.39), while the red squares correspond to a simulation where the DMI was set to zero. An average over 60 Monte Carlo simulations was performed at each temperature, and the error bars denote the standard deviation calculated from these independent simulations. The number of Monte Carlo steps was at least 1.5×10^5 at each temperature, with a higher number of steps close to the phase transitions. The calculations were carried out on a $64 \times 64 \times 2$ lattice, using the metadynamics parameters $T_\text{m} = 10400\,\text{K}$, $w_0 = 0.04\,\text{mRy}$, and $\sigma = 0.06$.

Since the DMI induced anisotropy (see in Sec. 3.3) is expected to be present in this system, two sets of calculations were performed, one with the full set of coupling parameters, and a second where all the DM vectors were omitted by the removal of the antisymmetric part of the coupling tensors $\mathbf{J}_{pi,qj}$. In Fig. 3.18 the magnetic anisotropy energy (K) defined as the difference of the free energy between the [$1\bar{1}0$]

TABLE 3.6: In-plane components of the DM vectors with the largest magnitude in the Fe_2/W(110). The Fe layer at the interface with W is denoted by I, the Fe at the surface by S. The number after N denotes the order of the neighbour. $D^x_{pi,qj} > 0$ prefers a right-handed rotation or fluctuation of the spins in the yz plane ($z \to y$), $D^y_{pi,qj} > 0$ describes an energy gain from a left-handed rotation in the xz plane ($x \to z$), following the convention of Ref. [146]. The z component of the DM vectors is 0 for all pairs in the table.

pair	$D^x_{pi,qj}$ (meV)	$D^y_{pi,qj}$ (meV)
S–S N1	1.62	-1.98
S–I N1	1.69	0.00
I–I N2	1.22	0.00
I–I N4	-1.12	0.34

in-plane orientation and the [110] normal-to-plane orientation is depicted for a wide range below T_C.

First let us focus on the calculation with the full set of parameters (black spheres). As can be inferred from this figure, the MAE changes sign at $T_r = 350\,K$ indicating a SRT from the normal-to-plane ($K > 0$) to in-plane ($K < 0$) direction. The temperature of the SRT is higher than the value reported experimentally in Ref. [137], but is supported by the presence of out-of-plane magnetized DL patches found at room temperature in Ref. [145], demonstrating that T_r strongly depends on the size and shape of the DL areas. Although the metadynamics simulations which use only the out-of-plane magnetization component as a collective parameter do not enable one to differentiate between in-plane directions, calculations based on the standard Metropolis Monte Carlo algorithm confirmed that above T_r the average magnetization is aligned along the x direction, in agreement with the prediction based on Table 3.5. The anisotropy goes to zero around $T \approx 450\,K$, which is slightly below the Curie temperature based on the heat capacity measurements, yet it is in good quantitative agreement with the measurements in Ref. [139]. The driving force of the spin reorientation is most probably a competition between the exchange anisotropy and the on-site anisotropy, since these contributions to the MAE exhibit different temperature dependences, as explained in details for the model systems before. Yet we have to turn our attention to the difference of the two curves (with and witout DMI). As seen for the model system in Sec. 3.3 the curve without the DMI is shifted upwards at all temperatures compared to simulations utilizing the full coupling. Note, that for this case this small shift has a significant effect, since the curve has no crossing through the zero value, consequently, without this dynamic anisotropy term due to the DMI, there is no reorientation of the spin direction.

The components of the largest DM vectors in the DL Fe on W(110) determined from the *ab initio* calculations are listed in Tbl. 3.6. The C_{2v} symmetry of the system causes the in-plane components of the DM vectors to dominate, as expected

for interfacial inversion-symmetry breaking. The z component of the DMI is exactly zero for all pairs in the same magnetic layer, as well as for interlayer pairs located in symmetry planes. Overall, the x component of the DM vectors has the largest contribution, preferring the formation of right-handed Néel-type domain walls with normal vectors along the [001] direction in the out-of-plane magnetized system, in agreement with the experimental observations [146].

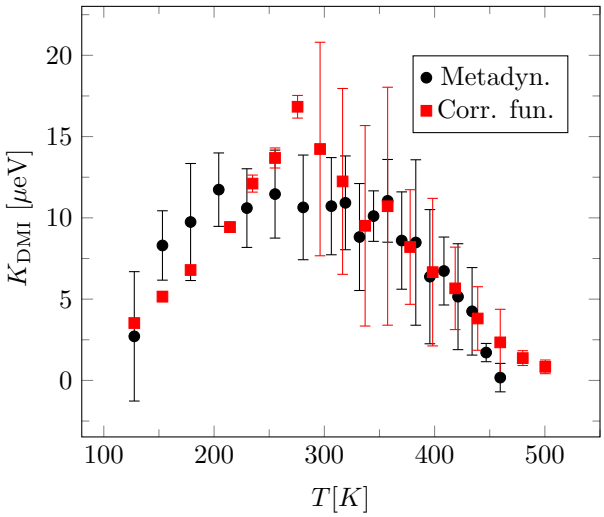

FIGURE 3.19: The difference in the MAE per Fe atom between metadynamics simulations with and without the DMI (black solid circles). The red squares denote the correlation function $\mathrm{K_{DMI}}$ from Eq. (3.7), which attributes this anisotropy to the DMI-induced chiral spin correlations, with the magnetization and the correlation function determined from Metropolis Monte Carlo simulations. Both calculations were performed on a $64 \times 64 \times 2$ lattice. Error bars denote the standard deviation calculated from 60 independent simulations.

The correlation function in Eq. (3.7), and the value for $\mathbf{D}$ in Tbl. 3.6 indicate that at finite temperatures where the spin fluctuations play a prominent role the DMI prefers the magnetization to be aligned in plane along the x direction. To confirm this idea the correlation function and the difference of the two MAE curves from Fig. 3.18 are plotted in Fig. 3.19. The magnetization and the correlation functions necessary for the calculation of K_{DMI} were obtained from standard Metropolis Monte Carlo simulations, with the correlation function determined only for the neighbours with the largest DMI interactions listed in Tbl. 3.6. Figure 3.19 demonstrates that the analytical expression for K_{DMI}, which only takes into account the lowest-order correlation corrections, is in good quantitative agreement with the full scale numerical simulations of the anisotropy contribution attributed to the DMI over the whole temperature range. Importantly, this contribution approaches zero at low temperature, where the fluctuations are suppressed, and it also vanishes close to the Curie temperature where the magnetization disappears, as can be deduced

from Eq. (3.7). The magnitude of the DMI-induced anisotropy is maximal around room temperature in the system, close to the SRT temperature. This behaviour is fundamentally different from the temperature dependence of the on-site MCA and the SA, which monotonically decrease in magnitude from zero temperature, and for which the spin-spin correlations lead to a faster decay compared to the mean-field prediction [147].

Chapter 4

Magnetic skyrmions in ultrathin films

In this Chapter I am going to present the results on the creation and annihilation of skyrmionic structures in skyrmion–hosting systems. First I summarize the basics of skyrmions physics, then I show how well-tempered metadynamics can be used to identify skyrmions and antiskyrmions as quasiparticles, and I present the prerequisites needed to be able to obtain their respective chemical potential. The method is tested in two skyrmion–hosting systems, namely $(Pt_{0.95}Ir_{0.05})$/ Fe/Pd(111) and Pd/Fe/Ir(111) illuminating their different energetics.

4.1 Background

Magnetic skyrmions, analogously to their namesakes in field theory are localized, noncollinear configurations, on a lattice. Since the first indications for the formation of a skyrmion lattice in bulk MnSi via neutron scattering [26, 148, 149] and real-space imaging on $Fe_{0.5}Co_{0.5}Si$ film using Lorentz transmission electron microscopy [150], magnetic skyrmions have been observed in a wide variety of bulk materials and in thin films [34]. Later it was shown, that these whirling magnetic patters can be stabilized by the Dzyaloshinky–Moriya interaction [30], by four-spin interactions [31], or due to the frustration of Heisenberg exchange interactions [32, 33]. Similarly, the magnetostatic dipolar interaction can also create cylindrical magnetic domains, which are called magnetic bubbles. An important difference between magnetic skyrmions and bubbles is that the size of a magnetic bubble is usually in the micrometer range, whereas the magnetic skyrmions are much smaller, generally in the nanometers scale. A more important difference is that in contrast to the bubbles, skyrmions are much more stable objects, in the continuum description a skyrmion cannot be destroyed, and also in lattice models they show an exceptional topological stability. Their special properties, such as their nanoscale size, exceptional stability and considerable mobility, make magnetic skyrmions perfect

candidates for usage in logical and high-density memory devices [36–38], and they form an emerging platform for future neuromorphic and quantum computing [39].

Though skymions have already been found at zero magnetic field [151], the stability of skyrmion state usuallys requires the presence of an external magnetic field, which makes possible the magnetic skyrmions to become energetically the most favourable state [30]. In bulk systems the skyrmions may be present as tubes aligning parallel to the direction of the magnetic field B. In thin films the external field must be perpendicular to the surface so that the skyrmions become energetically favourable. The spin in the middle of the skyrmion must be always directed opposite to the external field. Yet the overall magnetization of the skyrmion is parallel to the field, since there are more spins in the outer shells of the skyrmion, and this makes it energetically preferred due to the Zeeman term. Finally note that with the increase of the magnetic field the skyrmions loose their energetic advantage against the ferromagnetic state, and the skyrmions disintegrate, so the individual skyrmion particles can only be present in a specific field range. Skyrmions can be distinguished based on the type of their respective domain walls, namely there are Néel-type and Bloch-type skyrmions. In the former case the magnetic moments rotate along the radial direction, whereas in the case of Bloch type skyrmions the moments rotate perpendicular to the radial direction. The possible configurations are doubled when the different chiralities are also taken into account. Usually the crystal structure and the broken inversion symmetry at interfaces chooses the favourable configuration in a given case.

The topology of magnetic skyrmions can be characterized by three parameters [34]: their topological charge (Q), their vorticity (ω), and their helicity (ν). In field theory the topological charge is defined as follows [152]:

$$Q = \frac{1}{4\pi} \int \mathrm{d}^2 r \, \mathbf{s} \cdot (\partial_x \mathbf{s} \times \partial_y \mathbf{s}) \ , \tag{4.1}$$

where $\mathbf{s}$ is the classical spin vector with unit length. For the discrete lattice spin models this transforms to the following formula [153]:

$$Q = \sum_{\{i,j,k\}} \frac{1}{2\pi} \arctan \left(\frac{\mathbf{s}_i \cdot (\mathbf{s}_j \times \mathbf{s}_k)}{1 + \mathbf{s}_i \cdot \mathbf{s}_j + \mathbf{s}_i \cdot \mathbf{s}_k + \mathbf{s}_j \cdot \mathbf{s}_k} \right) \ , \tag{4.2}$$

where $\{\mathbf{s}_i, \mathbf{s}_j, \mathbf{s}_k\}$ denotes the spin vectors at three nearest-neighbour sites forming triangles that cover the lattice. In the case of periodic boundary condition the value of Q is always an integer, and with this sign convention in our investigated host systems, the topological charge of an isolated skyrmion in a background pointing along the positive z direction will be $Q = -1$. The vorticity and helicity are linked

to the magnetization field.

$$\mathbf{s}(r,\varphi) = \begin{pmatrix} \sin\theta(r)\cos\phi(\varphi) \\ \sin\theta(r)\sin\phi(\varphi) \\ \cos\theta(r) \end{pmatrix}, \tag{4.3}$$

$$\theta(\varphi) = \omega\varphi + \nu\,, \tag{4.4}$$

where r and φ are the radial distance of $\mathbf{s}$ from the center of the skyrmion, and its relative angle to the x direction. The direction of magnetization at position r, φ are given by the angles θ and ϕ. The vorticity (ω) expresses how many times and in which direction the in-plane component of the spins rotates around the circle when following a closed curve surrounding the center of the skyrmion. It is connected to the topological charge, $Q = \pm\omega$ depending on the direction of B. In realistic surface magnetic systems the Dzyaloshinsky–Moriya interaction prefers a given rotational sense of the spins, which selects a fixed value of helicity for magnetic skyrmions [29, 154].

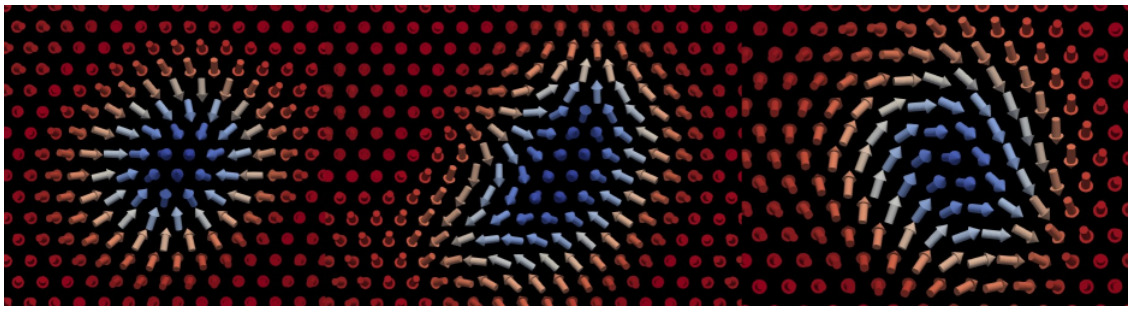

FIGURE 4.1: Examples for Néel type skyrmions with different topological charges. Left: skyrmion ($Q = -1$), middle: antiskyrmion ($Q = 1$) and right: chimera skyrmion ($Q = 0$). In all cases the magnetic field is pointing downwards, allowing only upward pointing skyrmions in the system. The coloring respects the spin direction, upwards and downwards pointing spins are denoted by blue and red, respectively.

The topological charge Q counts how many times the spin configuration winds around the unit sphere upon the application of stereographic projection. This quantity is zero in a ferromagnetic or antiferromagnetic state. However skyrmions always have a finite topological charge. Fig. 4.1 shows examples for a skyrmion (left), an antiskyrmion (middle) and for chimera skyrmion [155] (right), with topological charge $Q = 1$, $Q = -1$ and $Q = 0$ respectively. Note, that the topological charge without the other two parameters does not define uninquely the spin configuration: a value of $Q = 1$ may describe an antiskyrmion with the spins winding oppositely compared to a skyrmion (like on Fig. 4.1), or a skyrmion where all spin directions are reversed compared to the $Q = -1$ case. Also more complex structures can have larger topological charge, e. g $Q = -2$ may indicate a composite object but it can

hide also two individual skyrmions. And finally, a finite topological charge does not necessarily mean a localized object, since an elongated segment of a spin–spiral can be described by the same topological charge as a skyrmion. On the other hand localized objects with zero net topological charge may also be stable [29]. Among all of this zoo of objects the skyrmions and antiskyrmions are considered to be the most stable ones. In a continuum model the topological charge cannot be changed dynamically, hence they are called topologically protected, yet in a crystal lattice model it is not perfectly preserved. The finite energy gap between the skyrmion and the topologically trivial states allows to create and annihilate skyrmions, which thus can be regarded as quasiparticles [35]. Energetically, skyrmions are always preferred compared to antiskyrmions, since they gain energy from the DM interactions, while the energy contribution from the isotropic Heisenberg coupling and the Zeeman term is the same for both of them [156]. Considering all the processes listed before, the same change in the topological charge of a lattice can correspond to different physical processes with different energies. Even if only skymions and antiskymions are considered the related energy difference can differ, depending whether a skyrmion is created or an antiskyrmion is destroyed in the process. This means that if we want to calculate these energies, we have to be sure which process is changing the topological charge.

The energy barriers and the attempt frequencies of skyrmion creation and annihilation have been thoroughly investigated based on the zero-temperature energy landscape [33, 157–160], with the results in a good agreement with the collapse mechanisms observed with low-temperature STM [161]. Skyrmion lifetimes have also been calculated based on Metropolis Monte Carlo [162] and atomistic spin dynamics [70] simulations, which are primarily applicable at higher temperatures where the creation and annihilation processes are faster. Deviations from the method based on the zero-temperature energy landscape have been observed in this elevated temperature range [35]. The connection of the low and high T limits is an important task, and it can be achieved by using specialized algorithms to speed up the numerical simulations. A path–sampling approach was applied for this purpose in Ref. [163], and the finite-temperature free energy barriers of single skyrmions were also recently investigated in Ref. [87] using the well-tempered metadynamics. Most of these studies focus on the stability of single isolated skyrmions. Experimental observations in Ref. [164] indicated that at elevated temperatures multiple skyrmions may be created or annihilated at varying positions in nanoislands. It is expected that the interactions between skyrmions as quasiparticles in such ensembles influence their stability, as the influence of interactions has already been demonstrated on the thermally induced motion of skyrmions [165–167]. In my work the goal is to investigate

multi-skyrmion system, and so determine the equilibrium number of skyrmions as a function of the temperature, and to obtain the temperature dependent chemical potential of skyrmions and antiskyrmions.

4.2 Peculiarities in metadynamics to investigate skyrmions

We used metadynamics to explore the free energy surface of skyrmion–hosting ultrathin film systems. Since each skyrmion gives -1 to the topological charge of the lattice, Q is a natural choice for the collective variable. As opposed to the magnetization in the previous chapter, there is no natural limit that bounds the magnitude of the topological charge on a lattice other than its spatial extension which limits the number of objects due to their size. In a recent work [87] the problem of unwanted high Q value was solved by applying a harmonic spring potential outside of the region of interest. Our work focused on the investigation of many skyrmions and such an approach was not used, and we let the walkers explore the whole Q range, though this idea is worth considering to increase the speed of lower temperature simulations. For numerical reasons we chose $\eta = Q/Q_{\mathrm{max}}$ for the CV, which made the interpolation of the Gaussian potentials more manageable. The value Q_{max} was set based on the lattice size, usually $Q_{\mathrm{max}} = 50$ for a 128×128 lattice. This ensured enough space in η to obtain a wide regime of the bias potential, while its resolution remains still acceptable. Since as opposed to the case of MAE, there is no discontinuity at the boundaries the time development of the bias potential in (3.9) takes a simpler form:

$$V_{\mathrm{bias}}(\eta, t+\tau) \quad = \quad V_{\mathrm{bias}}(\eta, t) + V_{\mathrm{G}}(\eta - \eta_{\mathrm{act}})\,. \tag{4.5}$$

Numerical challenges of these simulations are due to the well-known high stability of the skyrmions. At low temperature the skyrmions in the lattice freeze in and it takes extremely long simulation time to overcome the energy barrier between the skyrmion and the ferromagnetic or spin–spiral state. In order to avoid this problem on one hand we applied multiples walkers which covers different regions of the CV η, on the other hand we also increased T_{m} temperature of the well tempered metadynamics. This way we were able to go just below the ordering temperature of the spin–spiral (SS) or skyrmion–lattice (SkL) phases.

At a given temperature, the position of the maximum of $V_{\mathrm{b}}(\eta)$ gives the most likely value Q_0 of the topological charge in the lattice. The average value of the

topological charge $\langle Q \rangle$ can be calculated as

$$\langle Q \rangle = \frac{\sum_{Q'} Q' \exp\{\beta V_\mathrm{b}(Q')\}}{\sum_{Q'} \exp\{\beta V_\mathrm{b}(Q')\}}, \tag{4.6}$$

where $\beta = 1/(k_\mathrm{B}T)$ is the inverse temperature, and the free energy F is replaced by the bias potential $-V_\mathrm{b}$ (see Eq. (2.63)).

4.3 Free energy curves and chemical potentials

As already explained, unfortunately the topological charge does not agree with the number of localized non-collinear spin configurations, such as skyrmions in the lattice. Since the definition of chemical potential is the free energy difference of the system with N and $N+1$ particles in it, it is a necessity to somehow identify how many objects are there even if it cannot be controlled in the metadynamics simulations. A possible solution to this is to look at the snapshots of the real-space spin configurations taken from the simulations. In Fig. 4.2 the snapshots of Fe sites are displayed for $Q = 4$, $Q = 7$ and $Q = -5$ at $T = 61\,\mathrm{K}$ in$(\mathrm{Pt}_{0.95}\mathrm{Ir}_{0.05})/\mathrm{Fe}/\mathrm{Pd}(111)$ at $B = 1\,\mathrm{T}$. At this temperature the thermal fluctuations make the identification of topological objects cumbersome, so the snapshot spin configuration was relaxed at zero temperature using the conjugate gradient method (See Sec. 2.4). It has to be noted, that such a procedure can modify the topological charge of the system by removing high-energy metastable skyrmionic textures, but in the case of low-temperature simulations we found that the topological charge was not affected. The coloring respects the local topological charge density, defined similarly to Eq. (4.2) as the following:

$$q(\mathbf{S}_i) = \sum_{\{j,k\}} \frac{1}{2\pi} \arctan\left(\frac{\mathbf{S}_i \cdot (\mathbf{S}_j \times \mathbf{S}_k)}{1 + \mathbf{S}_i \cdot \mathbf{S}_j + \mathbf{S}_i \cdot \mathbf{S}_k + \mathbf{S}_j \cdot \mathbf{S}_k} \right). \tag{4.7}$$

Three types of objects were found: skyrmions with $Q = -1$, antiskyrmions with $Q = 1$ and chimera skyrmions with $Q = 0$ enclosed in blue, red and green lines in the figures, respectively. Composite objects with higher topological charge are not found, and at this external magnetic field, non-local objects with final topological charge such as elongated spirals are not present. An important fact is that in configuration with positive (Fig. 4.2(a) and (b)) and negative (Fig. 4.2(c)) net topological charges the configuration consist mainly of $|Q|$ antiskyrmions and skyrmions, respectively. This suggests that in the positive and negative Q regions the process behind the change of the topological charge is the creation/annihilation of an antiskyrmion

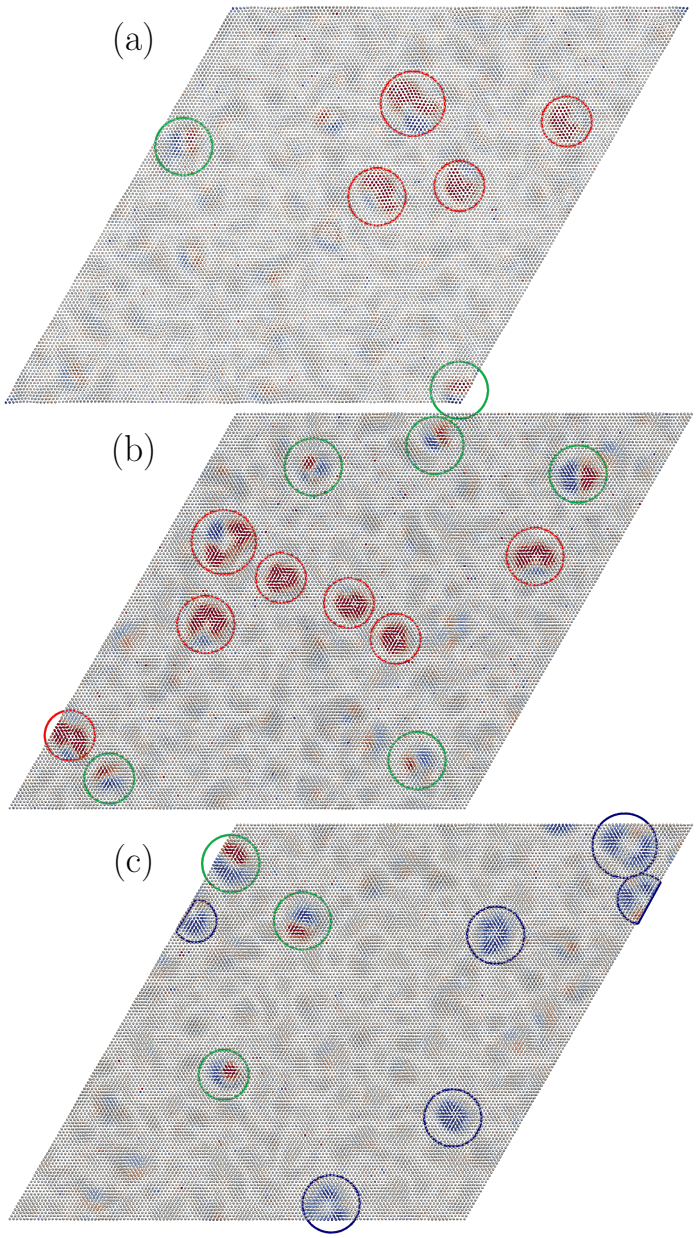

FIGURE 4.2: Snapshots of spin configurations obtained in $(Pt_{0.95}Ir_{0.05})/Fe/Pd(111)$ at external magnetic field $B = 1\,T$, temperature $T = 61\,K$, with topological charges (a) $Q = 4$, (b) $Q = 7$, and (c) $Q = -5$. The configurations were relaxed to turning off the thermal fluctuations for better visualization of the localized spin structures; The coloring denotes the topological charge density: red $q > 0$, blue $q < 0$. Skyrmionic objects with topological charge $Q = 1$, $Q = 0$, and $Q = -1$ are denoted by solid red, green and blue circles, respectively.

and a skyrmion, respectively. By definition in a mixed system with multiple types of particles the chemical potential is the free energy difference of the system with N and $N + 1$ particles in it, while the number of every other particle is fixed. Though chimera skyrmions with $Q = 0$ can also be observed in all configurations, which

complicate the evaluation of the data, but at this low density of localized objects their effect is expected to be small on the free energy differences. So we defined chemical potential of the skyrmions and antiskyrmions as a slope of fitted linears as follows:

$$\mu_{\pm} = \lim_{\Delta Q \to \pm 1} \frac{F(\Delta Q) - F(0)}{|\Delta Q|}\,, \tag{4.8}$$

where the $\pm$ indices denote antiskymions and skyrmions, respectively. This definition assumes, that skyrmion–skyrmion interactions are negligible, which restricts it to a finite region around $Q = 0$. It should be noted, that this definition is based on skyrmion creation and annihilation events in a spatially homogeneous system. A different definition of the skyrmion chemical potential was introduced in Ref. [168], which is spatially inhomogeneous and leads to the accumulation of skyrmions in certain areas while their total number is conserved.

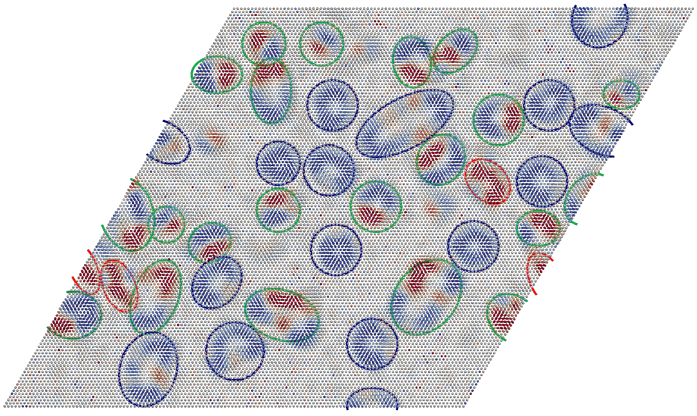

FIGURE 4.3: Spin configuration obtained in $(Pt_{0.95}Ir_{0.05})/Fe/Pd(111)$ at external magnetic field $B = 1\,\mathrm{T}$, temperature $T = 94\,\mathrm{K}$, with topological charge $Q = -11$. The configurations were relaxed to turning off the thermal fluctuations for better visualization of the localized spin structures; The coloring denotes the topological charge density: red $q > 0$, blue $q < 0$. Skyrmionic objects with topological charge $Q = 1$, $Q = 0$, and $Q = -1$ are enclosed by solid red, green and blue lines, respectively.

At higher temperatures the snapshots are more complicated. For the temperature $T = 94\,\mathrm{K}$, a spin configurations after zero temperature relaxation is presented in Fig. 4.3 with $Q = -11$, demonstrating that the topological charge is mostly formed by skyrmions with $Q = -1$, but many other irregularly shaped skyrmion-like patterns with $Q = 0$, and also antiskyrmions with $Q = 1$ are present in the system. Altogether these magnetic textures are much denser than at low T, which means that even with a small overall Q for the whole lattice the skyrmion–skyrmion

interactions play a crucial role, and an independent particle picture does not apply, and the chemical potential of individual objects cannot be evaluated.

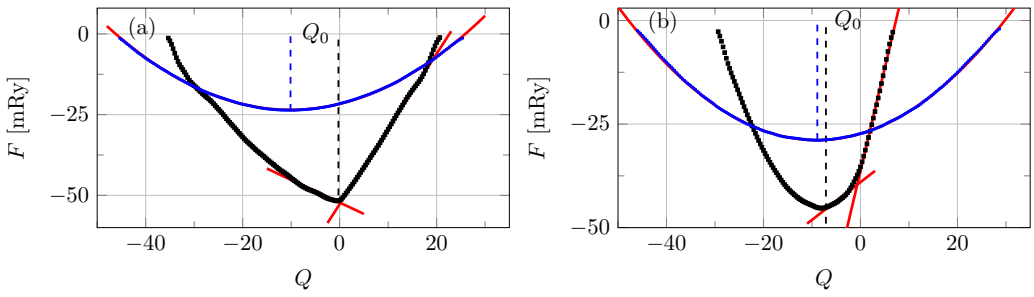

FIGURE 4.4: Free energy curves as a function of the topological charge Q simulated on a 128×128 lattice of Fe sites in $(Pt_{0.95}Ir_{0.05})$/Fe/Pd(111) (left) at T=61 K (black) and T=94 K (blue) in the presence of an external magnetic field $B = 1$ T, and Fe sites in Pd/Fe/Ir(111) (right) at T=141 K (black) and T=243 K (blue) in the presence of an external magnetic field $B = 4$ T. The red curves are obtained by fitting the data to to Eq. (4.9) for high temperature and to Eq. (4.8) for low temperature example. The vertical dashed lines mark the values of Q_0 from the fitting procedures.

This work concentrates on two skyrmion–hosting systems, namely $(Pt_{0.95}Ir_{0.05})$/Fe/Pd(111) and Pd/Fe/Ir(111). A typical low and high temperature example for the free energy curves is shown in Fig. 4.4 for both systems. The temperatures used for $(Pt_{0.95}Ir_{0.05})$/Fe/Pd(111) on Fig. 4.4(a) correspond to the ones of the snapshots in Fig. 4.2. The curves corresponding to $T = 61$ K (black) and to $T = 94$ K (blue) are significantly different.

At low temperature we found an asymmetrical shape with almost linear regions around its minimum Q_0, very close to zero. This behaviour clearly agrees with the assumption of non-interacting, free skyrmionic objects, and the chemical potential can be defined. The linearity of $F(Q)$ in the $Q < 0$ region persists until $Q \approx -10$ and in the $Q > 0$ region persists until $Q \approx 12$. When the number of objects exceeds this, the energy contribution from the skyrmion-skyrmion interactions clearly distorts the curve, as a sign that the free particle picture is only valid up to this point. The relations $\mu_+ > \mu_- > 0$ implies that at $B = 1$ T external field and $T = 61$ K temperature both the skyrmions and antiskyrmions are metastable in $(Pt_{0.95}Ir_{0.05})$/Fe/Pd(111), in agreement with the results in Ref. [35].

Later we will see, that as the temperature grows the linear region becomes smaller and smaller. First this makes the precise definition of the linear region cumbersome thus increases the fitting error, and after a point it is impossible to obtain the chemical potential from Eq. (4.8). At high temperatures such as the blue curves in Fig. 4.4, a parabolic fitting describes well the free energy curve over the whole

range of Q:

$$F(Q) = F_0 + a \cdot (Q - Q_0)^2 \,, \tag{4.9}$$

where F_0, Q_0 and a are fitting parameters and Q_0 defines the most likely value of the topological charge. In such a mixed and dense state as in 4.3 the change of F cannot be associated with the creation or annihilation cost of one type of skyrmionic object.

Figure 4.4(b) shows the free energy curves for the Pd/Fe/Ir(111) system at $T = 141\,\mathrm{K}$ (black) and $T = 243\,\mathrm{K}$ (blue) in the presence of an external magnetic field of $B = 4\,T$, at which field value the ground state is known to be field polarized [70]. The high temperature (blue) curve is very similar to that of the other bilayer system, showing a parabolic dependence on the topological charge with a value of $Q_0 \approx -9$. The low temperature curve is less asymmetric than the one for the $(Pt_{0.95}Ir_{0.05})$/Fe/Pd(111) system and has a minimum at a Q_0 further from the zero net topological case. Similarly, linear fits were performed above and below $Q = 0$. Note that there is a kink in the curve around $Q = 0$, which suggests that the chemical potential for skyrmion ($Q < 0$ side) and antiskyrmions ($Q > 0$ side) differ. Now that both fitting lines are on the same side of the Q_0, following the definition in Eq. (4.8), we obtain different signs for the chemical potential, namely $\mu_+ > 0$ and $\mu_- < 0$. This means that lowering the topological charge, i. e., creating a skyrmion, decreases the free energy of the system. In the same temperature and field regime, a high number of skyrmions was found in equilibrium in Ref. [70], in agreement with this conclusion and the negative value of Q_0 at the minimum of the free energy curve. The relation $|\mu_+| > |\mu_-|$ indicates that the free energy cost of creating an antiskyrmion is larger than the free energy gain of creating a skyrmion. Stable antiskyrmions have not been observed at zero temperature in this system in Ref. [70], which correlates with the observation that short-lived antiskyrmions created by thermal fluctuations have a high free energy cost. As we will see later, when decreasing the temperature $|Q_0|$ also decreases, and at a certain temperature $\mu_-(T)$ changes sign, indicating a field-polarized ground state at lower temperature.

4.4 $(Pt_{0.95}Ir_{0.05})$/Fe/Pd(111)

Fe monolayer on Pd(111) with a $Pt_{1-x}Ir_x$ alloy overlayer has a ferromagnetic ground state for $x = 0$, and it becomes a spin spiral as Ir is intermixed. A study [169] of individual skyrmions depending on the mixing parameter x demonstrated that skyrmions can be stabilized in this system. The most researched case is the $x = 0.05$

alloy. The interplay between frustrated Heisenberg exchange and DMI can lead to the formation of metastable skyrmionic spin structures with various topological charges [170], and skyrmions with $Q = -1$ are found to be the lowest-energy configurations [155].

The ground state configurations of $(Pt_{0.95}Ir_{0.05})/Fe/Pd(111)$ was investigated by Schick *et. al.* [35] as a function of the external magnetic field B. Below $B_1 \approx 0.21\,\mathrm{T}$ a spin–spiral state was found with the lowest energy, and above B_1 it turns to a field-polarized state. The skyrmion lattice phase is not a ground state for any range of external field, but it has a positive energy compared to the field-polarized state above $B_2 \approx 0.1\,\mathrm{T}$. This work also reported about the thermodynamic properties of the system above B_2. They performed atomistic spin model simulations on a relatively small lattice of 25×25 sites, with an aim to host a single skyrmion. The simulations were carried out ranging from low temperatures, where the number of skyrmions is conserved up to the range, where skyrmions are constantly created and destroyed by thermal fluctuations. Based on the time averaging of the number of skyrmions they published a curve on the temperature dependence of $\langle Q \rangle$ at $B = 1\,\mathrm{T}$ external field.

Spin model

In our study the magnetic structure of the system was modeled by the following classical Heisenberg model:

$$H = -\frac{1}{2}\sum_{i \neq j} \mathbf{s}_i^T \mathbf{J}_{ij} \mathbf{s}_j + \sum_i \lambda_z (\mathbf{s}_i \hat{\mathbf{z}})^2 - \mu \sum_i \mathbf{s}_i \mathbf{B}\,, \tag{4.10}$$

where the sums run through the Fe sites, $\mathbf{J}_{ij}$ is the tensorial exchange, λ_z is an on-site uniaxial anisotropy, $\hat{\mathbf{z}}$ denotes a unit vector parallel to the [111] normal direction of the surface, and finally $\mathbf{B} = B\hat{\mathbf{z}}$ is the external magnetic field perpendicular to surface. The geometric structure and the exchange parameters were taken from Ref. [169]. The parameters were obtained using the relativistic torque method and they confirmed the spin–spiral ground state for the system.

Finite temperature simulations

The first, preliminary calculations were performed on a 128×128 lattice in terms of traditional Metropolis MC simulations. The heat capacity (C) presented in Fig. 4.5(a) predicts the critical temperature around 130 K, which was found to be constant in the range of $B = 0.03 - 1\,\mathrm{T}$. The magnetic susceptibility (χ) is presented in Fig. 4.5(b). This quantity shows a peak at lower temperatures, and it

highly depends on the value of external magnetic field B. In contrast to a second-order phase transition, the difference between the maxima of the heat capacity and magnetic susceptibility curves cannot be attributed exclusively to finite-size effects. The heat capacity is maximal where short-range order is completely lost in the system and localized objects may no longer be identified, where the rapidly changing angles between neighbouring spins give rise to high energy fluctuations. On the other hand the susceptibility depends on the fluctuation of the magnetization. In a state where skyrmions and antiskyrmions are created and destroyed very rapidly by the temperature, the susceptibility takes a large value, whereas the heat capacity is still moderate due to the short-range order. As it was seen in Ref. [35], the energy difference between field polarized and skyrmion states depends on the external magnetic field, this explains why the position of the peak is so sensitive to the value of B. Note that similarly to the magnetic susceptibility (χ) one can define a skyrmion susceptibility based on the topological charge:

$$\chi_Q \propto \frac{\langle Q^2 \rangle - \langle Q \rangle^2}{T} . \tag{4.11}$$

The maximum of this quantity has the same position as χ has, since it is based on the fluctuation of the number of skyrmions and antiskyrmions. At low temperatures this suddenly becomes zero as the skyrmionic objects freeze in the lattice.

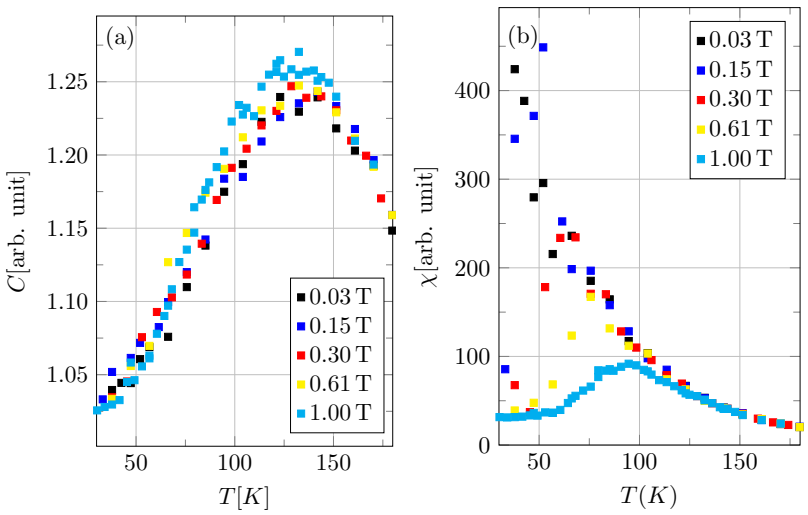

FIGURE 4.5: (a) Heat capacity (C) and (b) magnetic spin susceptibility (χ) simulated on a 128×128 lattice of $(Pt_{0.95}Ir_{0.05})$/Fe/Pd(111) with external magnetic field $B = 0.03 - 1\,\mathrm{T}$.

Next I investigated the topological charge of the system by using our metadynamics Monte Carlo method. From this point the external field was chosen $B = 1\,\mathrm{T}$ similarly to Ref. [35]. The temperature range of the metadynamics simulations was set between 50 K and 160 K. Below $T = 48\,\mathrm{K}$ the number of skyrmions did not

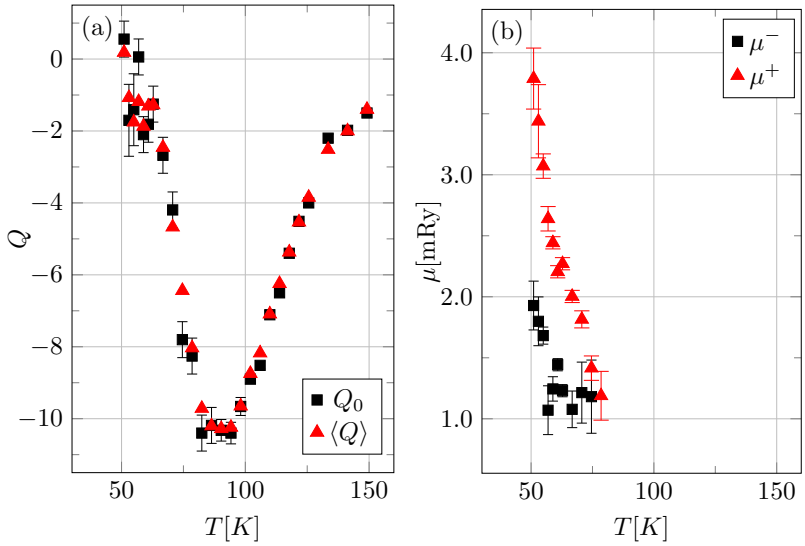

FIGURE 4.6: Average ($\langle Q \rangle$) and most likely (Q_0) topological charge, and chemical potential of skyrmions (μ_-) and antiskymions (μ_+) simulated on a 128×128 lattice of $(Pt_{0.95}Ir_{0.05})/Fe/Pd(111)$ with external magnetic field $B = 1\,\mathrm{T}$ in the same temperature range. The error bars are due to the insufficient statistics of the simulations.

change even for extremely long simulation times, and the free energy curve could not be calculated. Figure 4.6(a) implies, that the average number of skyrmions $\langle Q \rangle$ (Eq. (4.6)) and its equilibrium value Q_0 based on the minimum of the $F(Q)$ curve coincide well with each other. The shape of the $Q(T)$ curves is similar to the one reported in Ref. [35], but the minimum of the curve is set to a higher temperature around 90 K, instead of 75 K in Ref. [35]. Apparently, the topological charge (Fig. 4.6(a)) and the magnetic susceptibility (Fig. 4.5(b)) have their extrema at around the same temperature. Obviously, there is a proportionality between the number of skyrmions and the size of the lattice. Simulations of the same system using smaller (64×64) and larger (256×256) lattices showed that the topological charge scales with the area of the lattice. Considering this scaling, this result is in good agreement with Ref. [35].

Fig. 4.6(b) shows chemical potentials of skyrmions and antiskyrmions as defined in Eq. (4.8). As explained before, this quantity was only measureable at low temperatures, where we can assumed that only one type of topological objects, i. e. only skyrmions or only antiskyrmions are created in the process, while the number of all other topological textures is unchanged, preferably zero. This condition narrowed down the temperature range between 50 K and 80 K. Above 75–80 K the parabolic behavior illustrated in Fig. 4.4 becomes more pronounced in the $F(Q)$ curves. Note that the upper boundary of this temperature range coincides with the point, where Q_0 reaches its maximal value. As for the value of the chemical potential itself, it is

clear, that in the whole temperature range, μ_+ is larger than μ_-, i. e., the cost of creating an antiskyrmion is higher than that of creating a skyrmion.

4.5 Pd/Fe/Ir(111)

This section focuses on another skyrmion–hosting bilayer, namely Pd/Fe bilayer on Ir(111) [27, 70, 171, 172]. In this material, Dzyaloshinky–Moriya interactions competing with isotropic Heisenberg exchange, uniaxial anisotropy and Zeeman terms lead to the formation of metastable isolated skyrmionic spin structures. Spin-polarized scanning tunneling microscopy experiments [27] revealed that the ground state of the system is a spin–spiral state. In the presence of small external magnetic field perpendicular to the surface spin–spirals and Néel-type skyrmions can coexist. The increase of the external field above 1 T leads to the disappearance of the spin–spirals (SS), and to the emergence of a pure hexagonal skyrmion lattice (SkL). Further increase of the magnetic field brings the system into a field-polarized (FP) phase. The experimental results have been reproduced by Monte Carlo simulations based on parameters obtained from first-principles density-functional theory calculations [70, 172, 173].

Spin model

The magnetic structure was modeled by the same Heisenberg spin Hamiltonian as for the previous system:

$$H = -\frac{1}{2}\sum_{i\neq j} \mathbf{s}_i^T \mathbf{J}_{ij} \mathbf{s}_j + \sum_i \lambda_z (\mathbf{s}_i \hat{\mathbf{z}})^2 - \mu \sum_i \mathbf{s}_i \mathbf{B} \,, \tag{4.12}$$

where the sums also run similarly through the Fe sites, $\mathbf{J}_{ij}$ is the tensorial exchange, λ_z is an on-site uniaxial anisotropy, $\hat{\mathbf{z}}$ denotes a unit vector parallel to the [111] normal direction of the surface, and finally $\mathbf{B} = B\hat{\mathbf{z}}$ is the external magnetic field perpendicular to to surface.

The geometric structure and the exchange parameters were taken from Ref. [174]. The parameters were obtained using the spin–cluster expansion technique and they confirmed the spin–spiral ground state for the system.

Finite temperature simulations

Previous spin dynamics [70] and MC simulations [172] distinguished three different ground states depending on the magnitude of the external magnetic field B: spin–spiral (SS) ground state below $B = 1.4\,\mathrm{T}$, skyrmion lattice (SkL) between about

$B = 1.4\,\mathrm{T}$ and $B = 3\,\mathrm{T}$, and field-polarized (FP) state above $B = 3\,\mathrm{T}$. These phases are stable up to 100 K, where the system turns into a fluctuation-disordered regime, which undergoes an order–disorder (paramagnetic) phase transition at about 250 K independently of the external magnetic field. This enhanced complexity of ground state configurations makes Pd/Fe/Ir(111) bilayer a more interesting object of study.

As for the $(Pt_{0.95}Ir_{0.05})$/Fe/Pd(111) bilayer the first step was to calculate thermodynamic quantities, such as heat capacity and magnetic susceptibility via Metropolis Monte Carlo simulations. For the studies we choose a B value corresponding to each possible ground state configuration observed in this system [70]: $B = 0.67\,\mathrm{T}$ with a SS ground state, $B = 1.51\,\mathrm{T}$ with a SkL ground state, and $B = 4\,\mathrm{T}$, where the system is expected to have a FP ground state. Fig. 4.7(a) shows the heat capacity of the system calculated on a 128×128 lattice. Its peak is around $240 - 255\,\mathrm{K}$ depending on the magnitude of the external field, which is in good agreement with the previous studies [70, 172]. Note that in Ref. [70] the same parameters were used, whereas the results in Ref. [172] were based on a differently parameterized spin model. Based on this result, we set the upper limit of the metadynamics simulations to 370 K. Fig. 4.7(b) presents the magnetic susceptibility curves. Similarly, the peak is also at lower temperatures at around 140 K, which can be explained in a similar way.

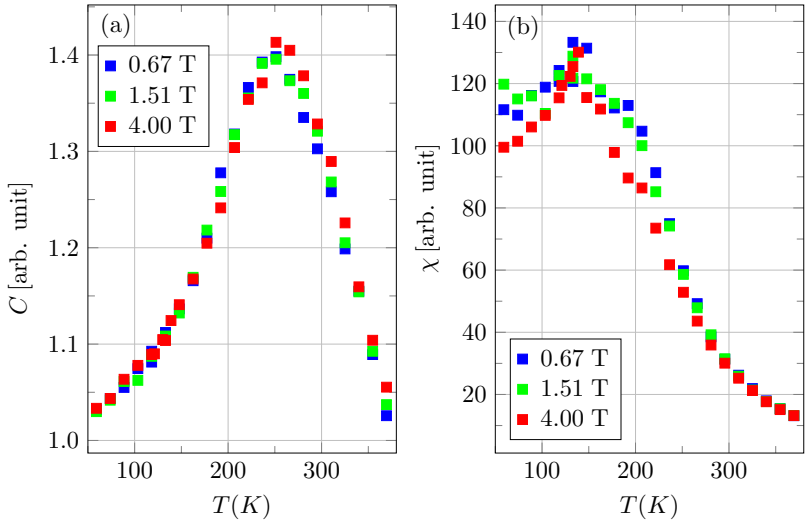

FIGURE 4.7: Temperature dependence of (a) heat capacity (C) and (b) magnetic spin susceptibility (χ) simulated on a 128×128 lattice of Pd/Fe/Ir(111) with external magnetic fields $B = 0.67 - 4\,\mathrm{T}$.

As can be seen in Fig. 4.6(a) the average number and the most likely value of the topological charge coincide very well, so for the sake of simplicity only the latter is presented for this system in Fig. 4.8(a) for the three chosen values of external

magnetic field B. All three curves show maximal absolute Q_0 in an intermediate temperature range between 100 K and 200 K. This indicates that similarly to the previous host system, the formation of skyrmions becomes energetically more favorable as the temperature is increased. This temperature dependence is in good agreement with the results of Metropolis MC simulation in Ref. [70].

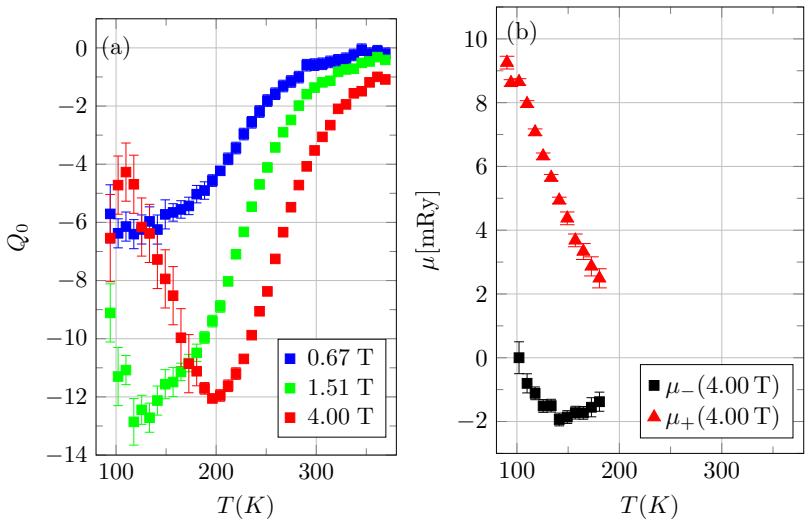

FIGURE 4.8: (a) Temperature dependence of the most likely value of the topological charge (Q_0) simulated on a 128×128 lattice of Pd/Fe/Ir(111) surface in the presence of different external magnetic fields, 0.67 T, 1.51 T and 4.00 T. (b) Temperature dependence of the chemical potential of skyrmions (μ_-) and antiskyrmions (μ_+) on a 128×128 lattice of Pd/Fe/Ir(111) surface with external magnetic field $B = 4.00$ T. The error bars display the uncertainty of the fitting parameters.

The case of FP ground state ($B = 4$ T) is the most similar to the previous system. The corresponding spin configurations indicated that at low temperatures the topological charge exclusively corresponds to skyrmions with $Q = -1$. At higher temperatures other minority skyrmionic textures appear such as antiskyrmions ($Q = 1$) and chimera skyrmions ($Q = 0$). As the temperature steps over the value set by the maximum of the heat capacity curve, the short-range order vanishes, and the topological charge, which approaches the zero value no more describes skyrmion like spin structures.

The other two cases describe a bit different situation. For $B = 1.51$ T, the $Q_0(T)$ curve reaches a similar maximal value around $Q_0 = -13$, but already at a lower temperature (≈ 120 K) and the decrease of $|Q_0|$ is less pronounced. This is not surprising, since the ground state is expected to be a skyrmion lattice. The third curve, belonging to the $B = 0.67$ T has a smaller maximum at a smaller temperature close to the lower limit of our calculations. Theoretically the topological charge should vanish in the zero-temperature limit, because of the spin–spiral ground state

in this case. Note that the spin configurations at these two cases of external magnetic field resemble space-filling networks of domain walls in the low-temperature regime. Individual skyrmions are not stable at zero temperature at these low field values, instead they fill up the whole space due to their strip-out instability. This means that instead of the localized spin textures the topological charge is originated to the ends of the intertwined spin–spiral segments. A very important consequence is that due to the strong interaction between these elongated objects, the free particle picture underlying the definion of the chemical potential in Eq. (4.8) is no longer valid, and the free energy curves are parabolic. Therefore, as presented in Fig. 4.8(b) the chemical potentials were only calculated for $B = 4.00\,\mathrm{T}$. The linear fitting around $Q = 0$ was possible up to the temperature where the most likely value of the topological charge has its minimum at about 180 K. As expected from the example in Fig. 4.4(b), the free energy cost for the creation of antiskyrmions μ_+ is positive, while that of the skyrmions μ_- is negative. This implies that in this temperature region the formation of skyrmions with $Q = -1$ is energetically favorable, whereas the formation of antiskyrmions with $Q = 1$ is highly unfavorable. As Q_0 approaches to zero at lower temperature, the linear regime for $Q < 0$ shrinks. This makes the determination of μ_- difficult based on the fitting procedure, when the slope is close to zero. This is the explanation, why μ_+ could be determined for a bit larger temperature range below 100 K, than μ_- where the length of the fitting interval was approaching zero. It is expected that the chemical potential changes sign in this regime, leading to the field-polarized ground state at zero temperature.

Chapter 5

Ground state magnetism of nanoclusters

In this Chapter results on magnetic ground state configurations of atomic chains deposited on nonmagnetic substrates are presented.

Atomic clusters are the youngest topic in the *ab initio* electronic structure calculations of solid state systems. Since freestanding chains are hardly accessible experimentally, most interests are focused on deposited clusters. The substrate largely influences the electronic structure of cluster atoms and these calculations require the precise knowledge of the electronic structure of the host system before one could even work with the cluster itself. The embedding scheme (see Sec. 2.1.4) relies on the fact, that the electronic structure of the hosting substrate is known, and it is only changed in the small vicinity of the cluster, which can be calculated site by site to gain accurate description of the system. Once the electronic structure of a simple – in most of the case ferromagnetic – magnetic configuration has been determined there are two ways of obtaining complex magnetic ground state configurations. One can fit the exchange couplings and anisotropy parameters to an appropriate spin model and perform Monte Carlo or spindynamics simulations to find non-trivial magnetic ground state. The obtained magnetic configuration is highly sensitive to the underlying spin model. Introduction of higher order spin interactions, e. g. may considerably change the ground state. In order to avoid this uncertainty we used an *ab initio* based method described in Sec. 2.4.

The study of Fe clusters extended on 3 different substrates: (0001) surface of Re, (111) fcc and hcp surface of Rh, and $(1\bar{1}0)$ surface of Nb. The study on Re shows, how the $\ell_{\max}$ angular momentum cutoff in partial waves of the electronic structure calculation affects the magnetic configuration. The chains on Rh were used to compare the magnetic configurations from the optimisation scheme and the same for spin dynamics simulations. Since the spin model-based calculation makes possible to include or omit every term of the exchange coupling $\mathbf{J}_{ij}$ tensor one by one, their effect on the magnetic configuration could be separated. Finally Nb,

similarly to Re was recently in the center of interest as hosting possible magnetic-superconducting hetero-structures due to their possible applications in quantum computing. Though here it has to be noted, that the calculations have been carried out in the non-superconducting state, assuming that superconductivity does not affect considerably the magnetic configuration [175].

5.1 Specialties of the conjugate gradient method

As it was presented in Sec. 2.4 we obtained the ground state magnetic configurations after consecutive recalculations of the effective potentials V_{eff} and exchange-correlation field B_{xc}, and searched directions of the exchange correlation field $\mathbf{s}_i$ at each site corresponding to the lowest free energy using the conjugate gradient method. The accuracy of the direction was measured by summing the torque $\mathbf{T}_i$ acting on each site (see Eq. (2.39)):

$$T = \sqrt{\sum_i T_i^2}\,, \tag{5.1}$$

where T_i is the magnitude of torque acting on site i. In all cases the optimization procedure has been done until the relative error of the effective potential and of the magnitude of the exchange-correlation field became smaller than 10^{-9} and 10^{-7}, respectively and the overall torque on the sites, T decreased below 10^{-2} mRy.

In practice, beyond the stable spin-moments of the magnetic cluster we also included the induced moments of the non-magnetic host atoms in the minimization scheme, if their value reached a predefined threshold value, usually chosen as $0.01\,\mu_{\text{B}}$. If the spin moment on site i was smaller than this threshold value, the direction of the local exchange field was set parallel to the direction of the magnetization in the next iteration step. This simplification makes the calculations bearable, since without it e. g on a typical triangular lattice, the inclusion of the first neighbourhood of a magnetic chain into the optimisation scheme would increase the cluster size by 7 times, which would dramatically restrict the size of a manageable cluster, without adding any significant accuracy to the solution. Note that this separation of small and large magnetic moments was considered only during the optimization process, in the electronic structure calculation the neighbourhood atoms were recalculated as well as the magnetic sites.

Note that this method searching for a local minimum of the energy can result in magnetic orientations sensitive to the initial configuration, especially in case of complex magnetic structures. To overcome this problem I used configurations based

on spin model calculations as starting magnetic orientations. Since all major interactions are included into a spin model, these configurations were usually close, i. e they followed the symmetry of the chain and the starting torque was small, but an important obstacle was still to overcome. Symmetry group of spin chains deposited on nonmagnetic substrate often contains only two operations: the identity and a mirror plane perpendicular to the chain. Furthermore, the time reversal that turns around the spin vectors is also a symmetry operation of these systems. Accordingly, there exist two kinds of ground-state spin-configurations being invariant either under the mirror transformation or under simultaneous action of mirror transformation and time reversal. It then follows that the spin vectors can transform either as polar or axial vectors under the mirror plane operation. The initial magnetic structure necessarily follows one of these, and if the energy barrier is high enough this property may not change, and the procedure can end in a metastable state. In order to find the state belonging to lower energy the optimization procedure was to be repeated using a starting configuration obtained by manually rotating the spin into the other symmetry.

5.2 Fe nanoclusters on Re(0001)

Geometry and electronic structure

Rhenium (Re) is a transition metal, which crystallizes in hexagonal close-packed (hcp) structure (space group P63/mmc) with lattice constant of $a_{\mathrm{Re}} = 2.761\,\text{Å}$, and the inter-layer distance between the [0001] planes is 2.281 Å. The geometric structure of the Fe atomic chains on the Re(0001) surface has been investigated by Lászlóffy *et al.* [77] using the Vienna Ab-initio Simulation Package (VASP) [75]. This work considered the relaxation of distance between the surface Re layer and the plane of the clusters on its top, and the distance between the two uppermost layers in the Re substrate. These are 2.228 Å and 2.160 Å, respectively. In my work I used this geometry, which is depicted on Fig. 5.1.

First the electronic structure of the host system was calculated using the SKKR method. The Re(0001) surface was modeled as an interface region between a semi-infinite bulk Re and vacuum consisting of eight monolayers of Re and four atomic layers of empty spheres (vacuum). The iron chains were embedded into the lowermost vacuum layer in hcp positions along the [1000] (x) direction (see Fig. 5.1 right)

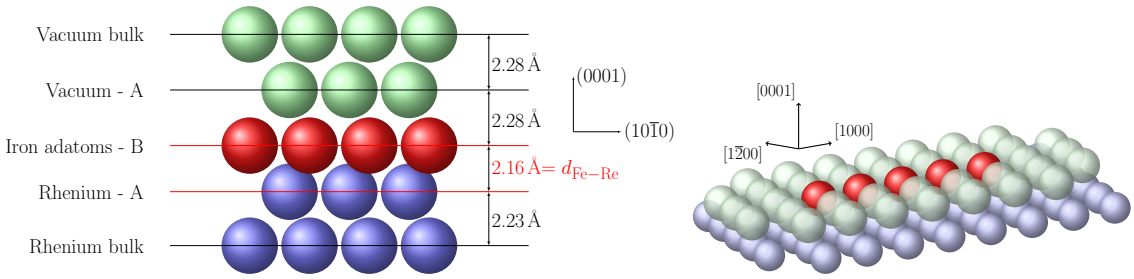

FIGURE 5.1: Left: Side view of the Re(0001) crystal lattice, showing the different layers. The layer in which the Fe atoms were embedded is shown with red, the underlying Re atoms are shown with blue, and the empty vacuum positions with green spheres. The layer–layer distances are obtained from [77]. Right: The concept of positioning Fe atoms (red) into vacuum positions (opaque green) on the top of the Re substrate (blue)

Studying the effect of $\ell_{\max}$

The electron configuration of Re is [Xe] $4f^{14}$ $5d^5$ $6s^2$, and for the Fe is [Ar] $3d^6 4s^2$. As mentioned earlier the core f electrons of Re may influence the sufficient angular momentum cutoff $\ell_{\max}$ of the partial wave expansion in KKR. Two sets of calculations were performed with different $\ell_{\max}$ values to test whether there is a significant change in the magnetic ground state configuration due to the different cutoff.

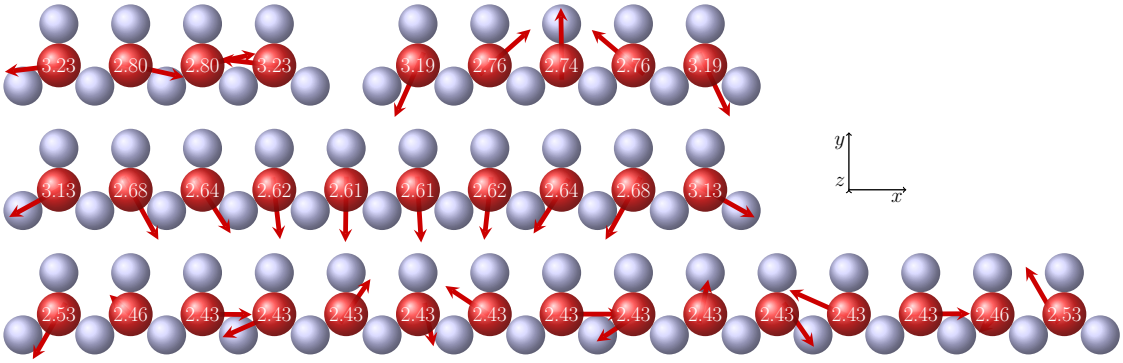

FIGURE 5.2: Different lengths (4, 5, 10, 15) of Fe chains on Re(0001) substrate, with angular momentum cutoff $\ell_{\max} = 2$. The x, y and z directions correspond to the [1000], [1$\bar{2}$00] and [0001] directions, respectively. The red (unit)vectors show the direction of the magnetization vector, while their magnitude is written inside the spheres in μ_B units. The red spheres correspond to the Fe atoms, while the blue ones belong to the underlying Re layer.

The comparison was performed on two shorter chains (4 and 5 Fe atoms), and two longer ones (10 and 15 Fe atoms). All these chains were deposited in the [1000] (x) direction, and the embedded system consisted of the Fe atoms and their first neighbourhood in the Re substrate and in the vacuum region. The obtained magnetic structure from the calculations using angular momentum cutoff $\ell_{\max} = 2$ is in Fig. 5.2., and the one using angular momentum cutoff $\ell_{\max} = 3$ is in Fig. 5.3. The vectors represent the direction of the magnetic moment and its magnitude is

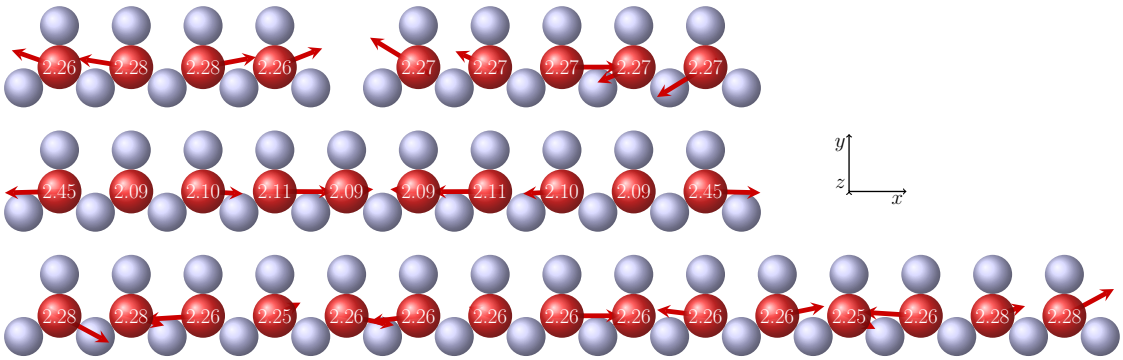

FIGURE 5.3: Different lengths (4, 5, 10, 15) of Fe chains on Re(0001) substrate, with angular momentum cutoff $\ell_{\max} = 3$. The x, y and z directions correspond to the[1000], [1$\bar{2}$00] and [0001] directions, respectively. The red (unit)vectors show the direction of the magnetization vector, while their magnitude is written inside the spheres in μ_B units. The red spheres correspond to the Fe atoms, while the blue ones belong the underlying Re layer.

written inside of each atomic sphere for the Fe sites in μ_B units. For simplicity the induced moments for the Re sites are not included in the figures, their value is about $0.1\,\mu_B$.

First consider the short chains (4 and 5). A general statement is that, the magnitude of the magnetic moments is roughly the same through the chain, and the edge atoms exhibit an enhanced moment, but it is significantly smaller in the larger $\ell_{\max}$ calculation. It is also clear to see that the increase of $\ell_{\max}$ changes the symmetries of both magnetic configurations, which suggests that an important element is added to the calculation when $\ell_{\max}$ is increased. Note that, since the essence of the method is finding a minimum of the band energy, it could have happened that the optimisation procedure was stuck in a metastable state of the opposite symmetry, if the initial configuration was far from the optimum as predicted in the previous section. In order to exclude this possibility, multiple calculations were performed with different initial configurations belonging to different symmetries. It was found that regardless the choice of the initial configuration the result were the same ones presented in Fig. 5.2 and Fig. 5.3. Thus the difference cannot be originated to initial conditions, but to the higher expansion in the partial waves, which fact has to be considered later in the following calculations.

The change of the symmetry does not occur in the case of the longer chains, yet an important difference can be observed in the configurations: in the smaller cutoff case the spins lie in the $x-y$ ([1000] $-$ $-$[1$\bar{2}$00]) plane, and for the larger expansion in the $x-z$ ([1000] $-$ $-$[0001]) plane, which means that in the first case the moments lie in-plane, whereas in the second one the spins are normal to the plane of the substrate, which difference can be essential for applications.

Since the change of $\ell_{\max}$ has a direct effect on the electronic structure, we can

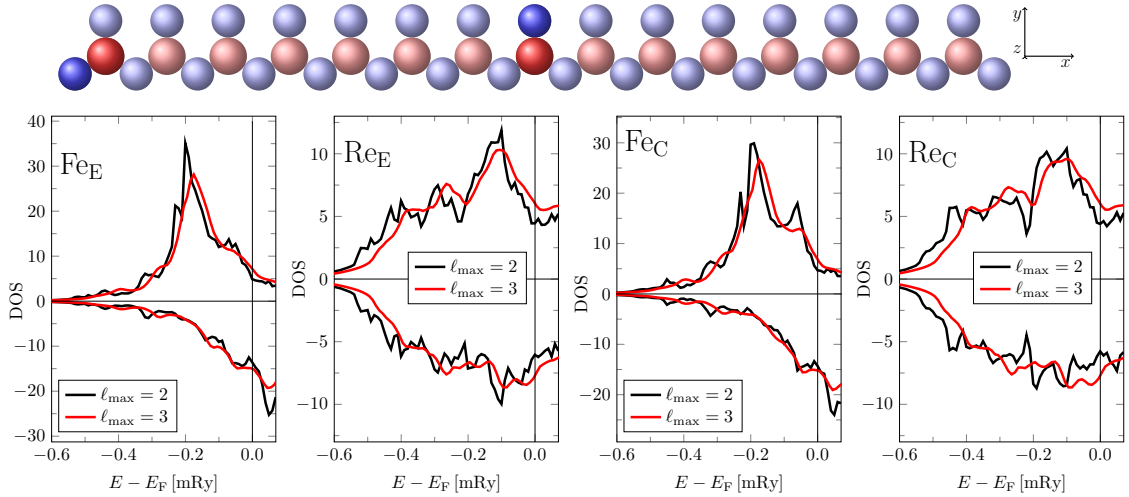

FIGURE 5.4: Up: Schematic view of the 15 atomic chain highlighting the atoms, where the local density of state was calculated. The red and blue spheres correspond to the Fe and Re atoms, respectively. Down: Local density of state for the end (E) and central (C) Fe and Re atoms of the 15 atomic length chain of Fe lying in the [1000] direction on Re(0001) substrate. The Fermi level is shifted to the zero level in both cases. The two colors correspond to the two angular momentum cutoff values, and the positive and negative value curves to the spin up and spin down components.

see how it changes the local density of states (LDOS) on a site. Figure 5.4 shows the LDOS for the Fe and Re atoms lying at the end (E) and in the center (C) of the 15 atomic long chain. Though the change is not dramatic, there peaks is a slight shift in the peaks to higher energies. It is more enhanced for the Re atoms, since the presence of the f electrons. The relative magnetic properties of the central region and at the end atoms are similar in both $\ell_{\max}$ cases.

Spin–spirals

Apart from being a good test system for this method, the rhenium as a substrate owes its recent popularity to the possibility of being a superconducting host system. Kim *et al.* [2] investigated Fe atoms, dimers and chains on superconducting Re(0001) surface using scanning tunneling microscopy/spectroscopy aiming at the discovery of Majorana bound states. By single-atom manipulation techniques they artificially constructed a 40 atom-long-chain of Fe atoms, which exhibited a spin–spiral state with a period of approximately four lattice constants. Lászlóffy and coworkers modelled the same surface in their investigation of higher order spin–spin interactions [77], and found a spin–spiral wavelength of 5 lattice constants. These calculations were performed in the non-superconducting state of Re assuming, that the superconductivity does not influence the magnetic ordering of Fe.

As an example Fig. 5.5 shows the magnetic ground state of the 15 atomic long Fe chain positioned along the [1000] direction, which is a spin–spiral state, as expected.

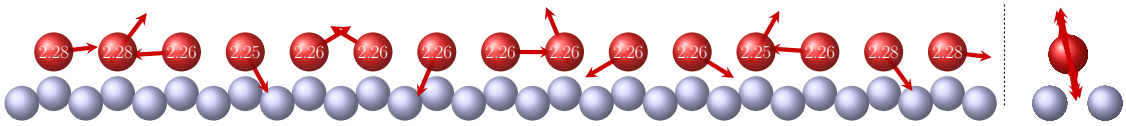

FIGURE 5.5: 15-atom-long Fe chain aligned in the [1000] direction showing spin–spiral ground state on Re(0001) surface with $\ell_{\max} = 3$. The side figure shows the view along the chain direction. The red (unit)vectors show the direction of the magnetization vector, while their magnitude is written inside the spheres in μ_B. The red and blue spheres correspond to the Fe and Re atoms, respectively.

Since our investigations showed that the increase of the angular momentum cutoff of $\ell_{\max}$ has a significant effect on the electronic and magnetic states, in the following we only use the larger, $\ell_{\max} = 3$ expansion when presenting results. The configuration presented here can be compared to the one published in Ref. [77]. Both show a spin–spiral state, though in our case the wavelength is smaller (discussed later). We were able to reproduce the same chirality, which required higher order interactions in the spin model study. This is not a surprise as we expect that the *ab initio* description of the interactions should include all effects. A significant difference is the plane of the spiral, which can be explained with the increase of $\ell_{\max}$, as discussed before.

The calculations were performed for different change lengths from $n = 11$ to $n = 19$ Fe atoms. In order to estimate the spin–spiral wavelength, the rotation angle φ was calculated between every neighbouring spin vector, defined as the following:

$$\varphi_j = \arccos\left(\mathbf{s}_j \cdot \mathbf{s}_{j-1}\right) , \tag{5.2}$$

from $j = 2$ to $j = n$ and $\varphi_1 = 0$. Apart from the effect at the ends, the partial sum of these angles up to the ith position shows a linear behaviour (see Fig. 5.6), and the wavelength was estimated from the slope of the lines. The numerical results are presented in Tbl. 5.1. The values are around $\lambda = 3.4 - 3.6\, a_{2d}$ which is close to the $\lambda_{exp} = 4\, a_{2d}$ experimental value in [2].

TABLE 5.1: The spin–spiral wavelength (λ) in a_{2d} units for different lengths (n) of Fe chains on Re(0001) substrate along the [1000] direction.

$n = 11$	$n = 13$	$n = 15$	$n = 17$	$n = 19$
3.42	3.56	3.40	3.64	3.52

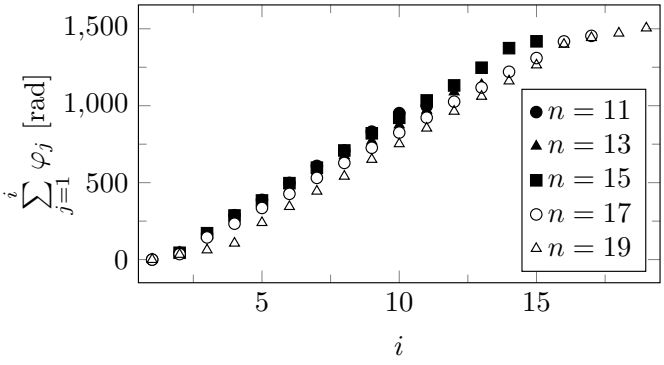

FIGURE 5.6: The cumulative relative rotational angle for every spin vector in spin–spirals in Fe atoms on Re(0001) with different lengths (n) with respect to the first spin.

5.3 Fe chains on Rh(111)

Geometry and electronic structure

Rhodium (Rh) crystallizes in face-centered cubic (fcc) structure (space group: FM-3m) with a lattice constant of $a_{\mathrm{Rh}} = 3.803\,\text{Å}$, which implies that the inter-layer distance between the Rh (111) planes is 2.196 Å. The geometric structure of Fe monolayer on Rh(111) substrate was investigated by Lehnert *et al.* [176]. They found an inward relaxation of the Fe adlayer of 7.3%, setting the Fe-Rh inter-layer distance to $d_{\mathrm{Fe-Rh}} = 2.057\,\text{Å}$. The relaxation of the inter-layer distances between the Rh layers was found to be 1% or less. In our calculations the geometry was based on these numbers, but the change in the Rh inter-layer distances was neglected due to their small size. The geometry of the layered system with the inter-layer distances is shown on Figure 5.7 for fcc and hcp stacking positions of the first vacuum layer, where the Fe is embedded. It should be noted that in Ref. [176] the Fe hcp stacking position was found energetically slightly better than the fcc stacking. In Ref. [177] it was demonstrated that the MAE is remarkably sensitive to the stacking position of Fe and Co adatoms on Rh(111) and Pd(111) surfaces. Since the MAE and, in general, relativistic effects are of great importance in determining the magnetic state of supported nanoclusters, we investigated the magnetic ground state of Fe chains both in fcc and in hcp stacking positions.

In the electronic structure calculations the Rh(111) surface was modeled as an interface region between a semi-infinite bulk Rh and vacuum consisting of eight atomic layers of Rh and four atomic layers of empty spheres (vacuum). The iron chains were embedded into the lowermost vacuum layer denoted with red spheres in Fig. 5.7, on the top of the rhodium. All calculations were performed using angular momentum cutoff $\ell_{\max} = 3$. The detailed calculations were extended to Fe chain

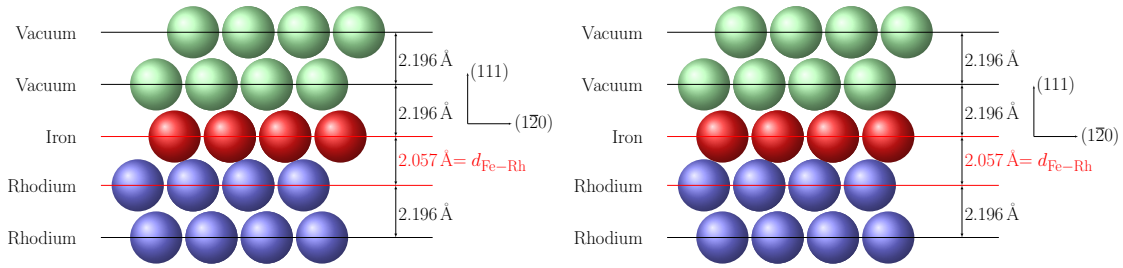

FIGURE 5.7: The layered geometry of Fe atoms on Rh(111) substrate. The left figure shows the fcc stacking positions of Fe, whereas the right one the hcp stacking on the fcc bulk Rh. The underlying Rh atoms are shown with blue, the position of the Fe adatoms with red, and the vacuum with green spheres.

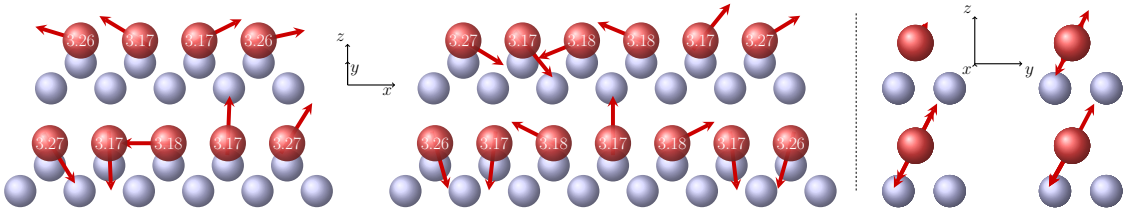

FIGURE 5.8: Fe chains of 4, 5, 6 and 7 atoms on Rh(111) surface with fcc stacking. The x, y and z directions correspond to the $[1\bar{1}0]$, $[1\bar{1}\bar{2}]$ and [111] directions, respectively. The red (unit)vectors show the direction of the magnetization vectors, whereas their magnitude is written inside the spheres in μ_{B} units. The red spheres correspond to the Fe atoms, while the blue ones belong to the underlying Rh layer. The right side pictures show the views along the chain direction.

of the length of 4, 5, 6 and 7 atoms deposited in the $[1\bar{2}0]$ direction in fcc and hcp stacking positions.

Magnetic configurations

Fig. 5.8 shows the magnetic ground state of chains stacked in fcc positions. The magnitude of each magnetic moment is written inside the corresponding sphere, the values are roughly constant, a small oscillation of $0.01\,\mu_{\mathrm{B}}$ can be observed, while the edge moments are slightly enhanced. The magnitude of the nearest induced magnetic moments in the Rh substrate in around is around $0.2\,\mu_{\mathrm{B}}$. The 4- and 7-atom-long chains show polar-vector symmetry, while the magnetic moments in the 5- and 6-atom-long chains behave as axial vectors. A tempting assumption is, that the building blocks of these configurations are pairs of spins being aligned closely parallel to each other ($\uparrow\uparrow$), while these dimers seem to be coupled antiparallel to each other resulting in a pair-wise antiferromagnetic state ($\uparrow\uparrow\downarrow\downarrow$). This structure is particularly apparent for the chains containing even number of magnetic atoms, i. e. the even chains. In case of chains containing odd number of Fe atoms – the odd chains, as abbreviated later – the $\uparrow\uparrow\downarrow\downarrow$ alternation is necessarily broken, which gives rise to more noncollinear spin configurations. This can be explained with the fact that the

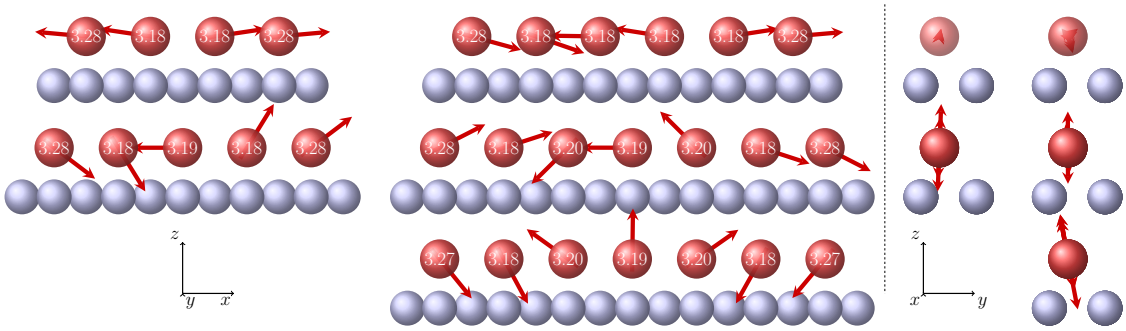

FIGURE 5.9: Fe chains of 4, 5, 6 and 7 atoms on Rh(111) surface with hcp stacking. The x, y and z directions correspond to the $[1\bar{1}0]$, $[1\bar{1}\bar{2}]$ and [111] directions, respectively. Out of the two 7-atom-long chains the upper one with axial vector symmetry is the ground state, while the lower one with polar-vector symmetry is a metastable state. The red (unit)vectors show the direction of the magnetization vectors, whereas their magnitude is written inside the spheres in μ_B units. The red spheres correspond to the Fe atoms, whereas the blue ones belong the underlying Rh layer. The right side pictures show the views along the chain direction.

central spin in an odd chain must be aligned either normal to the chain i. e. polar-vector symmetry or parallel to the chain i. e. axial-vector symmetry. Apparently, noncollinearity of the spins is present in the even chains too. Furthermore, all ground state spin configurations are coplanar with the planes tilted to the z axis by roughly the same angle: 22° for the 4-atom-long chain, and around 27° for the longer chains.

Fig. 5.9. shows the magnetic ground state of chains stacked in hcp positions. The magnitudes of the spin moments are very similar to those obtained for the chains with fcc stacking. Concerning the ground state spin configurations, the double pair-wise AFM structure keeps dominating, and the collinearity is much enhanced for the even chains. As in case of fcc stacking the odd chains with hcp stacking show a largely non-collinear magnetic ground state, while the plane of the magnetic moments is almost normal to the surface. For the 7-atom-long chain the magnetic ground state shows axial-vector symmetry. In addition, we also found a metastable state with polar-vector symmetry depicted in the last entry of Fig. 5.9, which is by 16.3 meV higher in energy than the ground state. These two configurations are related to each other by about 90° global rotation around the normal of the plane of the spins, while the metastable configuration is slightly tilted from the z axis. Note that both configurations have right-handed chirality.

TABLE 5.2: The most significant $J_{i,j}$ isotropic exchange couplings between at sites i and j in fcc (left) and hcp-stacked (right) Fe chains of n atoms in mRy units. (only independent ones)

	fcc stacked				hcp stacked			
$i-j$	4	5	6	7	4	5	6	7
$1-2$	0.604	0.572	0.686	0.605	0.437	0.339	0.378	0.363
$1-3$	-0.562	-0.624	-0.614	-0.599	-0.527	-0.599	-0.546	-0.573
$2-3$	0.114	0.331	0.558	0.322	0.186	0.288	-0.163	0.076
$2-4$		-0.441	-0.456	-0.406		-0.370	-0.357	-0.347
$3-4$			1.181	0.227			-0.117	-0.190
$3-5$				-0.420				-0.363

Spin model calculation

The main features of the ground state spin configurations for the different chains can be understood in terms of a bilinear spin model:

$$H = -\frac{1}{2}\sum_{i,j} \mathbf{s}_i \mathbf{J}_{i,j} \mathbf{s}_j + \sum_i \mathbf{s}_i \mathbf{K}_i \mathbf{s}_i \ , \tag{5.3}$$

where i and j are restricted to the Fe sites, and the $\mathbf{J}_{i,j}$ and $\mathbf{K}_i$ are generated from the potentials which are converged in respect to the whole embedded region, using the SCE method (see Sec. 2.2.2).

The leading terms in the spin model are the isotropic exchange interactions. The nearest-neighbour (NN) and next-nearest-neighbour (NNN) isotropic interactions between the Fe atoms are presented in Tbl. 5.2 for both Fe stackings. First let us discuss the fcc stacked case. Apparently, the NN and NNN isotropic interactions are ferromagnetic (FM) and antiferromagnetic (AFM), respectively. These interactions are consistent with the alternating $\uparrow\uparrow\downarrow\downarrow$ structure seen as the dominant feature of the even chains. The largest FM coupling is between the inner atoms of the $n = 6$ chain, which further stabilizes this spin structure. In the case of odd number of atoms this pair-wise AFM configuration is obviously broken. Note that the comparison from the data of chain 4 and 6, or 5 and 7 shows, that the ferromagnetic coupling is stronger with the increase of the length, which foreshadows that for a much longer chain the pair-wise AFM behaviour may vanish.

The right side of Tbl. 5.2 shows the isotropic interactions for the hcp-stacked case. The FM coupling within the dimer elements is weak, indeed it becomes antiferromagnetic for the middle atoms in the longer chains. The AFM coupling between the NNN atoms is roughly unchanged, the 1–3 term is dominating in all cases and it is strong enough so that the same pair-wise antiferromagnetic orientation appears.

Here it should be noted that a ↑↑↓↓ double-row-wise AFM structure has been theoretically predicted [178] and experimentally observed [179] in an Fe monolayer on Rh(111). While the emergence of such a spin structure in a monolayer requires the presence of higher-order (in particular, three-site four-spin) interactions [179], for a chain of finite length it can be stabilized by the inhomogeneous bilinear isotropic interactions only.

Spin dynamics simulations

The effect of different kinds of exchange interactions in the formation of the magnetic ground state is demonstrated for the fcc-stacked cases of the shorter, 4- and 5-atom-long chains. For this reason – in three consecutively simulations – three sets of spin model parameters were considered: (a) isotropic interactions and on-site anisotropy matrices, (b) the previous spin model extended by DMI and (c) the spin model with full tensorial interactions as in Eq. 5.3. The obtained spin configurations are presented in Fig. 5.10.

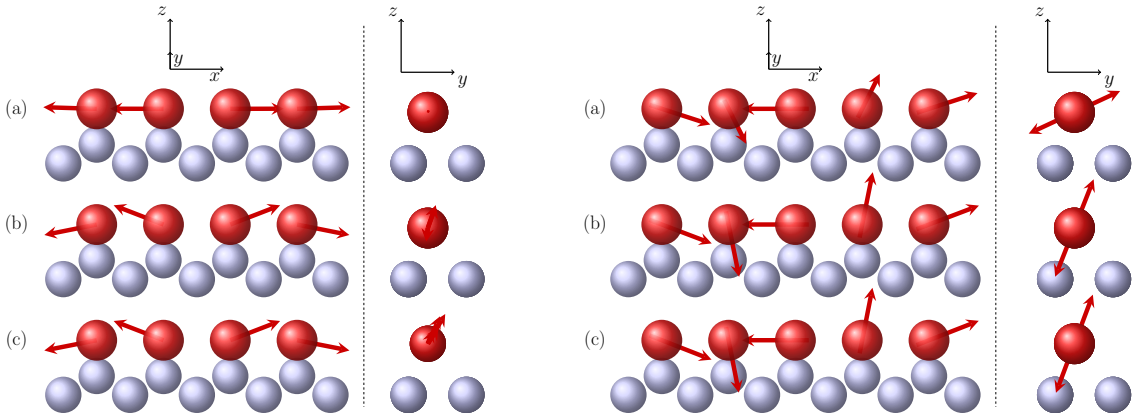

FIGURE 5.10: Ground state spin configurations of 4-atom-long and 5-atom-long Fe chains in fcc-stacked position on Rh(111) surface from spin dynamics simulations. The three subfigures show simulations with different spin models: (a) with only isotropic exchange coupling and onsite anisotropy, (b) the previous one extended with DMI, (c) the whole $\mathbf{J}_{ij}$ exchange tensor is included. The right side images show the views along the chain direction. The x, y and z directions correspond to the $[1\bar{1}0]$, $[1\bar{1}\bar{2}]$ and $[111]$ directions, respectively.

In case of the 4-atom-long chain – the left panel of Fig. 5.10.–, when only isotropic exchange interactions (see Tbl. 5.2) and on-site anisotropies are present, the simulations resulted in to a nearly collinear double-pair-wise (←←→→) AFM configuration along the chain direction due to an easy x-axis anisotropy. This configuration clearly respects a polar-vector symmetry. The y-components of the DM vectors introduce non-collinearity of the spin structure in the x–z plane by keeping the polar-vector symmetry. In addition, the plane of the spins is slightly rotated to

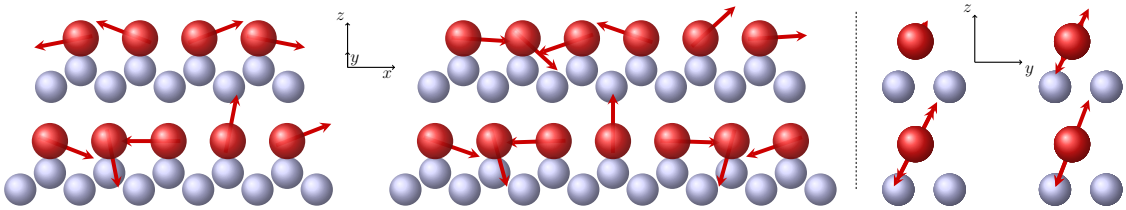

FIGURE 5.11: Ground state spin configuration from spin dynamics simulations for 4-, 5-, 6-, and 7-atom-long Fe chains in fcc-stacked position on Rh(111) surface The spin model included the whole $\mathbf{J}_{ij}$ exchange tensor. The right side images show the views along the chain direction. The x, y and z directions correspond to the $[1\bar{1}0]$, $[1\bar{1}\bar{2}]$ and [111] directions, respectively.

the y axis, which shows the preference of the y axis with respect to the z axis by on-site anisotropy (for a discussion of the tilting of spin–spiral states see Ref. [77]). Switching on the symmetric exchange anisotropy does not have considerably effect on the spin configuration.

In case of the 5-atom-long chain, – right panel of Fig. 5.10. – , the frustration of the isotropic exchange interactions (see Tbl. 5.2) causes a strongly non-collinear spin arrangement, with the middle spin oriented along the chain, again due to easy x-axis anisotropy. Thus the ground state exhibits an axial-vector symmetry. The views along the chain direction of the spin configurations show that the plane of the spins is slightly tilted away from the x–y plane of the substrate, which is mainly attributed to the nonvanishing xz components of the on-site anisotropy matrices $\mathbf{K}_i$. Switching on the DMI further stabilizes this configuration by just slightly changing the relative angles between the spins. On the other hand, the plane of the spins is tilted much closer to the x–z plane which can be attributed to large y components of the DM vectors [77]. As found for the 4-atom-long chain, including the symmetric exchange anisotropy has negligible effect on the magnetic ground state configuration.

The ground state configurations from the spin dynamics simulations of all fcc-stacked Fe chains are shown in Fig. 5.11. The configurations obtained from *ab initio* optimization (Fig. 5.8) and the ones based on the bilinear tensorial spin model (Fig. 5.11) compare remarkably well. However, in particular, for the longer chains larger differences occur mostly at the ends. In order to quantify the differences between the magnetic configurations obtained from these two methods we use the average mean deviation of the spin vectors Δ, the square of which is defined as

$$\Delta^2 = \frac{1}{n}\sum_{i=1}^{n}\left(\mathbf{s}_i^{\mathrm{m}} - \mathbf{s}_i^{\mathrm{a}}\right)^2 , \tag{5.4}$$

with $\mathbf{s}_i^{\mathrm{m}}$ and $\mathbf{s}_i^{\mathrm{a}}$ being the spin vectors at site i obtained from the spin dynamics simulation and the *ab initio* optimization, respectively.

TABLE 5.3: The mean deviation Δ, defined by Eq. (5.4) between the magnetic ground states of fcc- and hcp-stacked Fe chains with atomic lenngth n on Rh(111) obtained from *ab initio* optimization and from the spin dynamics simulations based on Eq. (5.3).

	$n = 4$	$n = 5$	$n = 6$	$n = 7$
fcc	0.332	0.417	0.297	0.601
hcp	0.244	0.366	0.650	0.716

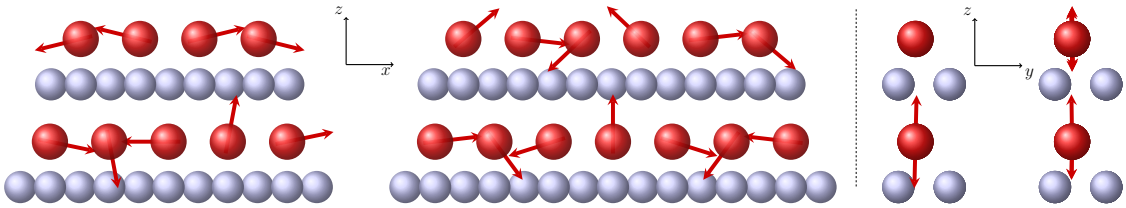

FIGURE 5.12: Ground state spin configuration from spin dynamics simulations for 4-, 5-, 6-, and 7-atom-long Fe chains in hcp-stacked position on Rh(111) surface The spin model included the whole $\mathbf{J}_{ij}$ exchange tensor. The right side images show view along the chain direction. The x, y and z directions correspond to the $[1\bar{1}0]$, $[1\bar{1}\bar{2}]$ and [111] directions, respectively.

The mean deviations for both stackings and all considered chains lengths are summarized in Tbl 5.3. It is apparent – more enhanced for the fcc-stacked case – that the agreement between the magnetic ground states based on *ab initio* optimization and on the spin model is significantly better for even chains, which might be attributed to the missing geometrical frustration, thus the reduced non-collinearity in these systems. The 6-atom-long hcp stacked chain shows an especially large deviation in comparison to the fcc-stacked one. This is visually also conspicuous by comparing the *ab initio* optimized (Fig. 5.9) and spin model-based configurations (Fig. 5.12). The coplanar chain in the x–z plane is perfectly reproduced by the spin models, but the spin dynamics forces the chain into a spin–spiral like configuration, which was not as apparent after the optimization. The evaluation of each contribution showed, that this effect can be traced back to the DM interaction.

5.4 Fe chains on Nb(110)

Geometry and electronic structure

Similarly to the Re(0001) surface the deposited magnetic atomic chains on Nb(110) are supposed to host Majorana edge states [2–4]. Bulk Nb has a bcc structure with lattice constant of $a_{\mathrm{Nb}} = 3.3004\,\text{Å}$. Using the Vienna Ab-initio Simulation Package (VASP) [75] Lászlóffy *et al.* [180] found that by putting an Fe adatom on the (110) surface of Nb, the average vertical distance of the atoms in the two uppermost Nb layers decreases from the bulk value of 2.3337 Å by 3.4 % to 2.2542 Å, while the

vertical distance between the Fe adatom and the closest Nb atoms was found to be 1.9868 Å. In our calculations we used these values as the interlayer distances between the uppermost two Nb layers, as well as between the Nb surface layer and the first two vacuum layers, in which the Fe atoms were embedded [180], respectively.

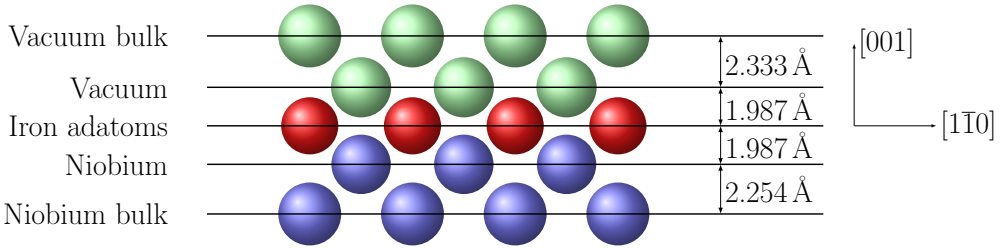

FIGURE 5.13: The layered geometry of Fe atoms on Nb(110) substrate. The underlying Nb atoms are shown with blue, the position of the Fe adatoms with red, and the vacuum with green spheres.

The ground state in Ref. [180] – determined from spin model calculations – was found to be FM/AFM – depending on the sign of NN isotropic coupling – parallel to the z direction in the case of Fe chains deposited along the [001] and [1$\bar{1}$1] directions. The chains deposited along the [1$\bar{1}$0] direction exhibited a spin–spiral with a wavelength of $\lambda = 3.39\, a_x$, where $a_x = \sqrt{2} a_{\mathrm{Nb}}$ is the distance between the two subsequent Fe atoms in the chain.

The substrate was modeled by eight Nb layers and four empty sphere layers sandwiched between semi-infinite bulk Nb and vacuum regions. Similarly to the previous substrates an angular momentum cutoff of $\ell_{\max} = 3$ was used in the calculations. The Fe atoms were embedded in the lowermost vacuum layer along the most promising [1$\bar{1}$0] direction, as shown on Fig. 5.14.

Magnetic structure

The study included the optimization of the magnetic ground state of 5-, 10- and 15-atom-long Fe chains deposited along the [1$\bar{1}$0] direction. Similarly, to Ref. [180], we found that the ground state of these chains is a spin–spiral. Fig. 5.15 shows

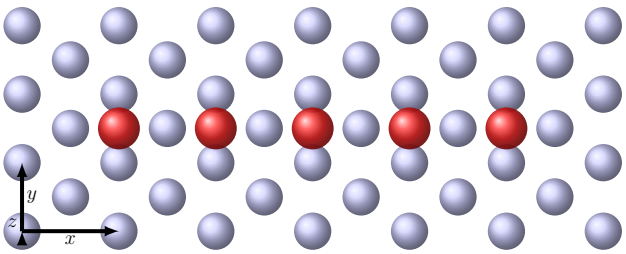

FIGURE 5.14: The top view of Fe atoms positioned on the top of Nb(110) surface along the [1$\bar{1}$0] direction. The Fe and Nb atoms are denoted by red and blue spheres, respectively. The x, y and z directions correspond to the [1$\bar{1}$0], [001] and [110] directions, respectively.

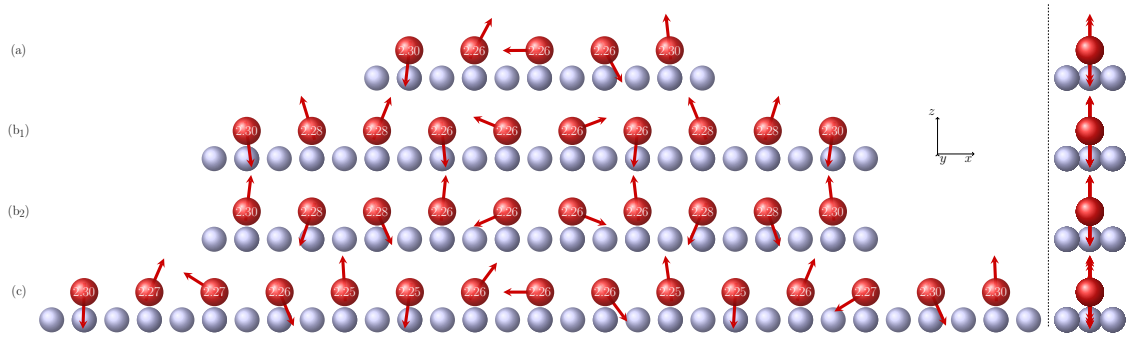

FIGURE 5.15: Magnetic ground state of of 5-, 10-, and 15-atom-long Fe chains (red) along the x direction on Nb(110) substrate (blue). (b_1) is a metastable and (b_2) is a ground state for the 10-atom-long chain. The x, y and z directions correspond to the $[1\bar{1}0]$, [001] and [110] directions respectively. The magnitude of each magnetic moment in inside the sphere in μ_B units.

the obtained configurations. For the 10-atom long chain two optimized magnetic configurations are presented. Due to the fact that the hard axis of the system is y, the spins rotate perfectly in the $x-z$ plane as can be observed at the side subfigure of Fig. 5.15. Using the same method as for the Re substrate, the spin–spiral wavelength is estimated from the rotation angles of the spins with respect to the x axis (see Eq. (5.2)), and presented in Tbl. 5.4. Apart from the 5-atom-long chain, where the effect from the end of the chain is most enhanced, the results differ by about 15% as compared to Ref. [180].

TABLE 5.4: The spin–spiral wavelength (λ) in a_x units for different lengths of Fe chains on Nb(110) substrate along the $[1\bar{1}0]$ direction.

$n = 5$	$n = 10$	$n = 15$
2.19	2.90	2.84

The metastable (Fig. 5.15(b_1)) and ground state configuration (Fig. 5.15(b_2)) of the 10-atom long chain have opposite rotational sense. The ground state is lower in energy by 1.7 meV than the metastable state, converted into about 0.08 meV/atom, which is indeed in the energy range of the DMI of these chains [180]. It is pointed out in Ref. [180] that the frustrated isotropic interactions and the relatively strong anisotropy can stabilize spin–spirals with opposite chirality for longer chains. Here should be noted, that all ground state spin–spirals obtained from the *ab initio* optimisation have a left-handed (anti-clockwise) rotational sense as opposed to those obtained from the spin model [180], which have a right-handed (clockwise) rotational sense. This discrepancy might be attributed to the higher-order chiral spin—spin interactions [77, 181], which are missing in the spin model used in Ref. [180], but their effect is included in the fully *ab initio* optimization used here.

Chapter 6

Summary

In this Thesis I covered 3 different topics. The first one is related to the temperature dependent magnetic anisotropy energy (MAE) and temperature induced spin reorientation transitions (SRT) in magnetic ultrathin films, which have technological importance in the magnetic data storage. The second one is the thermodynamic properties of skyrmionic structures, such as the number of skyrmionic objects in equilibrium, and their respective chemical potentials in two ultrathin skyrmion–hosting films. The third, and final topic is the magnetic ordering of spin chains of Fe atoms on nonmagnetic heavy metal surfaces.

The temperature dependent magnetism of ultrathin films was investigated using well-tempered metadynamics Monte Carlo simulations. The essence of the method is to add a biasing potential to the energy of the system and thus enable the it to overcome the energy barriers between different local energy minima. This way the global energy extremum of the system can be found, and by bookkeeping the biasing potential the whole free energy surface can be mapped. The key physical property in the calculation of MAE is the orientation of the magnetic moment. This is the reason why the normal-to-plane component of the magnetization vector was chosen as a collective variable in the metadynamics simulations, and the MAE could be calculated as the energy difference of two points of the free energy surface.

First I worked with model systems. I investigated the MAE originated from the on-site anistropy and from the two-site anisotropy, and I found a comforting agreement with the previous work of Callens [108]. The SRTs can be explained by the change of the easy direction of magnetism due to an external effect, usually film thickness and temperature [6]. My studies showed that the MAE contributions originated from different sources have different temperature dependence, thus by using a well-chosen anisotropy constants in the model, the competition of two opposite terms can bring forth a spin reorientation transition. I was able to induce this phenomenon in model monolayers and bilayers too. In the latter case the numerical results were reinforced by a theoretical study on the ground state and a mean field estimation of the reorientation temperature. I was able to draw the phase diagram

of the reorientation transition with respect to the anisotropy parameters. Interestingly I found that the course of the process depends not only on the value of the anisotropy, but also on its distribution in each layers: if the anisotropy agrees in the two layers, then the transition will be of second order, yet if all anisotropy is attributed to a single one of the two layers, then a first order phase transition is to be observed. This discovery is due to the fact, that the metadynamics simulation not only gives back the MAE, but the whole free energy surface. The shape of these curves clearly shows the evolution of extrema, and thus the order of transition can be read.

The investigation of MAE was extended to the studies of real, experimentally motivated [19, 64] systems, where the magnetic interactions were based on *ab initio* calculations. The study on Fe adlayers on Au(001) showed that the simulations are still feasible if the number of coupling parameters is increased by orders of magnitudes compared to the model study. The simulations in line with preliminary expectations showed that a bilayer has easy-axis and a trilayer has an easy-plane magnetization, and the thickness driven spin reorientation happens between these cases. The more detailed study of the bilayer gave back the expected temperature dependence of the MAE, and the interplay of the anisotropy contributions can be discovered in the MAE of the trilayer. The study on Fe bilayer on W(110) focused on the temperature driven SRTs. The speciality of this system is that the newly discovered DMI induced anisotropy term [155] plays a decisive role in the transition. The metadynamics MC simulations showed that a normal-to-plane to in-plane spin reorientation transition happens around $T_\mathrm{r} = 350\,\mathrm{K}$. The omission of the DM term from the exchange couplings resulted in the disappearance of the phenomenon, which foreshadows that the DMI gives an in-plane anisotropy term to the MAE. This energy difference could be well estimated by a spin–spin correlation function. Understanding SRTs is essential in engineering to set the thickness of the layers in heterostructures for stable room–temperature spintronic applications.

I modified the well-tempered metadynamics MC code to use the topological charge as the collective variable governing the simulation. This made possible to enforce the systems into states where nontrivial topological objects, i. e. skyrmions and antiskyrmions appear, and the bookkeeping of the bias potential made possible to estimate the optimal number of these structures. Though there is no clear correspondence between the topological charge and the number of skyrmionic particles in the system for general B-T parameters, yet at low temperatures with a low density of skyrmionic objects one can suppose a non-interacting picture, where the overall free energy of the lattice is only proportional to the number of skyrmions or antiskyrmions. This appeared as a linear region of the free energy $F(Q)$ curve around

the $Q = 0$ point. Here the respective chemical potential of skyrmions and antiskyrmions could be defined from the slope of $F(0)$ in the $Q < 0$ and $Q > 0$ regions. This definition is highly dependent on the free particle picture. As the temperature is increased more and more skyrmionic objects appeared on the lattice, and after reaching a certain density their interaction cannot be neglected anymore, since the energy contribution originated from the skyrmion-skyrmion interactions distorted the linear $F(Q)$ function to a parabolic one. I studied two heavy metal/iron skyrmion–hosting bilayers, namely $(Pt_{0.95}Ir_{0.05})$/Fe/Pd(111) and Pd/Fe/Ir(111). In the former one I reproduced the $\langle Q \rangle(T)$ behaviour published in Ref. [35]. The extension of the calculation for multiple particles made possible to obtain the chemical potential of the skyrmionic particles. The later system has a richer choice of ground states depending on the external magnetic field, namely the spin–spiral, the skyrmion lattice and also the field polarized ground state appear as the external magnetic field B is increased. For all instances I obtained the $\langle Q \rangle(T)$ curve, which was in good agreement with Ref. [70]. For the first two cases I found that at low temperatures the skyrmions are not stable objects, and the lattice is filled with extensive domain walls instead. Since here the topological charge is originated from the ends of the intertwined spin–spiral segments, and not from independent particles, the chemical potential could not be defined. In the field polarized ground state, where skyrmions can appear freely in a ferromagnetic background, the result was similar to the other hosting system. An important difference of $(Pt_{0.95}Ir_{0.05})$/Fe/Pd(111) and Pd/Fe/Ir(111) is that in the first system both skyrmions and antiskyrmions have positive chemical potential, meaning they have positive energy cost in a field-polarized ground state and thus their creation is highly unfavourable, but for the $B = 4\,\mathrm{T}$ case in Pd/Fe/Ir(111) the one belonging to the skyrmions is negative, meaning that the formation of $Q = -1$ skyrmions is energetically favourable. Interestingly in all cases I found that the chemical potential belonging to antiskyrmions is larger than that of the skyrmions.

I used the *ab initio* optimization method used in Ref. [55] supplemented with the conjugate gradient method to obtain the magnetic structure of atomic chains. Today, when more and more studies show the necessity of higher order spin interactions in the precise description of the magnetic structure, the usage of this kind of method can avoid the necessity of permanent supplementation of the spin models. I investigated Fe chains on nonmagnetic heavy metal surfaces, such as Re(0001), Rh(111) and Nb(110). The studies of Fe chains on the (0001) surface of Re with different lengths showed an outstanding importance of the choice of the angular momentum cutoff $\ell_{\max}$ in *ab initio* electronic structure calculations. This result is a sign, that the core f electrons influence the electronic structure in a way that has a significant consequence on the magnetic structure, which has to be considered

in future calculations. Furthermore I was able to reproduce the spin–spiral state for atomic chains of length between 10 and 20 atoms with a wavelength close to the experimentally measured value on a 40 atom-long chain in Ref. [2]. Using this higher $\ell_{\max}$ in the partial wave expansion in the electronic structure calculation, I was able to reproduce the spin–spiral configuration found in Fe chains deposited in the $[1\bar{1}0]$ direction on Nb(110). Interestingly for the 10 atomic-long-chain I found a ground state with opposite chirality in contrast to the spin model-based results in Ref. [180]. I made a detailed analysis on the comparison of the *ab initio* optimised and the spin model-based magnetic configurations on Rh(111) surface. The different spin models, based on the separation of the different terms in the $\mathbf{J}_{ij}$ coupling tensor, showed the contribution of each interaction in the formation of the final configuration. The two-atom wide stripes found in an Fe monolayer on Rh(111) [178, 179] clearly appeared as strong ferromagnetic nearest-neighbour and antiferromagnetic next-nearest-neighbour couplings in the spin model. In the even-atomic-long chains this interaction manifested as a double-pairwise pattern both in spin model-based and *ab initio* optimized configurations. In the odd-atomic-long chains this effect caused the frustration of couplings, and such a pattern could not appear. The different configurations for hcp and fcc stacked chains showed that the stacking has an influence on the orientation of the magnetic moments. All these results, which are in good agreement with previous experimental observations, show that the *ab initio* method I used can describe the magnetic structure with good accuracy, and it can also be used effectively in later research.

My studies showed that the metadynamics method is a very efficient tool in the research of ultrathin magnetic films. Although the standard Monte Carlo simulation is useful to obtain the ground state of a simple system, it can fail if many metastable states are possible. This can be avoided with a good choice of an external parameter as collective variable in a well-tempered metadynamics MC simulation, and in addition the free energy surface can be mapped too, to compare different configurations. Since the choice of the CV can be easily changed depending on the emphasis of the study, many seemingly different arrangements such as ferromagnets, skyrmions and spin–spirals can be investigated. As for chains the ground state configurations are much more important, and that is the reason why our *ab inito* optimisation scheme can be a very useful complementary tool beside the spin dynamics simulations. Although perpendicular magnetic anisotropy, skyrmions and Majorana modes in magnetic chains are important in different materials, but all these effects are the foundation of possible data storage techniques, which will be important to address humanity's continously increasing demand for larger information storing devices.

Chapter 7

Thesis Statements

1. First I used the well-tempered metadynamics method on model spin Hamiltonians describing magnetic thin films. I investigated the temperature dependence of the magnetic anisotropy energy in the case of purely on-site and purely two-site anisotropies and found a good agreement on the magnetic anisotropy energy with the Callen–Callen theory. I found that these two terms have a different temperature dependence, which can lead to a spin reorientation transition (SRT) due to the competition of the two. This phenomenon has been demonstrated first in a single monolayer. In the case of a bilayer system the richer behaviour of the phase transitions have been found, namely first and second order phase transitions were discovered depending on the distribution of the anisotropy of the system.

   These results are discussed in Sec 3.3 and Sec. 3.4, and they are published in Pub. II.

2. I studied the magnetic anisotropy of $Fe_n/Au(001)$ ($n = 2, 3$) and $Fe_2/W(110)$ using well-tempered metadynamics method.

   For the first system, I calculated the magnetic exchange parameters for different Fe-Au layer-to-layer distances, then I used a selected one in the simulations to calculate the temperature dependent magnetic anisotropy energy. I showed, that this system fulfills the Callen–Callen theory. The investigation of free energy surfaces showed that a thickness driven spin reorientation transition happens between $n = 2$ and $n = 3$.

   The Dzyaloshynsky–Moriya interaction (DMI) plays a crucial role in the spin reorientation transition taking place in the Fe bilayer on W(110). I showed that at finite temperature an additional anisotropy term appears, which can be explained by the arising finite temperature fluctuations in the system. I proved that without the DMI, the spin-reorientation transition would not happen in the system.

These results are shown in Sec 3.5 and in Sec 3.6, and they are published in Pub. I., II. and III.

3. I further developed the well-tempered metadynamics code to use the topological charge as a collective variable. With this modified version I investigated the temperature dependence of creation and annihilation of skyrmionic objects in heavy metal/iron bilayers, namely $(Pt_{0.95}Ir_{0.05})$/Fe/Pd(111) and Pd/Fe/Ir(111). I found that at the low temperatures in a low density the skyrmions and antiskyrmions act as particles, thus their respective chemical potential can be defined. Finite temperature chemical potential curves showed that for the investigated $(Pt_{0.95}Ir_{0.05})$/Fe/Pd(111) bilayer both skyrmion and antiskyrmion creation is energetically unfavourable, but for Pd/Fe/ Ir(111) in a magnetic field range, where the ground state is field polarized I found negative chemical potential for skyrmions, showing that their formation is a favourable process, i. e. with the given $B - T$ parameters their creation from the field polarized background is a favourable process.

   The corresponding results are in Chapter 4, and published in Pub. V.

4. I used *ab initio* optimization to obtain the ground state magnetic configuration of Fe chains on different heavy metal substrates. The calculations on Re substrate highlighted how the choice on the angular momentum cutoff in the electronic structure calculation can influence the magnetic structure. I reproduced the experimentally measured spin–spiral states in the Fe chains on Re(000) and Nb(110), with a good agreement on the wavelengths. The extensive study on Fe atomic chains on Rh(111) showed how the stacking can influence the magnetic configuration, and the comparison with spinmodel simulations pointed out how each term of the exchange coupling contributes to the formation of the magnetic configuration.

   The results are in Chapter 5 and they are published in Pub. IV.

Publications related to the thesis statements

I B. Nagyfalusi L. Udvardi and L. Szunyogh, First principles and metadynamics study of the spin-reorientation transition in Fe/Au(001) films, IOP Conf. Ser.:, J. Phys. Conf. Ser. **903**, 012016 (2017)

II Nagyfalusi, L. Udvardi and L. Szunyogh, Metadynamics study of the temperature dependence of magnetic anisotropy and spin-reorientation transitions in ultrathin films. Phys. Rev. B **100**, 174429 (2019)

III B. Nagyfalusi, L. Udvardi L. Szunyogh, and L. Rózsa, Spin reorientation in an ultrahin Fe film on W(110) induced by Dzyaloshinsky-Moriya interactions, Phys. Rev. B **102**, 134413 (2020)

IV B. Nagyfalusi, L. Udvardi and L. Szunyogh, Magnetic ground state of supported monatomic Fe chains from first principles, J. Phys. Cond. Mat. **34** 395803 (2022)

V B. Nagyfalusi, L. Udvardi L. Szunyogh, and L. Rózsa, Chemical potential of magnetic skyrmion quasiparticles in heavy metal/iron bilayers, sent to Phys. Rev. B, arxiv: 2312.05535 (2023)

Acknowledgements

First and foremost I would like to gratefully thank László Udvardi for all the help and guidance over our work, since I began to work on my BSc. Thesis. He introduced me in electronic structure calculations, in scientific computing and showed me the mysteries of using Linux and a computer cluster. His door was always open anytime I got stuck with the scientific or programming work.

A would like to thank László Szunyogh for the joint work, his scientific viewpoint and the great effort what he always does during the publication process.

I would also thank Levente Rózsa for his recommendations of topics, and András Lászlóffy for his fast and helpful replies for my coding errors. I am thankful for Krisztián Palotás for our work in the last two years and for reading this work. Also I would like to express my thank for the many other members during the last decade of Computational Magnetism Group here at the BME and the Long Range Order in Condensed Systems Research Group at at the Wigner Research Center for their advises and the inspiring and friendly environment.

Last but not least, I would like express my thank to my parents, my family and all my friends for their support, caring and peaceful background during these years.

Bibliography

[1] R. Wiesendanger. "Spin mapping at the nanoscale and atomic scale". In: *Rev. Mod. Phys.* 81 (2009), pp. 1495–1550. DOI: 10.1103/RevModPhys.81.1495.

[2] H. Kim et al. "Toward tailoring Majorana bound states in artificially constructed magnetic atom chains on elemental superconductors". In: *Sci. Adv.* 4 (2018). DOI: 10.1126/sciadv.aar5251.

[3] P. Beck et al. "Spin-orbit coupling induced splitting of Yu-Shiba-Rusinov states in antiferromagnetic dimers". In: *Nat. Commun.* 12 (2021), p. 2040. DOI: 10.1038/s41467-021-22261-6.

[4] D. Crawford et al. "Majorana modes with side features in magnet-superconductor hybrid systems". In: *npj Quantum Mater.* 7 (2022). DOI: 10.1038/s41535-022-00530-x.

[5] L. Néel. "Anisotropie magnétique superficielle et surstructures d'orientation". In: *J. Phys. Radium* 15 (1954), p. 225. DOI: 10.1051/jphysrad:01954001504022500.

[6] U. Gradmann and J. Müller. "Flat Ferromagnetic, Epitaxial 48Ni/52Fe(111) Films of few Atomic Layers". In: *Phys. Status Solidi (b)* 27 (1968), pp. 313–324. DOI: 10.1002/pssb.19680270133.

[7] M. T. Johnson et al. "Magnetic anisotropy in metallic multilayers". In: *Rep. Prog. Phys.* 59 (1996), p. 1409. DOI: 10.1088/0034-4885/59/11/002.

[8] P. Grünberg. "Layered magnetic structures: history, facts and figures". In: *Journal of Magnetism and Magnetic Materials* 226-230 (2001). Proc. Int. Conf. Magn. (ICM 2000), pp. 1688–1693. DOI: https://doi.org/10.1016/S0304-8853(00)01050-7.

[9] H. X. Yang et al. "First-principles investigation of the very large perpendicular magnetic anisotropy at Fe|MgO and Co|MgO interfaces". In: *Phys. Rev. B* 84 (2011), p. 054401. DOI: 10.1103/PhysRevB.84.054401.

[10] A. A. Timopheev et al. "Second order anisotropy contribution in perpendicular magnetic tunnel junctions". In: *Sci. Rep.* 6 (2011), p. 26877. DOI: 10.1038/srep26877.

[11] S. Iwasaki. "Perpendicular magnetic recording –Its development and realization–". In: *Proc. Jap. Ac., Ser. B* 85 (2009), pp. 37–54. DOI: 10.2183/pjab.85.37.

[12] I. Benguettat-El Mokhtari et al. "Perpendicular magnetic anisotropy and interfacial Dzyaloshinskii–Moriya interaction in as grown and annealed X/Co/Y ultrathin systems". In: *J. Phys. Cond. Mat.* 32 (2020), p. 495802. DOI: 10.1088/1361-648x/abb0a8.

[13] B. Tudu and A. Tiwari. "Recent Developments in Perpendicular Magnetic Anisotropy Thin Films for Data Storage Applications". In: *Vacuum* 146 (2017), pp. 329–341. ISSN: 0042-207X. DOI: 10.1016/j.vacuum.2017.01.031.

[14] B. Dieny and M. Chshiev. "Perpendicular magnetic anisotropy at transition metal/oxide interfaces and applications". In: *Rev. Mod. Phys.* 89 (2017), p. 025008. DOI: 10.1103/RevModPhys.89.025008.

[15] H. F. Hamann, Y. C. Martin, and H. K. Wickramasinghe. "Thermally assisted recording beyond traditional limits". In: *Appl. Phys. Lett.* 84 (2004), pp. 810–812. DOI: 10.1063/1.1644924.

[16] T. W. McDaniel. "Ultimate limits to thermally assisted magnetic recording". In: *J. Phys. Cond. Mat.* 17 (2005), R315. DOI: 10.1088/0953-8984/17/7/R01.

[17] B. C. Stipe et al. "Magnetic recording at 1.5 Pb m^{-2} using an integrated plasmonic antenna". In: *Nat. Photonics* 4 (2010), pp. 484–488. DOI: 10.1038/nphoton.2010.90.

[18] P. J. Jensen and K. H. Bennemann. "Magnetic structure of films: Dependence on anisotropy and atomic morphology". In: *Surf. Sci. Rep.* 61 (2006), pp. 129 –199. DOI: 10.1016/j.surfrep.2006.02.001.

[19] D. Wilgocka-Slezak et al. "Thickness-driven polar spin reorientation transition in ultrathin Fe/Au(001) films". In: *Phys. Rev. B* 81 (2010), p. 064421. DOI: 10.1103/PhysRevB.81.064421.

[20] A. Kukunin, J. Prokop, and H. J. Elmers. "Temperature-driven spin reorientation transition in Fe/Mo(110) nanostructures". In: *Phys. Rev. B* 76 (2007), p. 134414. DOI: 10.1103/PhysRevB.76.134414.

[21] M. Farle et al. "Magnetic anisotropy of Co/Cu(111) ultrathin films". In: *Surf. Sci.* 439 (1999), pp. 146 –152. DOI: 10.1016/S0039-6028(99)00762-1.

[22] I. Dzyaloshinsky. "A thermodynamic theory of "weak" ferromagnetism of antiferromagnetics". In: *J. Phys. Chem. Solids* 4 (1958), pp. 241–255. DOI: 10.1016/0022-3697(58)90076-3.

[23] T. Moriya. "New Mechanism of Anisotropic Superexchange Interaction". In: *Phys. Rev. Lett.* 4 (1960), pp. 228–230. DOI: 10.1103/PhysRevLett.4.228.

[24] M. Bode et al. "Chiral magnetic order at surfaces driven by inversion asymmetry". In: *Nature* 447 (2007), pp. 190–193. DOI: 10.1038/nature05802.

[25] K. Ryu et al. "Chiral spin torque at magnetic domain walls". In: *Nat. Nanotechnol.* 8 (2013), pp. 527–533. DOI: 10.1038/nnano.2013.102.

[26] S. Mühlbauer et al. "Skyrmion Lattice in a Chiral Magnet". In: *Science* 323 (2009), pp. 915–919. DOI: 10.1126/science.1166767.

[27] N. Romming et al. "Writing and Deleting Single Magnetic Skyrmions". In: *Science* 341 (2013), pp. 636–639. DOI: 10.1126/science.1240573.

[28] Kh. Zakeri et al. "Asymmetric Spin-Wave Dispersion on Fe(110): Direct Evidence of the Dzyaloshinskii-Moriya Interaction". In: *Phys. Rev. Lett.* 104 (2010), p. 137203. DOI: 10.1103/PhysRevLett.104.137203.

[29] L. Rózsa, U. Atxitia, and U. Nowak. "Temperature scaling of the Dzyaloshinsky-Moriya interaction in the spin wave spectrum". In: *Phys. Rev. B* 96 (2017), p. 094436. DOI: 10.1103/PhysRevB.96.094436.

[30] A. Bogdanov and A. Hubert. "Thermodynamically stable magnetic vortex states in magnetic crystals". In: *J. Magn. Magn. Mater.* 138 (1994), pp. 255–269. DOI: https://doi.org/10.1016/0304-8853(94)90046-9.

[31] S. Heinze et al. "Spontaneous atomic-scale magnetic skyrmion lattice in two dimensions". In: *Nat. Phys.* 7 (2011), 713–718. DOI: https://doi.org/10.1038/nphys2045.

[32] T. Okubo, S. Chung, and H. Kawamura. "Multiple-q States and the Skyrmion Lattice of the Triangular-Lattice Heisenberg Antiferromagnet under Magnetic Fields". In: *Phys. Rev. Lett.* 108 (2012), p. 017206. DOI: 10.1103/PhysRevLett.108.017206.

[33] S. von Malottki et al. "Enhanced skyrmion stability due to exchange frustration". In: *Sci. Rep.* 7 (2017), p. 12299. DOI: 10.1038/s41598-017-12525-x.

[34] Y. Tokura and N. Kanazawa. "Magnetic Skyrmion Materials". In: *Chem. Rev.* 121 (2021), pp. 2857–2897. DOI: 10.1021/acs.chemrev.0c00297.

[35] D. Schick et al. "Skyrmions as quasiparticles: Free energy and entropy". In: *Phys. Rev. B* 103 (2021), p. 214417. DOI: 10.1103/PhysRevB.103.214417.

[36] A. Fert, V. Cros, and J. Sampaio. "Skyrmions on the track". In: *Nat. Nanotechn.* 8 (2013), pp. 152–156. DOI: 10.1038/nnano.2013.29.

[37] J. Iwasaki, M. Mochizuki, and N. Nagaosa. "Current-induced skyrmion dynamics in constricted geometries". In: *Nat. Nanotechn.* 8 (2013), pp. 742–747. DOI: 10.1038/nnano.2013.176.

[38] Y. Zhou and M. Ezawa. "A reversible conversion between a skyrmion and a domain-wall pair in a junction geometry". In: *Nat. Comm.* 5 (2014), p. 4652. DOI: 10.1038/ncomms5652.

[39] C. Psaroudaki and C. Panagopoulos. "Skyrmion Qubits: A New Class of Quantum Logic Elements Based on Nanoscale Magnetization". In: *Phys. Rev. Lett.* 127 (2021), p. 067201. DOI: 10.1103/PhysRevLett.127.067201.

[40] U. Nowak. "Classical Spin Models". In: *Handbook of Magnetism and Advanced Magnetic Materials*. John Wiley & Sons, Ltd, 2007. ISBN: 9780470022184. DOI: 10.1002/9780470022184.hmm205.

[41] A. I. Liechtenstein et al. "Local spin density functional approach to the theory of exchange interactions in ferromagnetic metals and alloys". In: *J. Magn. Magn. Mat.* 67 (1987), pp. 65–74. DOI: 10.1016/0304-8853(87)90721-9.

[42] L. Udvardi et al. "First-principles relativistic study of spin waves in thin magnetic films". In: *Phys. Rev. B* 68 (2003), p. 104436. DOI: 10.1103/PhysRevB.68.104436.

[43] R. Drautz and M. Fähnle. "Spin-cluster expansion: Parametrization of the general adiabatic magnetic energy surface with ab initio accuracy". In: *Phys. Rev. B* 69 (2004), p. 104404. DOI: 10.1103/PhysRevB.69.104404.

[44] L. Szunyogh et al. "Atomistic spin model based on a spin-cluster expansion technique: Application to the $IrMn_3$/Co interface". In: *Phys. Rev. B* 83 (2011), p. 024401. DOI: 10.1103/PhysRevB.83.024401.

[45] A. Deák, L. Szunyogh, and B. Ujfalussy. "Thickness-dependent magnetic structure of ultrathin Fe/Ir(001) films: From spin-spiral states toward ferromagnetic order". In: *Phys. Rev. B* 84 (2011), p. 224413. DOI: 10.1103/PhysRevB.84.224413.

[46] A. Bergman et al. "Magnetic interactions of Mn clusters supported on Cu". In: *Phys. Rev. B* 73 (2006), p. 174434. DOI: 10.1103/PhysRevB.73.174434.

[47] A. Bergman et al. "Non-collinear magnetisation of V clusters supported on a Cu (111) surface: Theory". In: *Surf. Sci.* 600 (2006), pp. 4838–4842. DOI: https://doi.org/10.1016/j.susc.2006.08.004.

[48] A. Bergman et al. "Magnetic structures of small Fe, Mn, and Cr clusters supported on Cu(111): Noncollinear first-principles calculations". In: *Phys. Rev. B* 75 (2007), p. 224425. DOI: 10.1103/PhysRevB.75.224425.

[49] R. Cardias et al. "Magnetic and electronic structure of Mn nanostructures on Ag(111) and Au(111)". In: *Phys. Rev. B* 93 (2016), p. 014438. DOI: 10.1103/PhysRevB.93.014438.

[50] D. C. de Melo Rodrigues et al. "First-principles theory of electronic structure and magnetism of Cr nano-islands on Pd(111)". In: *J. Phys. Cond. Mat.* 29 (2016), p. 025807. DOI: 10.1088/0953-8984/29/2/025807.

[51] G. M. Stocks et al. "Towards a constrained local moment model for first principles spin dynamics". In: *Phil. Mag. B* 78 (1998), pp. 665–673. DOI: 10.1080/13642819808206775.

[52] B. Újfalussy et al. "Constrained density functional theory for first principles spin dynamics". In: *J. Appl. Phys.* 85 (1999), pp. 4824–4826. DOI: 10.1063/1.370494.

[53] B. Újfalussy et al. "Ab initio spin dynamics applied to nanoparticles: Canted magnetism of a finite Co chain along a Pt(111) surface step edge". In: *Phys. Rev. B* 70 (2004), p. 100404. DOI: 10.1103/PhysRevB.70.100404.

[54] P. Gambardella et al. "Ferromagnetism in one-dimensional monatomic metal chains". In: *Nature* 416.6878 (2002), pp. 301–304. DOI: 10.1038/416301a.

[55] L. Balogh et al. "Theoretical study of magnetic domain walls through a cobalt nanocontact". In: *Phys. Rev. B* 86 (2012), p. 024406. DOI: 10.1103/PhysRevB.86.024406.

[56] L. Rózsa, L. Udvardi, and L. Szunyogh. "Langevin spin dynamics based on ab initio calculations: numerical schemes and applications". In: *J. Phys. Cond. Mat.* 26 (2014), p. 216003. DOI: 10.1088/0953-8984/26/21/216003.

[57] J. Korringa. "On the calculation of the energy of a Bloch wave in a metal". In: *Physica* 13 (1947), pp. 392–400. DOI: 10.1016/0031-8914(47)90013-X.

[58] W. Kohn and N. Rostoker. "Solution of the Schrödinger Equation in Periodic Lattices with an Application to Metallic Lithium". In: *Phys. Rev.* 94 (1954), pp. 1111–1120. DOI: 10.1103/PhysRev.94.1111.

[59] L. Szunyogh, B. Újfalussy, and P. Weinberger. "Magnetic anisotropy of iron multilayers on Au(001): First-principles calculations in terms of the fully relativistic spin-polarized screened KKR method". In: *Phys. Rev. B* 51 (1995), pp. 9552–9559. DOI: 10.1103/PhysRevB.51.9552.

[60] A. Laio and M. Parrinello. "Escaping free-energy minima". In: *Proc. Natl. Acad. Sci.* 99 (2002), pp. 12562–12566. DOI: 10.1073/pnas.202427399.

[61] A. Barducci, G. Bussi, and M. Parrinello. "Well-Tempered Metadynamics: A Smoothly Converging and Tunable Free-Energy Method". In: *Phys. Rev. Lett.* 100, 020603 (2008), p. 020603. DOI: 10.1103/PhysRevLett.100.020603.

[62] W. Dürr et al. "Magnetic Phase Transition in Two-Dimensional Ultrathin Fe Films on Au(100)". In: *Phys. Rev. Lett.* 62 (1989), pp. 206–209. DOI: 10.1103/PhysRevLett.62.206.

[63] N. Weber et al. "Nanoscale spatial switching of magnetic anisotropy in pseudomorphic Fe(110) on W(110)". In: *Phys. Rev. B* 55 (1997), pp. 14121–14124. DOI: 10.1103/PhysRevB.55.14121.

[64] T. Slezak et al. "Noncollinear Magnetization Structure at the Thickness-Driven Spin-Reorientation Transition in Epitaxial Fe Films on W(110)". In: *Phys. Rev. Lett.* 105 (2010), p. 027206. DOI: 10.1103/PhysRevLett.105.027206.

[65] P. Hohenberg and W. Kohn. "Inhomogeneous Electron Gas". In: *Phys. Rev.* 136 (1964), B864–B871. DOI: 10.1103/PhysRev.136.B864.

[66] W. Kohn and L. J. Sham. "Self-Consistent Equations Including Exchange and Correlation Effects". In: *Phys. Rev.* 140 (1965), A1133–A1138. DOI: 10.1103/PhysRev.140.A1133.

[67] L. Szunyogh. *Introduction to Multiple Scattering Theory (lecture notes)*. URL: http://newton.phy.bme.hu/~szunyogh/Elszerk/Kkr-slides.pdf.

[68] J. Zabloudil et al. *Electron Scattering in Solid Matter*. Vol. 147. Springer Series in Solid State Sciences. Heidelberg: Springer, 2005. URL: https://link.springer.com/book/10.1007/b138290.

[69] A. Deák. "Finite-temperature magnetism from first principles". PhD thesis. Budapest University of Technology and Economics, 2015. URL: https://repozitorium.omikk.bme.hu/handle/10890/5358.

[70] L. Rózsa. "Finite-temperature magnetism of ultrathin films and nanoclusters". PhD thesis. Budapest University of Technology and Economics, 2016. URL: https://repozitorium.omikk.bme.hu/handle/10890/1552.

[71] L. Balogh. "First principles simulations of magnetic nanostructures". PhD thesis. Budapest University of Technology and Economics, 2017. URL: https://repozitorium.omikk.bme.hu/handle/10890/5392.

[72] J. C. Slater. "Wave Functions in a Periodic Potential". In: *Phys. Rev.* 51 (1937), pp. 846–851. DOI: 10.1103/PhysRev.51.846.

[73] J. S. Faulkner and G. M. Stocks. "Calculating properties with the coherent-potential approximation". In: *Phys. Rev. B* 21 (1980), pp. 3222–3244. DOI: 10.1103/PhysRevB.21.3222.

[74] B. Lazarovits. "Electronic and magnetic properties of nanostructures". PhD thesis. Technischen Universität Wien, 2003. URL: https://repositum.tuwien.at/handle/20.500.12708/8691.

[75] G. Kresse and J. Furthmüller. "Efficient iterative schemes for ab initio total-energy calculations using a plane-wave basis set". In: *Phys. Rev. B* 54 (1996), pp. 11169–11186. DOI: 10.1103/PhysRevB.54.11169.

[76] B. Lazarovits, L. Szunyogh, and P. Weinberger. "Fully relativistic calculation of magnetic properties of Fe, Co, and Ni adclusters on Ag(100)". In: *Phys. Rev. B* 65 (2002), p. 104441. DOI: 10.1103/PhysRevB.65.104441.

[77] A. Lászlóffy et al. "Magnetic structure of monatomic Fe chains on Re(0001): Emergence of chiral multispin interactions". In: *Phys. Rev. B* 99 (2019), p. 184430. DOI: 10.1103/PhysRevB.99.184430.

[78] H. J. F. Jansen. "Magnetic anisotropy in density-functional theory". In: *Phys. Rev. B* 59 (1999), pp. 4699–4707. DOI: 10.1103/PhysRevB.59.4699.

[79] P. Lloyd. "Wave propagation through an assembly of spheres: II. The density of single-particle eigenstates". In: *Proc. Phys. Soc.* 90 (1967), pp. 207–216. DOI: 10.1088/0370-1328/90/1/323.

[80] N. Metropolis et al. "Equation of State Calculations by Fast Computing Machines". In: *J. Chem. Phys.* 21 (1953), pp. 1087–1092. DOI: 10.1063/1.1699114.

[81] F. Wang and D. P. Landau. "Efficient, Multiple-Range Random Walk Algorithm to Calculate the Density of States". In: *Phys. Rev. Lett.* 86 (2001), pp. 2050–2053. DOI: 10.1103/PhysRevLett.86.2050.

[82] S. Marsili et al. "Self-healing Umbrella Sampling: A Non-equilibrium Approach for Quantitative Free Energy Calculations". In: *J. Phys. Chem. B* 110 (2006), pp. 14011–14013. DOI: 10.1021/jp062755j.

[83] J. F. Dama, M. Parrinello, and G. A. Voth. "Well-Tempered Metadynamics Converges Asymptotically". In: *Phys. Rev. Lett.* 112 (2014), p. 240602. DOI: 10.1103/PhysRevLett.112.240602.

[84] F. Marini et al. "Metadynamic sampling of the free-energy landscapes of proteins coupled with a Monte Carlo algorithm". In: *Gene* 422.1-2 (2008), pp. 37 –40. DOI: http://dx.doi.org/10.1016/j.gene.2008.06.003.

[85] Y. Crespo et al. "Metadynamics convergence law in a multidimensional system". In: *Phys. Rev. E* 81 (2010), 055701(R). DOI: 10.1103/PhysRevE.81.055701.

[86] J. Tóbik, R. Martonák, and V. Cambel. "Free-energy landscapes in magnetic systems from metadynamics". In: *Phys. Rev. B* 96 (2017), 140413(R). DOI: 10.1103/PhysRevB.96.140413.

[87] I. Charalampidis and J. Barker. *Metadynamics calculations of the effect of thermal spin fluctuations on skyrmion stability*. 2023. DOI: 10.48550/arXiv.2310.03169. arXiv: 2310.03169 [cond-mat.mtrl-sci].

[88] A. Honkela et al. "Natural Conjugate Gradient in Variational Inference". In: *Neural Information Processing*. Ed. by M. Ishikawa et al. Berlin, Heidelberg: Springer Berlin Heidelberg, 2008, pp. 305–314. ISBN: 978-3-540-69162-4. DOI: 10.1007/978-3-540-69162-4_32.

[89] S. T. Smith. *Geometric Optimization Methods for Adaptive Filtering*. 2013. DOI: 10.48550/arXiv.1305.1886. arXiv: 1305.1886 [math.OC].

[90] A. Edelman, T. Arias, and S. Smith. "The Geometry of Algorithms with Orthogonality Constraints". In: *SIAM J. Matrix Anal. Appl.* 20 (1998). DOI: 10.1137/S0895479895290954.

[91] E. Polak and G. Ribière. "Note sur la convergence de méthodes de directions conjuguées". fre. In: *Math. Mod. Num. Anal.* 3.R1 (1969), pp. 35–43. DOI: 10.1051/m2an/196903R100351.

[92] B. Nagyfalusi, L. Udvardi, and L. Szunyogh. "Metadynamics study of the temperature dependence of magnetic anisotropy and spin-reorientation transitions in ultrathin films". In: *Phys. Rev. B* 100 (2019), p. 174429. DOI: 10.1103/PhysRevB.100.174429.

[93] B. Nagyfalusi, L. Udvardi, and L. Szunyogh. "First principles and metadynamics study of the spin-reorientation transition in Fe/Au(001) films". In: *J. Phys. Conf. Ser.* 903.1 (2017), p. 012016. DOI: 10.1088/1742-6596/903/1/012016.

[94] B. Nagyfalusi et al. "Spin reorientation transition in an ultrathin Fe film on W(110) induced by Dzyaloshinsky-Moriya interactions". In: *Phys. Rev. B* 102 (2020), p. 134413. DOI: 10.1103/PhysRevB.102.134413.

[95] P. Ravindran et al. "Large magnetocrystalline anisotropy in bilayer transition metal phases from first-principles full-potential calculations". In: *Phys. Rev. B* 63 (2001), p. 144409. DOI: 10.1103/PhysRevB.63.144409.

[96] J. P. Liu et al. "Magnetic hardening in FePt nanostructured films". In: *J. Appl. Phys* 81.8 (1997), pp. 5644–5646. DOI: 10.1063/1.364681.

[97] M. Farle. "Ferromagnetic resonance of ultrathin metallic layers". In: *Rep. Prog. Phys.* 61 (1998), pp. 755–826. DOI: 10.1088/0034-4885/61/7/001.

[98] Cochran J. F. "Light Scattering from Ultrathin Magnetic Layers and Bilayers". In: *Ultrathin Magnetic Structures II*. Berlin: Springer, 1994. Chap. 3.2, 222–. DOI: 10.1007/b138706.

[99] Ulrich Gradmann. "Chapter 1 Magnetism in ultrathin transition metal films". In: vol. 7. Handbook of Magnetic Materials. Elsevier, 1993, pp. 1–96. DOI: https://doi.org/10.1016/S1567-2719(05)80042-3.

[100] Bader S. D. and Erskine J. L. "Magneto-Optical Effects in Ultrathin Films". In: *Ultrathin Magnetic Structures II*. Berlin: Springer, 1994. Chap. 4, 297–325. DOI: 10.1007/b138706.

[101] A. Berger and H. Hopster. "Nonequilibrium Magnetization near the Reorientation Phase Transition of Fe/Ag(100) Films". In: *Phys. Rev. Lett.* 76 (1996), pp. 519–522. DOI: 10.1103/PhysRevLett.76.519.

[102] R Sellmann et al. "Thickness- and temperature-driven spin-reorientation-transition in ultrathin epitaxial Co-films". In: *Physica B: Condens. Matter* 276-278 (2000), pp. 578 –579. DOI: 10.1016/S0921-4526(99)01811-6.

[103] M. B. Stearns. "1.1.2.5 Magnetocrystalline anisotropy constants". In: ed. by H.P.J. Wijn. Springer-Verlag Berlin Heidelberg, 1986. DOI: 10.1007/10311893_8.

[104] J. B. Staunton et al. "Spin fluctuations in nearly magnetic metals from ab initio dynamical spin susceptibility calculations: Application to Pd and $Cr_{95}V_5$". In: *Phys. Rev. B* 62 (2000), pp. 1075–1082. DOI: 10.1103/PhysRevB.62.1075.

[105] L. Szunyogh et al. "Magnetic anisotropy of ordered and disordered FePd thin films". In: *Phys. Rev. B* 63 (2001), p. 184408. DOI: 10.1103/PhysRevB.63.184408.

[106] N. Akulov. "Zur Quantentheorie der Temperaturabhängigkeit der Magnetisierungskurve". In: *Z. Phys.* 197 (1936). DOI: 10.1007/BF01418601.

[107] C. Zener. "Classical Theory of the Temperature Dependence of Magnetic Anisotropy Energy". In: *Phys. Rev.* 96 (1954), pp. 1335–1337. DOI: 10.1103/PhysRev.96.1335.

[108] H. B. Callen and E. Callen. "The present status of the temperature dependence of magnetocrystalline anisotropy, and the l(l+1)2 power law". In: *J. Phys. Chem. Solids* 27 (1966), pp. 1271 –1285. DOI: 10.1016/0022-3697(66)90012-6.

[109] J. B. Staunton et al. "Temperature Dependent Magnetic Anisotropy in Metallic Magnets from an Ab Initio Electronic Structure Theory: $L1_0$-Ordered FePt". In: *Phys. Rev. Lett.* 93 (2004), p. 257204. DOI: 10.1103/PhysRevLett.93.257204.

[110] O. N. Mryasov et al. "Temperature-dependent magnetic properties of FePt: Effective spin Hamiltonian model". In: *EPL* 69 (2005), p. 805. DOI: 10.1209/epl/i2004-10404-2.

[111] P. Weinberger and L. Szunyogh. "Perpendicular magnetism in magnetic multilayer systems". In: *Comput. Mater. Sci.* 17 (2000), pp. 414–437. DOI: 10.1016/S0927-0256(00)00063-X.

[112] A. Fert and Peter M. Levy. "Role of Anisotropic Exchange Interactions in Determining the Properties of Spin-Glasses". In: *Phys. Rev. Lett.* 44 (1980), pp. 1538–1541. DOI: 10.1103/PhysRevLett.44.1538.

[113] Peter M. Levy and A. Fert. "Anisotropy induced by nonmagnetic impurities in Cu Mn spin-glass alloys". In: *Phys. Rev. B* 23 (1981), pp. 4667–4690. DOI: 10.1103/PhysRevB.23.4667.

[114] M. Cubukcu et al. "Dzyaloshinskii-Moriya anisotropy in nanomagnets with in-plane magnetization". In: *Phys. Rev. B* 93 (2016), p. 020401. DOI: 10.1103/PhysRevB.93.020401.

[115] C. Liu, E. R. Moog, and S. D. Bader. "Polar Kerr-Effect Observation of Perpendicular Surface Anisotropy for Ultrathin fcc Fe Grown on Cu(100)". In: *Phys. Rev. Lett.* 60 (1988), pp. 2422–2425. DOI: 10.1103/PhysRevLett.60.2422.

[116] S. S. Kang, W. Kuch, and J. Kirschner. "Structural and magnetic properties of Fe thin films on $Cu_{90}Au_{10}$(001)". In: *Phys. Rev. B* 63 (2000), p. 024401. DOI: 10.1103/PhysRevB.63.024401.

[117] D. Peterka et al. "Adsorbate and thermally induced spin reorientation transition in low-temperature-grown Fe/Cu(001)". In: *Phys. Rev. B* 66 (2002), p. 104411. DOI: 10.1103/PhysRevB.66.104411.

[118] N. C. Koon et al. "Direct Evidence for Perpendicular Spin Orientations and Enhanced Hyperfine Fields in Ultrathin Fe(100) Films on Ag(100)". In: *Phys. Rev. Lett.* 59 (1987), pp. 2463–2466. DOI: 10.1103/PhysRevLett.59.2463.

[119] R. Allenspach, M. Stampanoni, and A. Bischof. "Magnetic domains in thin epitaxial Co/Au(111) films". In: *Phys. Rev. Lett.* 65 (1990), pp. 3344–3347. DOI: 10.1103/PhysRevLett.65.3344.

[120] L. Udvardi et al. "On tilted magnetization in thin films". In: *J. Magn. Magn. Mater.* 183.3 (1998), pp. 283–291. DOI: https://doi.org/10.1016/S0304-8853(97)01084-6.

[121] M. Kisielewski et al. "New Possibilities for Tuning Ultrathin Cobalt Film Magnetic Properties by a Noble Metal Overlayer". In: *Phys. Rev. Lett.* 89 (2002), p. 087203. DOI: 10.1103/PhysRevLett.89.087203.

[122] I.-G. Baek et al. "Spin reorientation transition in Fe(110) thin films: The role of surface anisotropy". In: *Phys. Rev. B* 67 (2003), p. 075401. DOI: 10.1103/PhysRevB.67.075401.

[123] D. P. Pappas, K.-P. Kämper, and H. Hopster. "Reversible transition between perpendicular and in-plane magnetization in ultrathin films". In: *Phys. Rev. Lett.* 64 (1990), pp. 3179–3182. DOI: 10.1103/PhysRevLett.64.3179.

[124] L. Udvardi et al. "Reorientation phase transitions in thin magnetic films: a review of the classical vector spin model within the mean-field approach". In: *Phil. Mag. B* 81 (2001), pp. 613–628. DOI: 10.1080/13642810108225455.

[125] A. Laio and F. L. Gervasio. "Metadynamics: a method to simulate rare events and reconstruct the free energy in biophysics, chemistry and material science". In: *Rep. Prog. Phys.* 71 (2008), p. 126601. DOI: 10.1088/0034-4885/71/12/126601.

[126] P. Raiteri et al. "Efficient Reconstruction of Complex Free Energy Landscapes by Multiple Walkers Metadynamics". In: *J. Phys. Chem. B* 110 (2006), pp. 3533–3539. DOI: 10.1021/jp054359r.

[127] P. Asselin et al. "Constrained Monte Carlo method and calculation of the temperature dependence of magnetic anisotropy". In: *Phys. Rev. B* 82 (2010), p. 054415. DOI: 10.1103/PhysRevB.82.054415.

[128] S. Okamoto et al. "Chemical-order-dependent magnetic anisotropy and exchange stiffness constant of FePt (001) epitaxial films". In: *Phys. Rev. B* 66 (2002), p. 024413. DOI: 10.1103/PhysRevB.66.024413.

[129] A. Deák et al. "Metallic magnetism at finite temperatures studied by relativistic disordered moment description: Theory and applications". In: *Phys. Rev. B* 89 (2014), p. 224401. DOI: 10.1103/PhysRevB.89.224401.

[130] N. D. Mermin and H. Wagner. "Absence of Ferromagnetism or Antiferromagnetism in One- or Two-Dimensional Isotropic Heisenberg Models". In: *Phys. Rev. Lett.* 17 (1966), pp. 1133–1136. DOI: 10.1103/PhysRevLett.17.1133.

[131] A. Moschel and K. D. Usadel. "Reorientation transitions of first and second order in thin ferromagnetic films". In: *Phys. Rev. B* 51 (1995), pp. 16111–16114. DOI: 10.1103/PhysRevB.51.16111.

[132] Yu. A. Fridman, D. V. Spirin, and Ph. N. Klevets. "Reorientation of magnetization with temperature in 2D ferromagnets". In: *J. Magn. Magn. Mater.* 253 (2002), pp. 105–110. DOI: 10.1016/S0304-8853(02)00159-2.

[133] D. Sander. "The correlation between mechanical stress and magnetic anisotropy in ultrathin films". In: *Rep. Prog. Phys.* 62 (1999), p. 809. DOI: 10.1088/0034-4885/62/5/204.

[134] H. L. Meyerheim et al. "Surface structure and stress in Fe monolayers on W(110)". In: *Phys. Rev. B* 64 (2001), p. 045414. DOI: 10.1103/PhysRevB.64.045414.

[135] J. Hauschild, U. Gradmann, and H. J. Elmers. "Perpendicular magnetization and dipolar antiferromagnetism in double layer nanostripe arrays of Fe(110) on W(110)". In: *Appl. Phys. Lett.* 72 (1998), pp. 3211–3213. DOI: 10.1063/1.121552.

[136] M. Heide, G. Bihlmayer, and S. Blügel. "Dzyaloshinskii-Moriya interaction accounting for the orientation of magnetic domains in ultrathin films: Fe/W(110)". In: *Phys. Rev. B* 78 (2008), 140403(R). DOI: 10.1103/PhysRevB.78.140403.

[137] K. von Bergmann, M. Bode, and R. Wiesendanger. "Coverage-dependent spin reorientation transition temperature of the Fe double-layer on W(110) observed by scanning tunneling microscopy". In: *J. Magn. Magn. Mater.* 305 (2006), pp. 279 –283. DOI: 10.1016/j.jmmm.2005.12.015.

[138] H. J. Elmers, J. Hauschild, and U. Gradmann. "Onset of perpendicular magnetization in nanostripe arrays of Fe on stepped W(110) surfaces". In: *Phys. Rev. B* 59 (1999), pp. 3688–3695. DOI: 10.1103/PhysRevB.59.3688.

[139] M. J. Dunlavy and D. Venus. "Critical susceptibility exponent measured from Fe/W(110) bilayers". In: *Phys. Rev. B* 69 (2004), p. 094411. DOI: 10.1103/PhysRevB.69.094411.

[140] M. Albrecht et al. "Scattering phases in low energy electron diffraction from spot profile analysis and from multiple scattering theory". In: *Solid State Commun.* 78 (1991), pp. 671 –675. DOI: 10.1016/0038-1098(91)90399-G.

[141] E. D. Tober et al. "Interface Structures of Ordered Fe and Gd Overlayers on W(110) from Photoelectron Diffraction". In: *Phys. Rev. Lett.* 79 (1997), pp. 2085–2088. DOI: 10.1103/PhysRevLett.79.2085.

[142] X. Qian and W. Hübner. "First-principles calculation of structural and magnetic properties for Fe monolayers and bilayers on W(110)". In: *Phys. Rev. B* 60 (1999), pp. 16192–16197. DOI: 10.1103/PhysRevB.60.16192.

[143] B. Santos et al. "Structure and stability of ultrathin Fe films on W(110)". In: *Phys. Rev. B* 93 (2016), p. 195423. DOI: 10.1103/PhysRevB.93.195423.

[144] M. Heide. "Magnetic domain walls in ultrathin films: Contribution of the Dzyaloshinsky-Moriya interaction". PhD thesis. Rheinisch-Westfälische Technische Hochschule Aachen, 2006. URL: http://publications.rwth-aachen.de/record/52536/files/Heide_Marcus.pdf.

[145] M. Slezak et al. "Perpendicular magnetic anisotropy and noncollinear magnetic structure in ultrathin Fe films on W(110)". In: *Phys. Rev. B* 87 (2013), p. 134411. DOI: 10.1103/PhysRevB.87.134411.

[146] S. Meckler et al. "Real-Space Observation of a Right-Rotating Inhomogeneous Cycloidal Spin Spiral by Spin-Polarized Scanning Tunneling Microscopy in a Triple Axes Vector Magnet". In: *Phys. Rev. Lett.* 103 (2009), p. 157201. DOI: 10.1103/PhysRevLett.103.157201.

[147] R. F. L. Evans et al. "Temperature scaling of two-ion anisotropy in pure and mixed anisotropy systems". In: *Phys. Rev. B* 102 (2020), p. 020412. DOI: 10.1103/PhysRevB.102.020412.

[148] A. Neubauer et al. "Topological Hall Effect in the *A* Phase of MnSi". In: *Phys. Rev. Lett.* 102 (2009), p. 186602. DOI: 10.1103/PhysRevLett.102.186602.

[149] C. Pappas et al. "Chiral Paramagnetic Skyrmion-like Phase in MnSi". In: *Phys. Rev. Lett.* 102 (2009), p. 197202. DOI: 10.1103/PhysRevLett.102.197202.

[150] X. Z. Yu et al. "Real-space observation of a two-dimensional skyrmion crystal". In: *Nature* 465 (2010), pp. 901–904. DOI: 10.1038/nature09124.

[151] S. Meyer et al. "Isolated zero field sub-10 nm skyrmions in ultrathin Co films". In: *Nat. Commun.* 10 (2019), p. 3823. DOI: 10.1038/s41467-019-11831-4.

[152] A. M. Polyakov and A. A. Belavin. "Metastable States of Two-Dimensional Isotropic Ferromagnets". In: *JETP Lett.* 22 (1975), pp. 245–248.

[153] B. Berg and M. Lüscher. "Definition and statistical distributions of a topological number in the lattice O(3) σ-model". In: *Nucl. Phys. B* 190 (1981), pp. 412–424. DOI: 10.1016/0550-3213(81)90568-x.

[154] A. O. Leonov et al. "The properties of isolated chiral skyrmions in thin magnetic films". In: *New J. Phys.* 18 (2016), p. 065003. DOI: 10.1088/1367-2630/18/6/065003.

[155] L. Rózsa et al. "Formation and stability of metastable skyrmionic spin structures with various topologies in an ultrathin film". In: *Phys. Rev. B* 95 (2017), p. 094423. DOI: 10.1103/PhysRevB.95.094423.

[156] A. O. Leonov and M. Mostovoy. "Multiply periodic states and isolated skyrmions in an anisotropic frustrated magnet". In: *Nat. Commun.* 6 (2015), p. 8275. DOI: 10.1038/ncomms9275.

[157] P. F. Bessarab, V. M. Uzdin, and H. Jónsson. "Method for finding mechanism and activation energy of magnetic transitions, applied to skyrmion and antivortex annihilation". In: *Comput. Phys. Commun.* 196 (2015), pp. 335–347. DOI: 10.1016/j.cpc.2015.07.001.

[158] D. Cortés-Ortuño et al. "Thermal stability and topological protection of skyrmions in nanotracks". In: *Sci. Rep.* 7 (2017), p. 4060. DOI: 10.1038/s41598-017-03391-8.

[159] L. Desplat et al. "Thermal stability of metastable magnetic skyrmions: Entropic narrowing and significance of internal eigenmodes". In: *Phys. Rev. B* 98 (2018), p. 134407. DOI: 10.1103/PhysRevB.98.134407.

[160] S. von Malottki et al. "Skyrmion lifetime in ultrathin films". In: *Phys. Rev. B* 99 (2019), p. 060409. DOI: 10.1103/PhysRevB.99.060409.

[161] F. Muckel et al. "Experimental identification of two distinct skyrmion collapse mechanisms". In: *Nat. Phys.* 17 (2021), pp. 395–402. DOI: 10.1038/s41567-020-01101-2.

[162] J. Hagemeister et al. "Stability of single skyrmionic bits". In: *Nat. Commun.* 6 (2015), p. 8455. DOI: 10.1038/ncomms9455.

[163] L. Desplat et al. "Path sampling for lifetimes of metastable magnetic skyrmions and direct comparison with Kramers' method". In: *Phys. Rev. B* 101 (2020), p. 060403. DOI: 10.1103/PhysRevB.101.060403.

[164] P. Lindner et al. "Temperature and magnetic field dependent behavior of atomic-scale skyrmions in Pd/Fe/Ir(111) nanoislands". In: *Phys. Rev. B* 101 (2020), p. 214445. DOI: 10.1103/PhysRevB.101.214445.

[165] A. F. Schäffer et al. "Stochastic dynamics and pattern formation of geometrically confined skyrmions". In: *Commun. Phys.* 2 (2019), p. 72. DOI: 10.1038/s42005-019-0176-y.

[166] C. Song et al. "Commensurability between Element Symmetry and the Number of Skyrmions Governing Skyrmion Diffusion in Confined Geometries". In: *Adv. Funct. Mater.* 31 (2021), p. 2010739. DOI: https://doi.org/10.1002/adfm.202010739.

[167] Y. Ge et al. "Constructing coarse-grained skyrmion potentials from experimental data with Iterative Boltzmann Inversion". In: *Commun. Phys.* 6 (2023), p. 30. DOI: 10.1038/s42005-023-01145-9.

[168] S. Sugimoto et al. "Nonlocal accumulation, chemical potential, and Hall effect of skyrmions in Pt/Co/Ir heterostructure". In: *Sci. Rep.* 10 (2020), p. 1009. DOI: 10.1038/s41598-020-57818-w.

[169] L. Rózsa et al. "Skyrmions with Attractive Interactions in an Ultrathin Magnetic Film". In: *Phys. Rev. Lett.* 117 (2016), p. 157205. DOI: 10.1103/PhysRevLett.117.157205.

[170] L. Rózsa, M. Weißenhofer, and U. Nowak. "Spin waves in skyrmionic structures with various topological charges". In: *J. Phys. Cond. Mat.* 33 (2020), p. 054001. DOI: 10.1088/1361-648x/abc404.

[171] N. Romming et al. "Field-Dependent Size and Shape of Single Magnetic Skyrmions". In: *Phys. Rev. Lett.* 114 (2015), p. 177203. DOI: 10.1103/PhysRevLett.114.177203.

[172] M. Böttcher et al. "$B - T$ phase diagram of Pd/Fe/Ir(111) computed with parallel tempering Monte Carlo". In: *New J. Phys.* 20 (2018), p. 103014. DOI: 10.1088/1367-2630/aae282.

[173] I. P. Miranda et al. "Band filling effects on the emergence of magnetic skyrmions: Pd/Fe and Pd/Co bilayers on Ir(111)". In: *Phys. Rev. B* 105 (2022), p. 224413. DOI: 10.1103/PhysRevB.105.224413.

[174] E. Simon et al. "Formation of magnetic skyrmions with tunable properties in PdFe bilayer deposited on Ir(111)". In: *Phys. Rev. B* 90 (2014), p. 094410. DOI: 10.1103/PhysRevB.90.094410.

[175] U. A. A. Rodríguez et al. *Magnetic exchange interactions at the proximity of a superconductor*. 2023. arXiv: 2306.02906 [cond-mat.supr-con].

[176] A. Lehnert et al. "Magnetic anisotropy of Fe and Co ultrathin films deposited on Rh(111) and Pt(111) substrates: An experimental and first-principles investigation". In: *Phys. Rev. B* 82 (2010), p. 094409. DOI: 10.1103/PhysRevB.82.094409.

[177] P. Błonski et al. "Magnetocrystalline anisotropy energy of Co and Fe adatoms on the (111) surfaces of Pd and Rh". In: *Phys. Rev. B* 81 (2010), p. 104426. DOI: 10.1103/PhysRevB.81.104426.

[178] B. Hardrat et al. "Complex magnetism of iron monolayers on hexagonal transition metal surfaces from first principles". In: *Phys. Rev. B* 79 (2009), p. 094411. DOI: 10.1103/PhysRevB.79.094411.

[179] A. Krönlein et al. "Magnetic Ground State Stabilized by Three-Site Interactions: Fe/Rh(111)". In: *Phys. Review Lett.* 120.20 (2018). DOI: 10.1103/physrevlett.120.207202.

[180] A. Lászlóffy et al. "Electronic and Magnetic Properties of Building Blocks of Mn and Fe Atomic Chains on Nb(110)". In: *Nanomaterials* 11 (2021), p. 1933. DOI: 10.3390/nano11081933.

[181] S. Brinker, M. dos Santos Dias, and S. Lounis. "The chiral biquadratic pair interaction". In: *New J. Phys.* 21 (2019), p. 083015. DOI: 10.1088/1367-2630/ab35c9.